CHARACTERIZATION OF FADING AND POLARIZATION STATE DISPERSION ON FIXED WIRELESS LINKS IN SUBURBAN MACROCELL ENVIRONMENTS

by

Anthony En-Lee Liou

B.A.Sc., University of British Columbia, 2006

A THESIS SUBMITTED IN PARTIAL FULFILLMENT OF
THE REQUIREMENTS FOR THE DEGREE OF

MASTER OF APPLIED SCIENCE

in

The Faculty of Graduate Studies

(Electrical and Computer Engineering)

THE UNIVERSITY OF BRITISH COLUMBIA

(Vancouver)

March 2009

ABSTRACT

Growing use of point-to-multipoint fixed wireless networks to support network access and system automation in suburban macrocell environments has prompted regulators to re-allocate various bands between 200 MHz and 2 GHz to such applications. Links in such networks are usually obstructed by buildings and foliage and are classified as non-line-of-sight. Although it is well-known that such links are susceptible to fading caused by windblown trees and foliage, most past efforts to characterize fading on such links have focused on frequency bands at 1.9 GHz and above. Here, we study how the depth and rate of fading in the 220, 850 and 1900 MHz bands vary with distance and time-averaged wind speed in a representative macrocell environment. We observed that while the signal fading is relatively severe at 1.9GHz, the depth of fading drops rapidly as the carrier frequency decreases. However, the rate of fading is effectively independent of either the average wind speed or the carrier frequency. Further, polarization diversity on narrowband wireless links has traditionally been characterized in terms of the fading statistics and the cross-correlation between the fading signals on each branch. A complementary approach, which is independent of the polarization states of the diversity receiving antennas, is to characterize the manner in which the polarization states observed at the receiver disperse across the Poincaré sphere. First, by simulation, we show that when the fading signals observed on orthogonal diversity branches follow ideal Ricean statistics, the distribution of polarization states on the Poincaré sphere is well-approximated by a Fisher distribution whose concentration parameter is: (1) determined by the corresponding Ricean K-factors and the cross-correlation coefficient between the diversity branches, and (2) a good indicator of the level of cross-polar discrimination (XPD). Finally, from measurements collected in a typical suburban macrocell environment at 1.9GHz, we show that: (1) the means of the polarization state distributions also tends to follow a Fisher distribution and (2) the Fisher concentration parameter is negatively correlated with the average wind speed. Development of a model applicable to a broad range of environments will require additional data from other sites and measurement configurations.

TABLE OF CONTENTS

LIST OF TABLES

LIST OF FIGURES

ACKNOWLEDGEMENTS

I offer my enduring gratitude to the faculty, staff and my fellow students at the UBC, who have inspired me to continue my work in this field.

I thank Dr. Michelson for supervising my work and providing critical guidance, suggestions and considerations.

I also thank my colleague Kyle Sivertsen for his considerable assistance through the whole work, and every student in Radio Science Lab who offered their help generously to assist this study during data collection phase.

Special thanks are owed to my parents and my sister, whose have supported me throughout my years of education.

CO-AUTHORSHIP STATEMENT

A version of Chapters 2,3,4,5,and 6 in this thesis has either been accepted by or has been submitted to an IEEE journal for publication:

Each of the above projects was initiated and identified by Prof. D.G. Michelson. Prof. Michelson contributed greatly to the (1) design of the project, (2) research details, including some research methods, math derivations, and results explanation, (3) editing/organizing manuscripts.

In [1], Mr. Sivertsen helped with database maintenance and proof read the manuscript. Both Mr. Arjmandi and Viswanathan assisted to configure the measurement test bed and contributed to data collection. Both Mr. Diallo and Mr. Lancashire provided access and space for base station set up in BC Hydro building at Edmonds.

In [2], Mr. Sivertsen helped with data collection and implemented the equivalent Doppler frequency estimation function in Matlab.

In [3], Mr. Sivertsen supplied the equivalent Doppler frequency estimation function.

In [4], Mr. Sivertsen developed the simulation program, analyzed the simulated results and finalized the trends and findings.

In [5], Mr. Sivertsen helped with data collection and implemented the polarization state estimation function in Matlab.

My major contributions are: For projects [1], [2], [3], and [5], I (1) conducted the research including literature survey, algorithm verification and implementation; (2) determined the project details concerning the procedures of measurement conduction, system configuration, calibration and verification, data collection, and data reduction; (3) configured and calibrated measurement system; (4)conducted field measurement, including both development and production rounds; (5) analyzed the data including data reduction, comparison and organizing; (6) organized and explained the results; (7) prepared the manuscripts including drafting/editing the papers and providing the results. For project [4], I implemented the cross-correlated Ricean sequence simulator in Matlab and participated in preparation of the manuscript.

1 Introduction

1.1 Introduction to Fixed Wireless Communication System in Suburban Macrocell Environment

Fixed wireless technology has attracted considerable interest in recent years as: (1) common carriers seek methods for providing either fixed or nomadic network access services to residential households without the expense of deploying wireline connectivity over the last mile [1], [2] and (2) as public utilities seek methods that will allow them to: (a) detect and report outages, (b) monitor usage, and (c) implement strategies that encourage customers to limit consumption and adopt sustainable practices [3]-[5].

Fixed wireless multipoint communication systems are often deployed in suburban macrocell environments where the base station antenna is mounted well above the local rooftop or treetop level and the remote station antenna is mounted well below the local rooftop or treetop level. In such environments, signal fading over the wireless link is usually as a result of scattering and diffraction by intervening obstacles, when the signal travels along the path from base station to remote terminal. Because both the transmitting and receiving antennas are fixed, signal fading is caused by not only the alignment of the obstacles, i.e., houses and buildings, but also the motion of objects in the environment that scatter and diffract the signal, such as wind-blown foliage and trees, moving vehicles and pedestrians.

Research groups across the world have been devoted in studying and developing wireless channel models in various types environments and system configurations. Especially in narrowband fixed wireless communication area, researchers in Canada, the United States, the United Kingdom, Chile, Australia and elsewhere have conducted measurement campaigns aimed at characterizing the manner in which signal fading occurs on non-line-of-sight (NLOS) paths in macrocell environments, *e.g.*, [6]-[13]. Such studies have variously sought to characterize: (1) the first-order statistics of the fading signal envelope over time and location, (2) the rate at which the signal fades, either through direct estimation of the Doppler spectrum or through estimation of the average fade duration and level crossing rate, (3) the effect of the height and beamwidth of the receiving antenna, local density of vegetation and the wind speed in the vicinity, and (4) the performance of space and polarization diversity at either the base station or the remote terminal.

The vast majority of previous studies of fixed wireless channels in suburban macrocell environments focused on individual frequency bands at 1.9 GHz and above, including the PCS band at 1.9 GHz, the ISM band at 2.45 GHz, the Fixed Wireless Access (FWA) band at 3.5 GHz and the U-NII and ISM bands at 5.2 and 5.8 GHz. Spectrum regulators have recently begun to reallocate frequency bands below 2 GHz in order to help meet the requirements for broadband wireless access for urban and rural areas and/or narrowband telemetry for public utilities. In Canada, spectrum in frequency bands near 700 MHz has been proposed for fixed wireless broadband use in rural areas [14] and may find application in distribution automation by the electrical power industry. Frequency bands such as 220–222 MHz and 1429.5–1432 MHz have recently been designated for utility telemetry and distribution automation [15]. Therefore, we choose 1.9 GHz and 200 MHz to 2GHz as our main frequency bands of interests.

In this work, one of the main goals is to study the effect of wind blowing through vegetation on channel impairments. Therefore, the measurements were collected in a condition in which most of the motion in the environment arose from wind-blowing trees; few cars, people or other moving scatterers were in the vicinity. Moreover, the results presented in this work are specific to geographical conditions of the specific sites, distance, density of vegetation, relative transmitting and receiving antenna heights, and meteorological statistics experienced during the measurement period, i.e., averaged wind speed.

1.2 Fading on Fixed Wireless Channels between 200 MHz and 2 GHz

The vast majority of previous studies of fixed wireless channels in suburban macrocell environments focused on individual frequency bands at 1.9 GHz and above. The manner in which path loss, or its reciprocal, path gain, is affected by the carrier frequency, the heights of and separation between the base station and mobile terminal in suburban macrocell environments over the range from 200 MHz to 2 GHz has been well-studied over the years and has been captured by several standard models [16]-[18]. However, existing channel models do not provide a description of the depth of signal fading that fixed wireless channels will experience over this frequency range in suburban macrocell environments. (Ref. [19] describes fading on UHF links between fixed nodes within a tropical rain forest but the link configuration (both nodes were located below the forest canopy) was quite different from that encountered in suburban macrocells.) This lack of information places those charged with planning, simulating or deploying fixed wireless systems in suburban macrocell environments at a severe disadvantage when asked to predict system coverage and outage probabilities.

Here, we take the first steps to develop measurement-based fading channel models suitable for use across the frequency range from 200 MHz to 2 GHz. Based on the time-series data collected in the 220, 850 and 1900 MHz bands at fixed locations at ranges between 1 and 4 km, we reduced the data in order to determine the manner in which path gain and signal fading vary with distance, time-averaged wind speed and carrier frequency in a typical suburban macrocell environment. The resulting measurement-based model allows the coverage and outage probability in a typical macrocell environment to be compared.

1.3 Rate of Fading on Fixed Wireless Channels between 200 MHz and 2 GHz

The rate at which signal fading occurs may be characterized either by the Level Crossing Rate (LCR) and Average Fade Duration (AFD) at selected thresholds above and below the mean signal strength [20] (which depend on both the first- and second-order statistics of the fading signal) or by a Doppler power spectrum [21],[22] (which depends only upon the second-order statistics). Although the latter representation is particularly useful because it is a key input for algorithms used to simulate (or emulate) fading channels, *e.g.*, [23],[24] , estimation of the Doppler power spectrum from measured data generally requires coherent time series data (amplitude and phase). Fading on fixed wireless links occurs so slowly, however, that lack of phase coherence between the local oscillators in the widely separated transmitter and receiver can severely distort the result. Although a method for estimating the Doppler spectrum from amplitude-only measurement data was proposed in [22], it is intended mainly for use on short-range line-of-sight paths where the Ricean K-factor is high, *e.g.*, $K > 10$, and is much less effective in suburban macrocell environments where K is often < 10.

In certain cases, it has been found that one can fit the measured level crossing rate (LCR) and/or average fade duration (AFD) distributions seen on fixed wireless links to expressions that are normally justified only for mobile wireless links [20]. This allows one to express the time variation on the link in terms of just three parameters: the mean signal strength, the Ricean K-factor, and an equivalent Doppler frequency which is referred to as $f_{d,FW}$ in [20] and which we will simply refer to as f_d. Here, based upon short-term measurements collected at 107 different locations in a suburban macrocell environment characterized by flat terrain and heavy foliage, we present what we believe is the first effort to describe the manner in which both K and f_d on 1.9 GHz and 200 MHz to 2GHz fixed wireless links vary with both distance and average wind speed across a typical suburban macrocell.

1.4 Polarization Dispersion on Fixed Wireless Channel at 1.9GHz

As wireless signals traverse the path from a transmitter to a receiver in suburban macrocell environments, they are diffracted and scattered by buildings, foliage and other obstructions along the path. The manner in which such interaction with the environment alters the polarization state of the wireless signal over time has attracted much interest over the years. Most previous work has characterized polarization diversity on fixed wireless links in terms of the fading statistics on each branch and the cross-correlation coefficient between the time-varying components, *e.g.,* [6]. Such a characterization is particularly useful because the results can be used directly in channel simulations. However, the traditional approach suffers from two significant limitations: (1) the results are generally specific to receiving branches with specified polarization states and (2) the results offer little physical insight concerning such issues as the degree of isolation between orthogonally polarized channels or XPD.

A complementary approach, which provides physical insight and which is independent of the polarization states of the diversity receiving antennas, is to characterize the manner in which polarization states disperse across the Poincaré sphere over time, *i.e.*, to determine the mean and shape of the corresponding polarization state distribution. The notion that it may be useful to consider the manner in which polarization states disperse across the Poincaré sphere has previously been considered in applications as diverse as wireless propagation [25] and radio astronomy [26]. To the best of our knowledge, however, we are the first to use this approach to characterize diversity fading channels and XPD.

We used simulations of ideal Ricean channels to show that: (1) the distribution of polarization states across the Poincaré sphere, as observed at the receiver, is very well approximated by a Fisher or spherical normal distribution over most values of the Ricean K-factor and cross-correlation coefficient, (2) the Fisher concentration parameter κ is a useful measure of the extent of such polarization state dispersion, (3) κ is completely determined by the fading statistics on each branch and the cross-correlation coefficient between the time-varying components, and (4) in the general case, κ provides a better prediction of the level of XPD than does the Ricean K factor.

We have also characterized the manner in which the polarization states observed on 1.9 GHz fixed wireless uplink channels disperse across the Poincaré sphere during short-term measurement sessions conducted at 95 different locations in a suburban macrocell environment. Based on our results, we found that: (1) The mean polarization state is dispersed about the vertical polarization state of the transmitter and tends to follow a Fisher or spherical normal distribution with a concentration parameter κ_m of approximately 3.4. (2) Regardless of the offset between the mean polarization state and the polarization state of the transmitter, the polarization states are symmetrically distributed about the mean polarization state and tend to be well approximated by a Fisher distribution with a concentration parameter κ. (3) The Fisher concentration parameter expressed in dB is well-described by a Gumbel (minimum) distribution over all measurement locations, (4) positively correlated with both Ricean K-factor (in dB) and the level of cross-polar discrimination (XPD) on the channel (in dB) and (5) negatively correlated with average speed of the wind blowing through foliage along the path. Moreover, as we have previously found in the case of simulated channels, XPD is more closely correlated with κ than the Ricean K-factor. Average wind speed is equally well correlated with κ and the Ricean K-factor.

1.5 Thesis outline

This thesis is organized as follows. In Chapter 2, we show that how fading on fixed wireless links in suburban macrocell environments increases with both distance and frequency in a data set that ranged from 1 to 4 km and from 220 MHz to 2 GHz. In Chapter 3, we show how rate of fading on fixed wireless links in suburban macrocell environments is affected with both distance and wind speed in a data set that ranged from 0.5 to 1.5 km at 1.9 GHz. In Chapter 4, we show that how the rate of fading on fixed wireless links in suburban macrocell environments is affected with both distance and frequency in a data set that ranged from 1 to 4 km and from 220 MHz to 2 GHz. In Chapter 5, we present a first-order simulation model for depolarization of propagating signals by narrowband Ricean fading channels. In

Chapter 6, we show how wind blowing through foliage causes the polarization states observed at the receiver to disperse across the Poincaré sphere in a statistically predictable manner. Finally, in Chapter 7, we draw conclusions, assess the contributions and limitations of the work, and recommend some future work.

References

[1] W. Webb, "Broadband fixed wireless access as a key component of the future integrated communications environment," *IEEE Commun. Mag.,* vol. 39, no. 9, pp. 115-121, Sep. 2001.

[2] K. Lu, Y. Qian and H-H Chen, "Wireless broadband access: WIMAX and beyond," *IEEE Commun. Mag.*, vol. 45, no. 5, pp. 124-130, May 2007.

[3] S. S. Venkata, A. Pahwa, R. E. Brown, and R. D. Christie, "What future distribution engineers need to learn," *IEEE Trans. Power Syst.*, vol.19, no.1, pp. 17-23, Feb. 2004.

[4] G. Simard and D. Chartrand, "Hydro-Quebec's Economic and Technical Approach to Justify its Distribution Automation Program," in *Proc. IEEE PES'07,* pp. 1-5, 24-28 Jun. 2007.

[5] S. Jim, W. Carr, and S. E. Collier, "Real time distribution analysis for electric utilities," in *Proc. IEEE REPC'08,* pp. B5-B5-8, 27-29 Apr. 2008.

[6] D. G. Michelson, V. Erceg, and L. J. Greenstein, "Modeling diversity reception over narrowband fixed wireless channels," in *Proc. IEEE MTT-TWA'99*, pp. 95-100, 21-24 Feb. 1999.

[7] L. J. Greenstein, S. S. Ghassemzadeh, V. Erceg and D. G. Michelson, "Ricean K-factors in narrowband fixed wireless channels: Theory, experiments and statistical models," in *Proc. WPMC'99*, 21-23 Sep. 1999.

[8] S. Perras and L. Bouchard, "Fading characteristics of RF signals due to foliage in frequency bands from 2 to 60 GHz," in *Proc. WPMC'02*, 27-30 Oct. 2002, pp. 267-271.

[9] M. J. Gans, N. Amitay, Y. S. Yeh, T. C. Damen, R. A. Valenzuela, C. Cheon and J. Lee, "Propagation measurements for fixed wireless loops (FWL) in a suburban region with foliage and terrain blockages," *IEEE Trans. Wireless Commun.*, vol. 1, no. 2, pp. 302-310, Apr. 2002.

[10] E. R. Pelet, J. E. Salt, and G. Wells, "Effect of wind on foliage obstructed line-of-sight channel at 2.5 GHz," *IEEE Trans. Broadcasting*, vol. 50, no. 3, pp. 224-232, 2004.

[11] D. Crosby, V. S. Abhayawardhana, I. J. Wassell, M. G. Brown, and M. P. Sellars, "Time variability of the foliated fixed wireless access channel at 3.5 GHz," in *Proc. IEEE VTC 2005 Spring*, 25-28 Sep. 2005, pp. 106-110.

[12] R. Feick, R. A. Valenzuela and L. Ahumada, "Experiment results on the level crossing rate and average fade duration for urban fixed wireless channels," *IEEE Trans. Commun.,* vol. 9, no. 1, pp. 175-179, Jan. 2007.

[13] H. Suzuki, C. D. Wilson, and K. Ziri-Castro, "Time variation characteristics of wireless broadband channel in urban area," presented at *EuCAP'06*, Nice, France, 2-6 Nov. 2006.

[14] "Policy for the Use of 700 MHz Systems for Public Safety Applications and Other Limited Use of Broadcasting Spectrum," Industry Canada Radio Systems Policy, RP-006 – Issue 1, Jun. 2006.

[15] "Proposals and Changes to the Spectrum in Certain Bands below 1.7 GHz," Industry Canada Gazette Notice DGTP-004-05, Dec. 2005.

[16] M. Hata, "Empirical formula for propagation loss in land mobile radio services," *IEEE Trans. Veh. Technol.,* vol. 29, no. 3, pp. 317-325, Aug. 1980.

[17] E. Damosso, Ed., "Digital Mobile Radio Toward Future Generation Systems - Final Report," COST 231 Final Report, 1996.

[18] V. Erceg, L. J. Greenstein, S. Y. Tjandra, S.R. Parkoff, A. Gupta, B. Kulic, A. A. Julius, and R. Bianchi, "An empirically based path loss model for wireless channels in suburban environments," *IEEE J. Sel. Areas Commun.,* vol. 17, no. 7, pp. 1205-1211, July 1999.

[19] Y. H. Lee and Y. S. Meng, "Tropical weather effects on foliage propagation," in *Proc. EuCAP '07,* 11-16 Nov. 2007, pp. 1-5.

[20] R. Feick, R. A. Valenzuela and L. Ahumada, "Experiment results on the level crossing rate and average fade duration for urban fixed wireless channels," *IEEE Trans. Commun.,* vol. 9, no. 1, pp. 175-179, Jan. 2007.

[21] S. Thoen, , L. V. D. Perre, and M. Engels, "Modeling the channel time-variance for fixed wireless communications," *IEEE Communic. Lett.*, vol. 6, no. 8, pp. 331-333, Aug. 2002.

[22] H. Suzuki, C. D. Wilson, and K. Ziri-Castro, "Time variation characteristics of wireless broadband channel in urban area," presented at *EuCAP '06*, Nice, France, 2-6 Nov. 2006.

[23] "Policy for the Use of 700 MHz Systems for Public Safety Applications and Other Limited Use of Broadcasting Spectrum," Industry Canada Radio Systems Policy, RP-006 – Issue 1, Jun. 2006.

[24] "Proposals and Changes to the Spectrum in Certain Bands below 1.7 GHz," Industry Canada Gazette Notice DGTP-004-05, Dec. 2005.

[25] D. J. Cichon, T. Kurner and W. Wiesbeck, "Polarimetric aspects in antenna related superposition of multipath signals," *Proc. ICAP 1993*, pp. 80-83, 30 Mar. – 2 Apr.1993.

[26] M. M. McKinnon, "Three-dimensional statistics of radio polarimetry," *Astrophys. J. Suppl.,* vol. 148, no. 2, pp. 519-526, Oct. 2003.

2 Characterization of Fading on Fixed Wireless Channels between 220 MHz and 2GHz in Suburban Macrocell Environment[1]

2.1 Introduction

Fixed wireless technology has attracted considerable interest in recent years as: (1) common carriers seek methods for providing either fixed or nomadic network access services to residential households without the expense of deploying wireline connectivity over the last mile [1], [2] and (2) as public utilities seek methods that will allow them to: (a) detect and report outages, (b) monitor usage, and (c) implement strategies that encourage customers to limit consumption and adopt sustainable practices [3]-[5]. In suburban macrocell environments, *i.e.,* environments in which the base station antenna is mounted well above the local rooftop or treetop level and the remote terminal antenna is mounted below the local rooftop or treetop level, wireless links are usually obstructed by intervening obstacles and a large fraction of the signal that reaches the receiver does so as a result of scattering and diffraction by objects in the environment. Because both the transmitting and receiving antennas in such applications are fixed, signal fading is caused solely by the motion of objects in the environment that scatter and diffract the signal. In suburban macrocell environments, a large fraction of those objects are trees and foliage with leaves and branches that sway when blown by the wind.

During the past decade, groups in Canada, the United States, the United Kingdom, Chile, Australia and elsewhere have conducted measurement campaigns aimed at characterizing the manner in which signal fading occurs on non-line-of-sight (NLOS) paths in macrocell environments, *e.g.,* [6]-[13]. Such studies have variously sought to characterize: (1) the first-order statistics of the fading signal envelope over time and location, (2) the rate at which the signal fades, either through direct estimation of the Doppler spectrum or through estimation of the average fade duration and level crossing rate, (3) the effect of the height and beamwidth of the receiving antenna, local density of

[1] A ver sion of this chapter has been submitted for publication: A. Liou, K. N. Sivertsen, P. Arjmandi, G. Viswanathan, B. Diallo, S. Lancashire, and D.G. Michelson, "Characterization of Fading on Fixed Wireless Channels between 200 MHz and 2 GHz in Suburban Macrocell Environments."

vegetation and the wind speed in the vicinity, and (4) the performance of space and polarization diversity at either the base station or the remote terminal.

The vast majority of previous studies of fixed wireless channels in suburban macrocell environments focused on individual frequency bands at 1.9 GHz and above, including the PCS band at 1.9 GHz, the ISM band at 2.45 GHz, the Fixed Wireless Access (FWA) band at 3.5 GHz and the U-NII and ISM bands at 5.2 and 5.8 GHz. However, spectrum regulators have recently begun to reallocate frequency bands below 2 GHz in order to help meet the requirements for broadband wireless access for urban and rural areas and/or narrowband telemetry for public utilities. In Canada, spectrum in frequency bands near 700 MHz has been proposed for fixed wireless broadband use in rural areas [14] and may find application in distribution automation by the electrical power industry. Frequency bands such as 220–222 MHz and 1429.5–1432 MHz have recently been designated for utility telemetry and distribution automation [15]. Regulators are increasingly designating multiple primary allocations within individual frequency bands, as well as proposing more flexible licensing schemes, in an attempt to accommodate different users and services in the same spectrum. Both the amount of radio spectrum, and the choice of frequency bands available for fixed wireless use, will almost certainly increase in coming years.

The manner in which path loss, or its reciprocal, path gain, is affected by the carrier frequency, the heights of and separation between the base station and mobile terminal in suburban macrocell environments over the range from 200 MHz to 2 GHz has been well-studied over the years and has been captured by several standard models [16]-[18]. However, existing channel models do not provide a description of the depth of signal fading that fixed wireless channels will experience over this frequency range in suburban macrocell environments. (Ref. [19] describes fading on UHF links between fixed nodes within a tropical rain forest but the link configuration (both nodes were located below the forest canopy) was quite different from that encountered in suburban macrocells.) This lack of information places those charged with planning, simulating or deploying fixed wireless systems in suburban macrocell environments at a severe disadvantage when asked to predict system coverage and outage probabilities.

Here, we take the first steps to develop measurement-based fading channel models suitable for use across the frequency range from 200 MHz to 2 GHz. We established a transmitting site atop an eighteen-storey office tower located in the middle of a large suburban area. We simultaneously broadcast single carrier signals in the 220, 850 and 1900 MHz bands and collected time-series of the received signal strength observed in each band at fixed locations at ranges between 1 and 4 km. We reduced the data in order to determine the manner in which path gain and signal fading vary with distance, time-averaged wind speed and carrier frequency in a typical suburban macrocell environment. The resulting measurement-based model allows the coverage and outage probability in a typical macrocell environment to be compared. The frequencies that we employed bracket the majority of the bands that have been allocated to fixed wireless access and SCADA (supervisory control and data acquisition) applications. Although our results strictly apply to narrowband channels, they are also relevant to single carriers in multicarrier modulation schemes. The results presented here are specific to high transmitting sites; in future work, we shall determine how lowering the base station height affects the results.

2.2 The Narrowband Fading Channel Model

The essential aspects of fading on narrowband fixed wireless channels have been described previously in [6], [7] and [20]. The complex signal path gain of a narrowband channel (typically tens of kHz wide) over a given time interval (typically several minutes long) is given by

$$g(t) = V + v(t), \tag{2.1}$$

where V is a complex number and $v(t)$ is a complex, zero-mean random time variation caused by windblown foliage, vehicular traffic, *etc.* Both V and the parameters of the random process $v(t)$ may change from one time-frequency segment to another.

From time series data collected over a given time-frequency segment, we can calculate the average power gain

$$G = \overline{|g(t)|^2} = |V|^2 + \overline{|v(t)|^2} = |V|^2 + \sigma^2, \tag{2.2}$$

where σ^2 is the variance of the complex Gaussian process. The rms fluctuation of the envelope about the mean is given by the standard deviation of $|g(t)|^2$ and is denoted by σ_G. Because experience has shown that $v(t)$ is a complex Gaussian process, the distribution of $|g(t)|^2$ over time is Ricean. The K-factor of the distribution is given by

$$K = |V|^2 / \overline{|v(t)|^2} = |V|^2 / \sigma^2. \tag{2.3}$$

Various methods for estimating K have been proposed; we use the moment-based method described in [20] where

$$K = \frac{|V|^2}{\sigma^2} = \frac{\sqrt{G^2 - \sigma_G^2}}{G - \sqrt{G^2 - \sigma_G^2}}. \tag{2.4}$$

In terms of G and K, the expression for $g(t)$ in (2.1) can be re-cast as

$$g(t) = \sqrt{\frac{G}{K+1}}\left[\sqrt{K}e^{j\Psi} + x(t)\right], \tag{2.5}$$

where Ψ is the phase of V and $x(t)$ is a zero-mean complex Gaussian process with a unit standard deviation. From (2.5), the channel parameters G and K completely specify the first-order statistics of the signal at a given location over time intervals of several minutes.

Knowledge of the first order statistics of signal fading is sufficient to predict the probability of the link experiencing a given fade depth or outage. Further, it has been observed that the level of cross-polar discrimination (XPD) on the channel is highly correlated with Ricean K-factor [21]. Previous measurements in suburban macrocell environments at frequencies above 1.5 GHz have shown that on Ricean channels, G and K are both well-modeled by Gaussian distributions when they are expressed in dB, *e.g.,* [6]. The implication of this result is that these parameters can be modeled and simulated as a set of Gaussian variates whose joint distribution is completely determined by their means, standard deviations and mutual correlation coefficients. In the sections that follow, we describe our efforts to characterize the parameters of this first-order model in a typical suburban macrocell.

2.3 The Measurement Setup

2.3.1 Tri-band Channel Sounder

Our tri-band channel sounder consists of a multiband continuous wave (CW) transmitter and receiver that operate in the 220, 850 and 1900 MHz frequency bands. A block diagram of the CW transmitter is shown in Figure 2.1(a). The signal source portion of the transmitter contains a pair of Marconi 2022 RF signal generators, each of which is capable of supplying a CW signal up to 6 dBm over the range 10 kHz to 1 GHz, and a Marconi 2031 RF signal generator capable of supplying a CW signal up to 13 dBm over the range 10 kHz to 2.7 GHz. The signal generators are locked to a 10 MHz reference signal supplied by a Stanford Research Systems PRS10 Rubidium frequency standard. It, in turn, is disciplined by the 1 PPS signal supplied by a Trimble Resolution-T GPS receiver that has been designed for such applications.

The amplifier portion contains three power amplifiers: (1) a TPL Communications LMS series RF power amplifier capable of delivering between 20 and 100 W at 220 MHz, (2) a Unity Wireless Dragon RF power amplifier capable of delivering up to 30 W between 869 and 894 MHz and (3) a Unity Wireless Grizzly RF power amplifier capable of delivering up to 35 W between 1930 and 1990 MHz. During data collection, all three amplifiers were configured to deliver 20 W signals to their respective feedlines. A wireless remote control device that operates near 150 MHz allowed the data collection team to remotely enable or disable the power amplifiers at the start or end of a measurement session. The 220, 850 and 1900 MHz transmitting antennas are omnidirectional and have gains of 8.1, 6.1 and 5.0 dBi, respectively. They were installed atop the eighteen-storey office tower at BC Hydro's Edmonds facility in Burnaby, BC at a height of 80 m above ground level. The remaining parameters used in the system link budget for each band are given in Table 2.1.

A block diagram of our multiband receiver is shown in Figure 2.1(b). The receiving antennas are omnidirectional and all have the same nominal gain of 1 dBi. When used in NLOS configurations, fixed wireless antennas are typically mounted at heights between 0.5 m (*e.g.*, for nomadic applications) and 4 m (*e.g.*, for permanent installations). As a compromise, we mounted the antennas on the roof of our propagation measurement van at a height of 2.3 m. In many cases, fixed wireless antennas are directional. Because our primary objective is to compare the behaviour of the channel at different frequencies, we elected to simplify the data collection protocol by collecting the measurement data using omnidirectional antennas. If the remote terminal antenna's beamwidth decreased or its height is increased, the path gain and/or the Ricean K-factor will tend to increase [7].

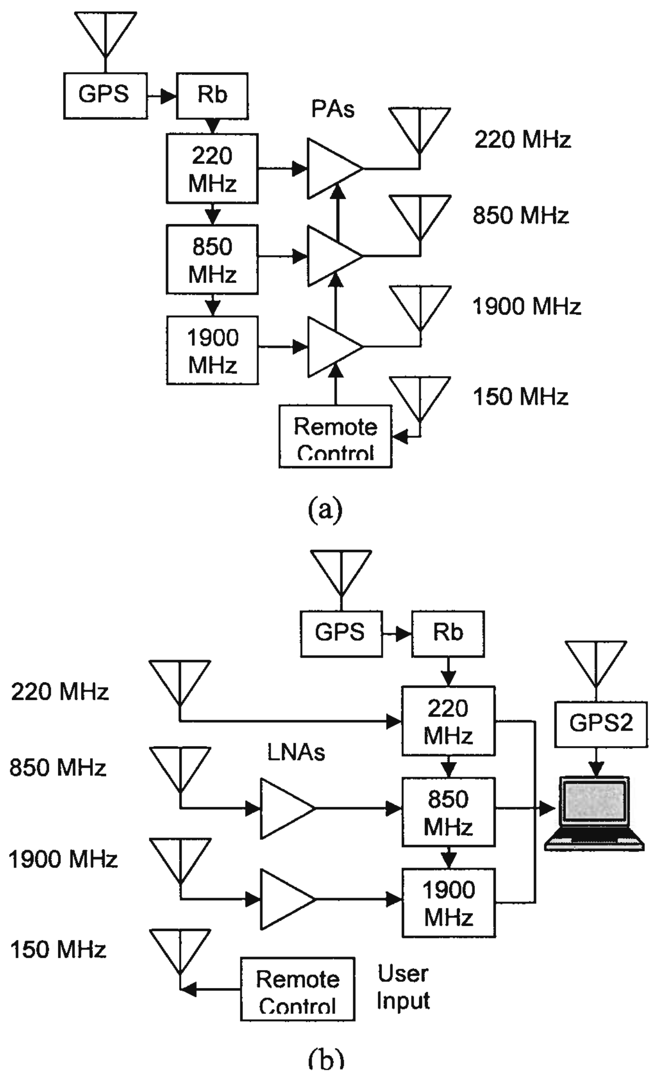

Figure 2.1 – (a) The tri-band transmitter that was deployed at the base station and (b) the tri-band receiver that was carried aboard the propagation measurement van.

Table 2.1 – Link Budget Parameters for the Tri-band Channel Sounder.

Parameter	220 MHz	850 MHz	1900 MHz
Transmitted Power	43 dBm	43 dBm	43 dBm
Transmit Cable Loss	1.3 dB	2.7 dB	4.3 dB
Transmit Antenna Gain	8.1 dBi	6.1 dBi	5 dBi
Receive Antenna Gain	1 dBi	1 dBi	1 dBi
Receive Cable Loss	0.37 dB	0.76 dB	1.2 dB
Receiver LNA Gain	-	30 dB	26 dB

The multiband receiver consists of: (1) a pair of Anritsu MS2651B spectrum analyzers that operate over the range of 9 kHz to 3 GHz with a selectable IF bandwidth, (2) an Anritsu MS2721A spectrum analyzer that operates over the range of 100 kHz to 7.1 GHz with a selectable IF bandwidth , (3) a Stanford Research Systems PRS10 Rubidium frequency standard that generates a 10 MHz reference signal to which the spectrum analyzers can be locked and (4) a Trimble Resolution-T GPS receiver that supplies the 1 PPS signal used to discipline the frequency standard. External low-noise pre-amplifiers with 30 dB and 26 dB gain were used to increase the sensitivity of the spectrum analyzers that measure the received strength of the 850 and 1900 MHz signals, respectively. We used a laptop computer equipped with a GPIB adapter to: (1) configure the spectrum analyzers and (2) collect data from them. We geocoded the data with a nominal circular error probability (CEP) of less than 5 metres using location information supplied by a u-blox Antaris 4 SuperSense GPS receiver.

2.3.2 Verification Protocol

Before we collected any field data, we verified the function and operation of our tri-band CW channel sounder using a Spirent SR5500 channel emulator. We set the relevant narrowband channel parameters, including path gain and Ricean K-factor, to various values over a broad range and, in each case, confirmed that we were able to correctly estimate each of the parameters. We verified the transmitted power levels using a Bird Model 5000EX digital wattmeter.

2.3.3 Weather Instrument

We measured the wind speed, wind direction, rain rate and outdoor temperature using a Davis Vantage Pro 2 wireless weather station that we mounted on a mast located about 30 metres away from the transmitting antennas. Internally, the weather station samples the relevant weather parameters every few seconds. Once per minute, it logs the average values of these parameters over the previous minute to an internal database. We used a custom software tool to match the received signal strength data collected at a given location to the relevant weather data. Because previous work has shown that variations in average wind speed at tree top level or above are well correlated over mesoscale distances of several kilometers [22], we concluded that collecting wind data at a single location near the base station would be adequate for our purposes.

2.3.4 Test Area

Our test area consisted of suburban neighbourhoods with generally flat terrain, light to moderate foliage and one- and two-storey houses. We collected measurement data at 84 fixed measurement locations that were situated within an annulus between 1 and 4 km from the transmitter site. Almost all the motion in the environment arose from windblown foliage; few, if any, cars, people or other moving scatterers were in the vicinity when we collected measurement data. Most of the foliage in the area is deciduous and between 4 and 7 m in height but at least one-third is coniferous and up to 15 m in height. The duration of the measurement campaign was too short to permit observation of the effects of seasonal variations in the foliage. All of our data was collected with leaves on the trees.

2.3.5 Data Collection Protocol

Our data collection protocol comprised the following steps. First, we conducted a rapid survey of the proposed measurement locations in order to ensure that the strength of the received signal would be adequate at all locations. Next, over a span of several days, the operator drove the propagation measurement van to each of the fixed measurement locations that we had selected in advance. At each location, the operator collected simultaneous time series of the received strength of the 220, 850 and 1900 MHz CW signals. The measured data were collected in the form of three successive 120 second sweeps. For the two upper bands, the pair of Anritsu MS2651B spectrum analyzers were used to record three sweeps of 501 samples each, yielding 1503 received signal strength samples at each location. For the 220 MHz band, the Anritsu MS2721A spectrum analyzer was used; it yielded 551 samples per sweep or 1653 samples at each location.

Time-series recordings of received signal strength of 6 minutes in duration as measured at a typical location at a distance of 1.44 km from the transmitting site are shown in Figure 2.2. The upper trace is the 220 MHz received signal; its average received signal strength is -47 dBm and its Ricean K-factor is 24.2 dB. The lower trace is the 1900 MHz received signal; its average received signal strength is -53 dBm and its Ricean K-factor is just 7.4 dB. The K-factor values are very similar to the averages over all locations at each frequency. The greater severity of the signal fading at 1900 MHz compared to 220 MHz is apparent.

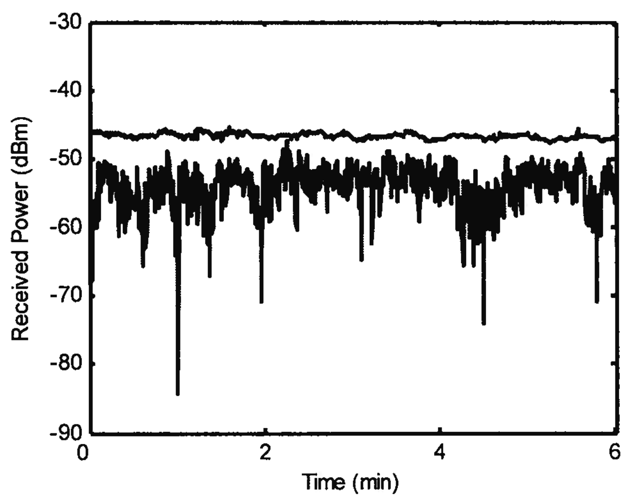

Figure 2.2 – Typical time series of received signal strength at 220 MHz (top) and 1900 MHz (bottom) with Ricean K-factors of 24.2 and 7.4 dB, respectively.

2.4 Results

2.4.1 Distribution of Ricean K-factors

Over the 84 measurement locations and in all three frequency bands, the fading distributions experienced by the received signal are well approximated by Ricean distributions. The Ricean K-factors in each band tend to follow a lognormal distribution (*i.e.,* normal in dB), as suggested by Figure 2.3. The mean values of K are strongly dependent on the frequency band with $\overline{K}_{220} = 23$ dB >> $\overline{K}_{850} = 11.2$ dB > $\overline{K}_{1900} = 7.7$ dB. Although our results are only based upon three frequencies, we made a preliminary attempt to use regression analysis to determine the relationship between $\overline{K}$ and the carrier frequency. The resulting regression line is shown in Figure 2.4 and is given by

$$\overline{K}(\mathrm{dB}) = -16.6\log_{10}(f) + 61.5, \tag{2.6}$$

where $\overline{K}$ is expressed in dB and the carrier frequency f is expressed in MHz. The variability of K over all locations at each frequency is remarkably similar and falls between 6.8 and 8.3 dB, a range of less than 1.5 dB. Although these results should be regarded as preliminary because they are based upon only three frequencies, the trend is consistent with the notion that $\overline{K}$ is inversely proportional to $\log_{10}(f)$. It also suggests that the frequency dependence of $\overline{K}$ be investigated further.

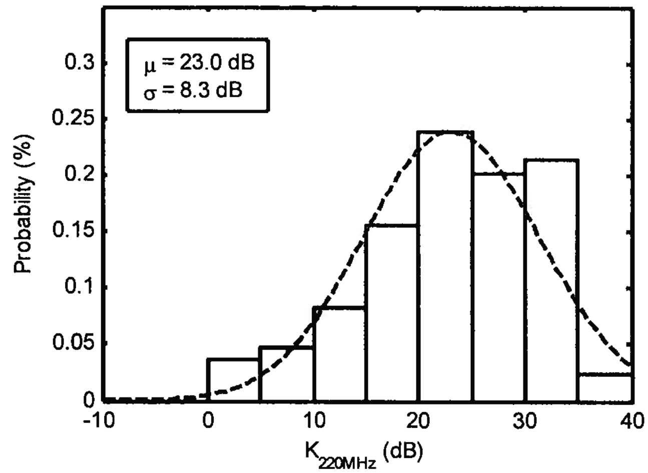

(a)

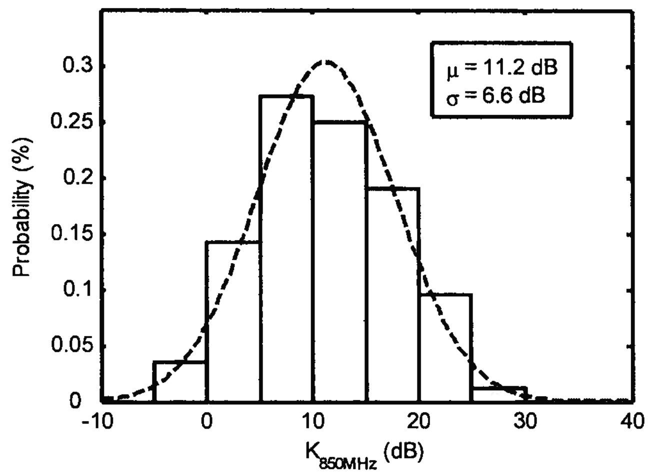

(b)

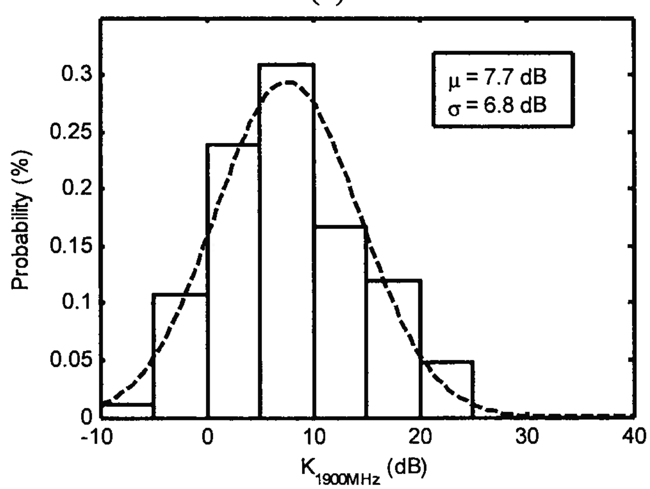

(c)

Figure 2.3 – Distribution of Ricean K-factors observed throughout the test area at (a) 200MHz, (b) 850MHz, and (c) 1900MHz.

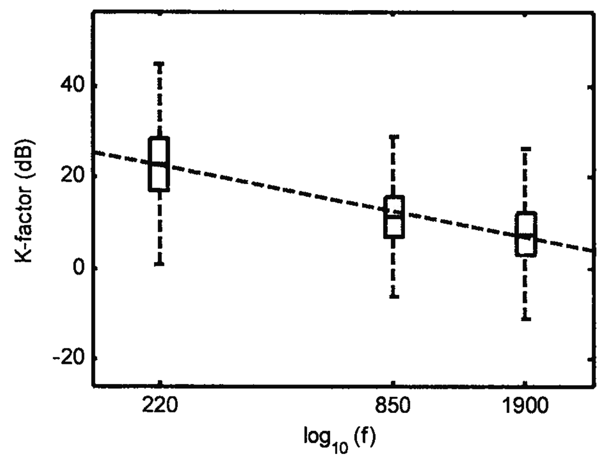

Figure 2.4 – Regression analysis of Ricean K-factors vs. carrier frequency in MHz. The distribution of K at 220, 850 and 1900 MHz is indicated by a box plot.

If, as seems likely, the scattered component of the received signal is the result of scattering by windblown trees and foliage, the frequency dependence of the severity of fading can likely be explained by considering the displacement of the moving scatterers in terms of the wavelength of the signal. As wavelength increases, a given displacement of leaves and branches by the wind will lead to a much smaller phase shift of the scattered signal and a much lower probability of deep fades occurring at the receiver. In [23], [24] and [25], the first attempts to formulate physical models capable of predicting and/or simulating fading on fixed wireless channels due to moving vegetation were reported. Development of a more sophisticated physical model that captures the frequency dependence of fading reported here is an obvious next step.

2.4.2 Path Gain and Ricean K-factors vs. Distance

We used (2.2) and (2.4) to estimate the values of G and K, respectively, that describe the set of time series data collected at each location, then plotted the results *vs*. the distance between the transmitter and the receiver. Path gain and Ricean K-factor both decrease with distance according to a power law relationship as suggested by Figures 2.5(a) and (b). We characterized the distance dependence of G and K by estimating the regression line that best fits the measured data. We also estimated the correlation coefficients ρ between each parameter and distance d and estimated the location variability σ of the parameter, *i.e.*, the variation of the parameter about the regression line. The regression lines for G and K and the corresponding correlation coefficients ρ and location variabilities σ in each frequency band are given by

$$\bar{G}_{220}(\mathrm{dB}) = -33.5\log_{10} d - 92.3; \qquad \rho = -0.59, \quad \sigma = 7.2, \tag{2.7}$$

$$\bar{G}_{850}(\mathrm{dB}) = -37\log_{10} d - 108.4; \qquad \rho = -0.64, \quad \sigma = 6.9, \tag{2.8}$$

$$\bar{G}_{1900}(\mathrm{dB}) = -36\log_{10} d - 114.7; \qquad \rho = -0.58, \quad \sigma = 7.9, \tag{2.9}$$

and

$$\bar{K}_{220}(\mathrm{dB}) = -8.0\log_{10} d + 25.8; \qquad \rho = -0.15, \quad \sigma = 8.3, \tag{2.10}$$

$$\bar{K}_{850}(\mathrm{dB}) = -4.9\log_{10} d + 12.9; \qquad \rho = -0.12, \quad \sigma = 6.5, \tag{2.11}$$

$$\bar{K}_{1900}(\mathrm{dB}) = -8.5\log_{10} d + 10.5; \qquad \rho = -0.19, \quad \sigma = 6.7, \tag{2.12}$$

respectively, where the parameters' subscript indicate the relevant frequency band in MHz and all values of σ are given in dB. For simplicity, subscripts have not been added to either ρ or σ; it is understood that each instance applies only to the corresponding regression line.

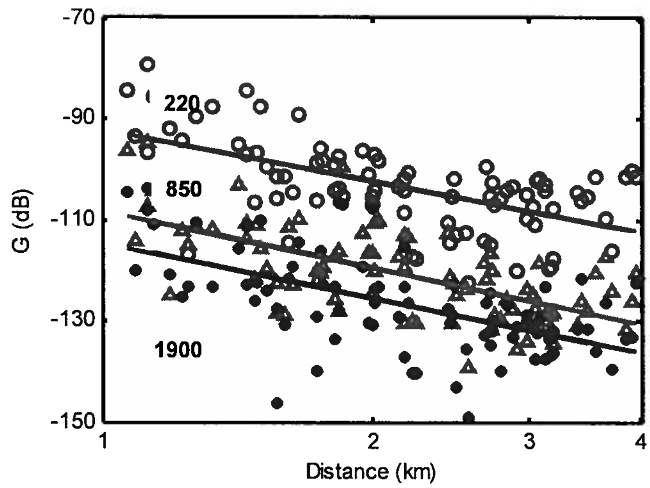

(a)

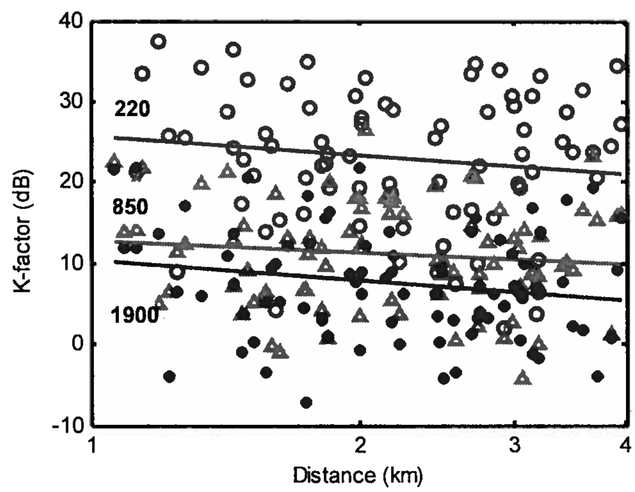

(b)

Figure 2.5 – (a) Average path gain G and (b) Ricean K-factors observed at 220 (O), 850 (Δ), and 1900 ($\bullet$) MHz *vs.* distance.

Path gain changes with distance and frequency in the general manner predicted by standard models. The distance coefficients in (2.7)-(2.9) are 33.5, 37 and 36, respectively. They are higher than but comparable to the value of 32 that the Okumura-Hata/COST-231 model predicts for a high transmitting site and light-to-moderate foliage with gentle terrain in the coverage area [16]. We also note that the exponent increases slightly as the frequency increases. In general, approximately two-thirds of the differences in path gain (in dB) between frequencies can be attributed to the reduction in the effective area of the receiving antenna as frequency increases. The remaining third can likely be attributed to increased diffraction losses as the frequency increases. For a given distance d, $\bar{K}_{220}(d) >> \bar{K}_{850}(d) > \bar{K}_{1950}(d)$. Moreover, K falls off with increasing distance, but at a much slower rate than path gain. The location variability of K is comparable to that of path gain.

2.4.3 Fixed and Scattered Path Gain vs. Distance

Our second set of reductions involved estimating the fixed path gain G_f and the scattered path gain G_s associated with the set of time series data collected at each location. These parameters are given by the numerator and denominator of (2.4), respectively, so provide insight into the behavior of K. Because fixed path gain tends to be determined by the configuration of obstacles along the direct path between the base and remote terminal while scattered path gain is the result of scattering over a broad range of angles about the remote terminal, we anticipated that G_f would roll off with distance more quickly and experience greater location variability than G_s. However, few previous studies have either verified these trends or quantified them. We plotted the results *vs.* the distance between the transmitter and receiver; the results are presented in Figures 2.6(a) and (b).

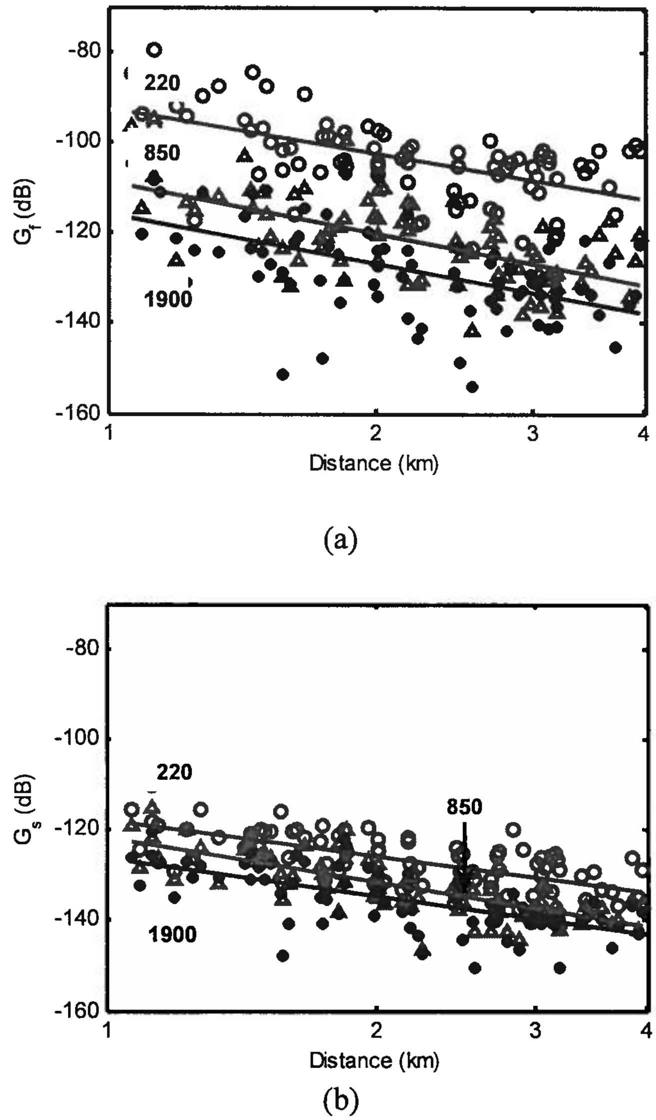

Figure 2.6– (a) Fixed path gain G_f and (b) scattered path gain G_s observed at 220 (O), 850 (Δ), and 1900 (●) MHz *vs.* distance.

Fixed and scattered path gain both decrease with distance according to a power law relationship. The regression lines for G_f and G_s and the corresponding correlation coefficients and location variabilities in each frequency band are given by

$$\bar{G}_{f\_220}(dB) = -33.8\log_{10} d - 92.3; \qquad \rho = -0.58, \ \sigma = 7.4, \qquad (2.13)$$

$$\bar{G}_{f\_850}(dB) = -37.6\log_{10} d - 108.9; \qquad \rho = -0.61, \ \sigma = 7.5, \qquad (2.14)$$

$$\bar{G}_{f\_1900}(dB) = -36.9\log_{10} d - 115.7; \qquad \rho = -0.53, \ \sigma = 9.1, \qquad (2.15)$$

and

$$\bar{G}_{s\_220}(dB) = -25.8\log_{10} d - 118.1; \qquad \rho = -0.65, \ \sigma = 4.7, \qquad (2.16)$$

$$\bar{G}_{s\_850}(dB) = -32.7\log_{10} d - 121.7; \qquad \rho = -0.77, \ \sigma = 4.2, \qquad (2.17)$$

$$\bar{G}_{s\_1900}(dB) = -28.4\log_{10} d - 126.2; \qquad \rho = -0.67, \ \sigma = 4.9, \qquad (2.18)$$

respectively. Once again, the subscripts indicate the relevant frequency in MHz and all values of σ are given in dB. Also, subscripts have not been added to either ρ or σ; it is understood that the values given with the expression for each regression line apply to that regression line.

Three trends are immediately apparent: (1) At all three frequencies, the fixed path gain falls off with distance more quickly than does the scattered path gain. This, of course, is what causes K-factor to decrease as distance increases. (2) At all three frequencies, the location variability of scattered path gain is between 2.5 and 4 dB less than the location variability of the corresponding fixed path gain. This is consistent with our physical understanding of the nature of fixed and scattered path gains, as summarized earlier in this section. (3) At a given distance, the mean scattered path gain at each frequency is only a few dB different from those at other frequencies. The differences between the corresponding fixed path gains are far greater.

If one normalizes the path gains by removing the frequency-squared dependence of the free space path loss component, two further trends are apparent: (1) the normalized fixed path gain at lower frequencies is greater than at higher frequencies, likely because diffraction losses are less and (2) the normalized scattered path gain at lower frequencies is less than at higher frequencies, likely because the obstructions and scatterers in the environment are smaller in terms of wavelength and do not diffract and scatter wireless signals as effectively.

2.4.4 Excess Path Gain and Ricean K-factor as a Function of Average Wind Speed

Our third set of data reductions involved determining how path gain and the Ricean K-factor observed at each location are affected by the time-averaged wind speed v in km/h that we observed in the vicinity of the transmitting site. In order to remove the distance dependence from path gain, we calculated the excess path gain ΔG (or the difference in dB) between the path gain G measured at a given location and the mean value $\overline{G}$ observed at that distance. Because Ricean K-factor depends only weakly on distance, and to be consistent with the approach taken by others, we ignored that distance dependence of K and simply compared K to wind speed. The results are presented in Figures 2.7(a) and (b) while the distribution of average wind speeds that we observed over all measurements is presented in Figure 2.8.

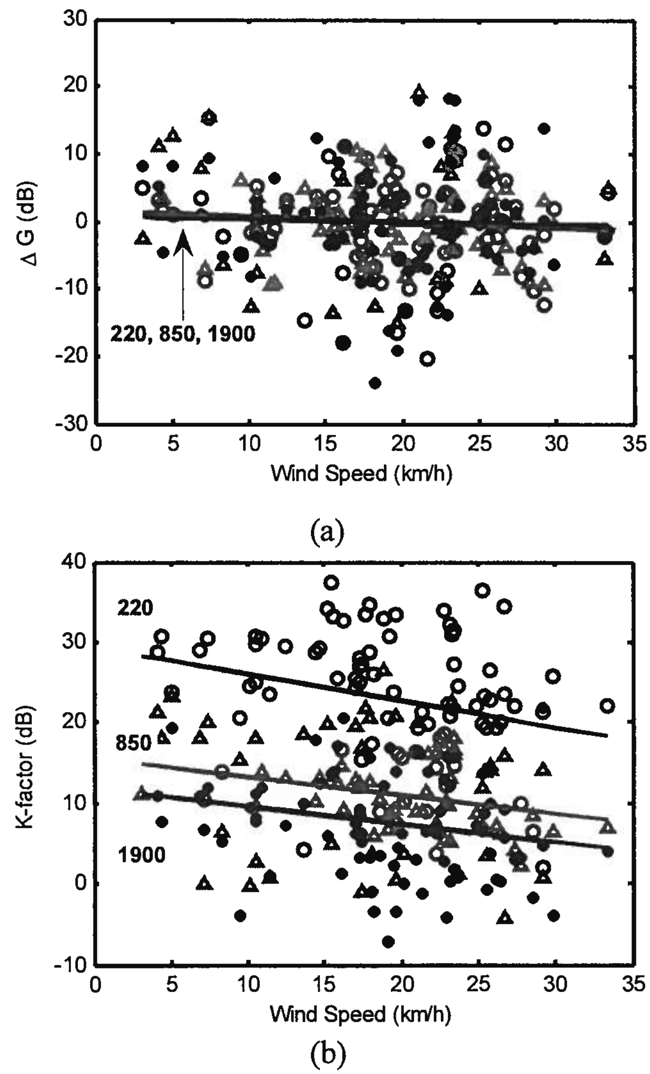

Figure 2.7– (a) Excess path gain and (b) Ricean K-factors observed at 220 (O), 850 (Δ), and 1900 (●) MHz *vs.* averaged wind speed.

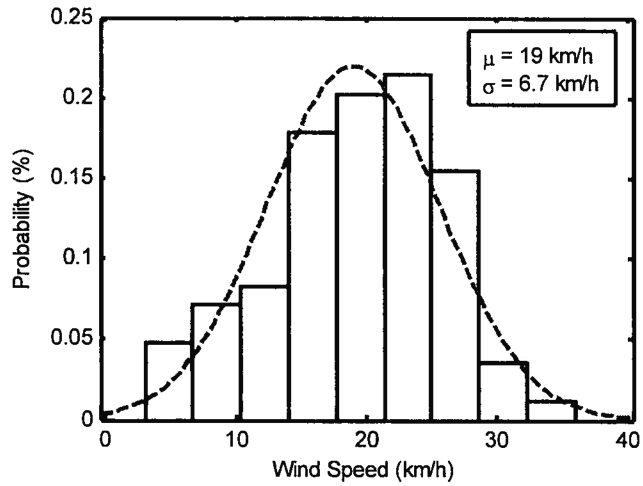

Figure 2.8– The average wind speed distribution observed at the base station during data collection.

We estimated the regression line that best fits the measured data, the correlation coefficient between each parameter and the average wind speed, and the location variability of the parameter, *i.e.,* the variation of the parameter about the regression line at a given average wind speed. The regression lines for ΔG and K and the corresponding correlation coefficients and location variabilities in each frequency band are given by

$$\Delta\overline{G}_{220}(dB) = -0.037v_W + 0.69; \qquad \rho = -0.034,\ \sigma = 7.2, \tag{2.19}$$

$$\Delta\overline{G}_{850}(dB) = -0.058v_W + 1.11; \qquad \rho = -0.057,\ \sigma = 6.9, \tag{2.20}$$

$$\Delta\overline{G}_{1900}(dB) = 0.001v_W - 0.02; \qquad \rho = 0.001,\ \sigma = 7.9, \tag{2.21}$$

and

$$\overline{K}_{220}(dB) = -0.33v_W + 29.4; \qquad \rho = -0.26,\ \sigma = 8.3, \tag{2.22}$$

$$\overline{K}_{850}(dB) = -0.23v_W + 15.5; \qquad \rho = -0.23,\ \sigma = 6.6, \tag{2.23}$$

$$\overline{K}_{1900}(dB) = -0.22v_W + 11.9; \qquad \rho = -0.22,\ \sigma = 6.8, \tag{2.24}$$

respectively, where v_w is expressed in km/h.

As expected, there is no correlation between the excess path gain and average wind speed. Both the moderate negative correlations between the Ricean K-factor and average wind speed and the standard deviations at all three frequencies are comparable to each other. The main differences between (2.22)-(2.24) are the intercepts of the regression lines with the K axis, which decrease as the carrier frequency increases.

2.4.5 Excess Fixed Path Gain and Excess Scatter Path Gain as a Function of Average Wind Speed

Our fourth set of data reductions involved determining how the fixed and scattered path gains are affected by the average wind speed. As in the previous section, we eliminated the distance dependence of path gain by taking the excess value of each parameter or the difference (in dB) between the parameter measured at a given location and the mean value observed at that distance. The results are presented in Figures 2.9(a) and (b).

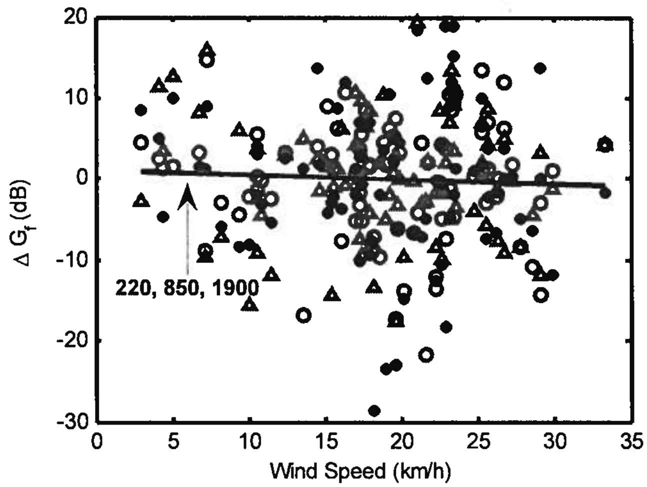

(a)

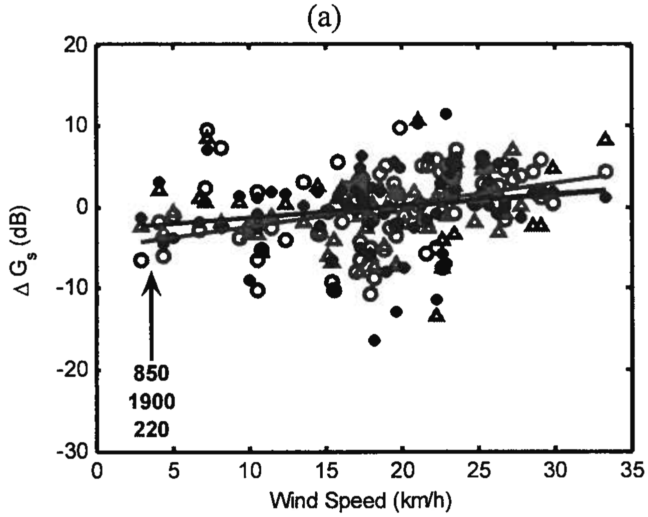

(b)

Figure 2.9– (a) Excess fixed path gain and (b) excess scattered path gain observed at 220 (O), 850 (Δ), and 1900 (•) MHz *vs.* average wind speed.

We estimated the regression line that best fits the measured data, the correlation coefficient between each parameter and the average wind speed, v_w, and the location variability of the parameter, *i.e.,* the variation of the parameter about the regression line at a given average wind speed. The regression lines for ΔG_f and ΔG_s and the corresponding correlation coefficients and location variabilities in each frequency band are given by

$$\Delta\overline{G}_{f\_220}(dB) = -0.044 v_W + 0.84; \qquad \rho = -0.04,\ \sigma = 7.4 \tag{2.25}$$

$$\Delta\overline{G}_{f\_850}(dB) = -0.072 v_W + 1.37; \qquad \rho = -0.064,\ \sigma = 7.5 \tag{2.26}$$

$$\Delta\overline{G}_{f\_1900}(dB) = -0.048 v_W + 0.9; \qquad \rho = -0.035,\ \sigma = 9.1 \tag{2.27}$$

and

$$\Delta\overline{G}_{s\_220}(dB) = 0.26 v_W - 5.0; \qquad \rho = 0.37,\ \sigma = 4.7, \tag{2.28}$$

$$\Delta\overline{G}_{s\_850}(dB) = 0.14 v_W - 2.6; \qquad \rho = 0.22,\ \sigma = 4.2, \tag{2.29}$$

$$\Delta\overline{G}_{s\_1900}(dB) = 0.15 v_W - 2.9; \qquad \rho = 0.21,\ \sigma = 4.9, \tag{2.30}$$

respectively.

As expected, there is no correlation between the excess fixed path gain and average wind speed. In contrast, there is a clear relationship between scattered path gain and wind speed. The moderate positive correlations between the excess scattered path gain and average wind speed at all three frequencies are comparable to each other, as are the standard deviations. The main differences are the intercepts of the regression line with the ΔG_s axis, which generally decreases as the carrier frequency increases.

2.4.6 Joint Dependency of the Excess Path Gain and Ricean K-factor

At a given location, we observed a strong correlation between the excess path gain ΔG and the Ricean K-factor. In order to remove distance effects, we replaced K by the excess Rician K-factor ΔK, i.e., the difference in dB between the Rician K-factor observed at a given location and $\overline{K}(d)$ the mean value at that distance which is given by (2.10)-(2.12) for the three frequency bands that we considered. The results are presented in Figure 2.10(a), (b), and (c). The corresponding regression lines are given by

$$\Delta\bar{K}_{220}(dB) = 0.94\Delta G_{220} + 23.1; \qquad \rho = 0.81, \ \sigma = 4.9, \tag{2.31}$$

$$\Delta\bar{K}_{850}(dB) = 0.75\,\Delta G_{850} + 11.23; \qquad \rho = 0.78, \ \sigma = 4.1, \tag{2.32}$$

$$\Delta\bar{K}_{1900}(dB) = 0.68\,\Delta G_{1900} + 7.6; \qquad \rho = 0.80, \ \sigma = 4.2, \tag{2.33}$$

Because the dependence of K on distance is so much weaker than its dependence on excess path gain, the correlations given in (2.31)-(2.33) are virtually identical to those that we observed between ΔG and K. This correlation between ΔG and ΔK forms the basis for the simulation model that we present in the next section.

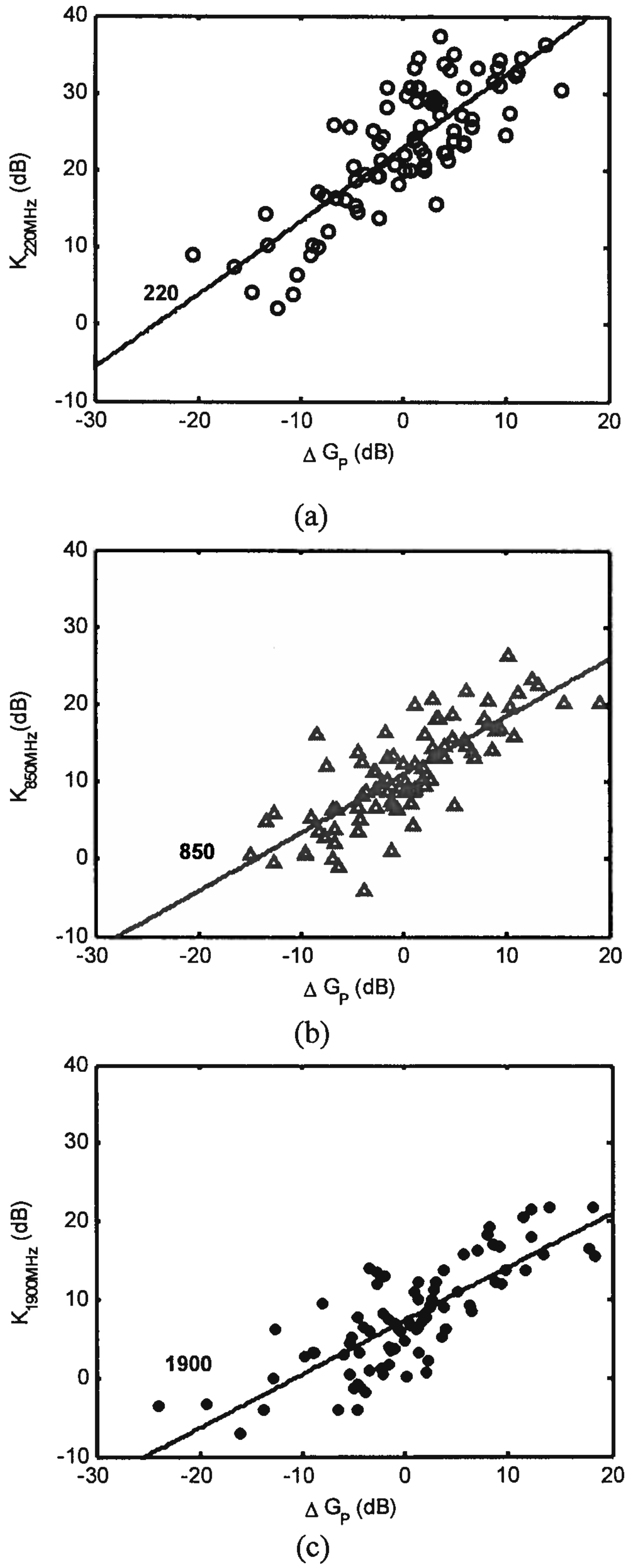

Figure 2.10 – Scatter plots of Ricean K-factor vs. excess path loss at a given distance at (a) 220 (O), (b) 850 (Δ), and (c) 1900 (•) MHz.

2.5 A Simulation Model

In simulations of fixed wireless systems, it may be necessary to generate values of G and K that a link might experience at a particular frequency and distance. Although we do not have any information concerning the correlation between the values of G and K in either time or space, we can easily generate values that have the same *first order* statistics as our measured data. In a particular frequency band, we consider G and K as the sum of: (1) the mean value $\bar{G}$ and $\bar{K}$ at a particular distance d and (2) random components ΔG and ΔK which have zero mean. If, as our results suggest, we can assume that ΔG and ΔK are both normally distributed when expressed in dB, their joint distributions are completely described by their mean values, standard deviations and mutual correlation coefficient. Thus, at a given distance and in a specific frequency band, $G(d)$ and $K(d)$ can be generated by

$$\begin{aligned} G(d) &= \bar{G}(d) + \Delta G \\ &= \bar{G}(d) + \sigma_G U_1 \end{aligned} \tag{2.34}$$

and

$$\begin{aligned} K(d) &= \bar{K}(d) + \Delta K \\ &= \bar{K}(d) + \rho\sigma_K U_1 + \sqrt{1-\rho^2}\,\sigma_K U_2 \end{aligned} \tag{2.35}$$

where σ_G is the σ given in (2.7)-(2.9), σ_K is the σ given in (2.10) -(2.12), ρ is given in (2.31)-(2.33), and U_1 and U_2 are uncorrelated Gaussian random variables with zero mean and unit variance.

2.6 Conclusions

To the best of our knowledge, this is the first study to compare path gain and signal fading on fixed NLOS links in suburban macrocell environments over the frequency range 220 MHz to 2 GHz. Our most significant finding is that the depth of signal fading drops off rapidly as frequency decreases (or as wavelength increases). A link that experiences severe fading at 1.9 GHz is often relatively unaffected at 220 MHz. An obvious next step for future researchers will be to develop a more sophisticated physical model that is consistent with the multiband measurement data presented here.

The first-order statistical models that we have presented here capture the essential aspects of the manner in which fixed wireless channels between 200 MHz and 2 GHz fade in a typical suburban macrocell environment. Development of models applicable to a broad range of environments would require additional measurement data: (1) from other sites, (2) from transmitters at different heights and (3) at additional frequencies within the range of interest. Such models will provide a basis for predicting the coverage and outage probabilities experienced by point-to-multipoint fixed wireless networks deployed in suburban macrocell environments and for assessing the suitability of a particular frequency band for use in a given application. The results presented here represent the first step in achieving this goal.

References

[1] W. Webb, "Broadband fixed wireless access as a key component of the future integrated communications environment," *IEEE Commun. Mag.,* vol. 39, no. 9, pp. 115-121, Sep. 2001.

[2] K. Lu, Y. Qian and H-H Chen, "Wireless broadband access: WIMAX and beyond," *IEEE Commun. Mag.*, vol. 45, no. 5, pp. 124-130, May 2007.

[3] S. S. Venkata, A. Pahwa, R. E. Brown, and R. D. Christie, "What future distribution engineers need to learn," *IEEE Trans. Power Syst.*, vol.19, no.1, pp. 17-23, Feb. 2004.

[4] G. Simard and D. Chartrand, "Hydro-Quebec's Economic and Technical Approach to Justify its Distribution Automation Program," in *Proc. IEEE PES'07,* pp. 1-5, 24-28 Jun. 2007.

[5] S. Jim, W. Carr, and S. E. Collier, "Real time distribution analysis for electric utilities," in *Proc. IEEE REPC'08,* pp. B5-B5-8, 27-29 Apr. 2008.

[6] D. G. Michelson, V. Erceg, and L. J. Greenstein, "Modeling diversity reception over narrowband fixed wireless channels," in *Proc. IEEE MTT-TWA'99*, pp. 95-100, 21-24 Feb. 1999.

[7] L. J. Greenstein, S. S. Ghassemzadeh, V. Erceg and D. G. Michelson, "Ricean K-factors in narrowband fixed wireless channels: Theory, experiments and statistical models," in *Proc. WPMC'99*, 21-23 Sep. 1999.

[8] S. Perras and L. Bouchard, "Fading characteristics of RF signals due to foliage in frequency bands from 2 to 60 GHz," in *Proc. WPMC'02*, 27-30 Oct. 2002, pp. 267-271.

[9] M. J. Gans, N. Amitay, Y. S. Yeh, T. C. Damen, R. A. Valenzuela, C. Cheon and J. Lee, "Propagation measurements for fixed wireless loops (FWL) in a suburban region with foliage and terrain blockages," *IEEE Trans. Wireless Commun.*, vol. 1, no. 2, pp. 302-310, Apr. 2002.

[10] E. R. Pelet, J. E. Salt, and G. Wells, "Effect of wind on foliage obstructed line-of-sight channel at 2.5 GHz," *IEEE Trans. Broadcasting*, vol. 50, no. 3, pp. 224-232, 2004.

[11] D. Crosby, V. S. Abhayawardhana, I. J. Wassell, M. G. Brown, and M. P. Sellars, "Time variability of the foliated fixed wireless access channel at 3.5 GHz," in *Proc. IEEE VTC 2005 Spring*, 25-28 Sep. 2005, pp. 106-110.

[12] R. Feick, R. A. Valenzuela and L. Ahumada, "Experiment results on the level crossing rate and average fade duration for urban fixed wireless channels," *IEEE Trans. Commun.,* vol. 9, no. 1, pp. 175-179, Jan. 2007.

[13] H. Suzuki, C. D. Wilson, and K. Ziri-Castro, "Time variation characteristics of wireless broadband channel in urban area," presented at *EuCAP'06*, Nice, France, 2-6 Nov. 2006.

[14] "Policy for the Use of 700 MHz Systems for Public Safety Applications and Other Limited Use of Broadcasting Spectrum," Industry Canada Radio Systems Policy, RP-006 – Issue 1, Jun. 2006.

[15] "Proposals and Changes to the Spectrum in Certain Bands below 1.7 GHz," Industry Canada Gazette Notice DGTP-004-05, Dec. 2005.

[16] M. Hata, "Empirical formula for propagation loss in land mobile radio services," *IEEE Trans. Veh. Technol.,* vol. 29, no. 3, pp. 317-325, Aug. 1980.

[17] E. Damosso, Ed., "Digital Mobile Radio Toward Future Generation Systems - Final Report," COST 231 Final Report, 1996.

[18] V. Erceg, L. J. Greenstein, S. Y. Tjandra, S.R. Parkoff, A. Gupta, B. Kulic, A. A. Julius, and R. Bianchi, "An empirically based path loss model for wireless channels in suburban environments," *IEEE J. Sel. Areas Commun.,* vol. 17, no. 7, pp. 1205-1211, July 1999.

[19] Y. H. Lee and Y. S. Meng, "Tropical weather effects on foliage propagation," in *Proc. EuCAP '07,* 11-16 Nov. 2007, pp. 1-5.

[20] L. J. Greenstein, D. G. Michelson, and V. Erceg, "Moment-method estimation of the Ricean K-factor," *IEEE Commun. Lett,* vol. 3, no. 6, pp. 175-176, Jun. 1999.

[21] D. S. Baum, D. A. Gore, R. U. Nabar, S. Panchanathan, K. V. S. Hari, V. Erceg and A. J. Paulraj, "Measurements and characterization of broadband MIMO fixed wireless channels at 2.5 GHz," in *Proc. IEEE ICPWD'00,* 17-20 Dec. 2000, pp. 203-206.

[22] S. R. Hanna and J. C. Chang, "Representativeness of wind measurements on a mesoscale grid with station separations of 312 m to 10 km," *Boundary-Layer Meteorol,* vol. 60, pp. 309-324, 1992.

[23] D. A. J. Pearce, A. G. Burr and T. C. Tozer, "Modelling and predicting the fading performance of fixed radio links through vegetation," in *Proc. IEE NCAP'99,* 31 Mar.-1 Apr. 1999, pp. 263-266.

[24] P. Lédl, P. Pechač and M. Mazánek, "Time-series prediction of attenuation caused by trees for fixed wireless access systems operating in millimeter waveband," in *Proc. IEE ICAP'03,* 31 Mar.-3 Apr. 2003, pp. 646-649.

[25] M. Cheffena and T. Ekman, "Modeling the dynamic effects of vegetation on radiowave propagation," in *Proc. IEEE ICC'08*, 19-23 May 2008, pp. 4466-4471.

3 Characterization of Time Variation on 1.9 GHz Fixed Wireless Channels in Suburban Macrocell Environments[2]

3.1 Introduction

A growing number of fixed wireless point-to-multipoint communication systems that are deployed in suburban environments operate in the frequency range from 800 MHz to 6 GHz. It has long been recognized that wind blowing through foliage is a major cause of deep fading on the links in such systems. Together, the depth and rate of fading have significant implications for both: (1) the implementation and tuning of automatic gain control and automatic power control loops [1], and (2) for schemes such as opportunistic scheduling that take advantage of fast time fluctuations in the radio channel to improve system performance by favoring users at a time when they have higher data rates [2]. If the signal fluctuations occur too slowly, the performance of the opportunistic scheduler will be impaired and mitigation strategies must be devised, e.g., [3]. The tendency for the Ricean K-factor to decrease as wind speed and/or distance increases has been noted and models that relate K to the two parameters in various environments have been proposed [4]-[10]. However, with the exception of a few anecdotal results, relatively little has been done to characterize the manner in which average wind speed and the distance of the terminal from the base station affect the *rate* of fading [11].

The rate at which signal fading occurs may be characterized either by the Level Crossing Rate (LCR) and Average Fade Duration (AFD) at selected thresholds above and below the mean signal strength [12] (which depend on both the first- and second-order statistics of the fading signal) or by a Doppler power spectrum [13],[14] (which depends only upon the second-order statistics). Although the latter representation is particularly useful because it is a key input for algorithms used to simulate (or emulate) fading channels, *e.g.*, [15],[16], estimation of the Doppler power spectrum from measured data generally requires coherent time series data (amplitude and phase). Fading on fixed wireless links occurs so slowly, however, that lack of phase coherence between the local oscillators in the widely separated transmitter and receiver can severely distort the result. Although a method for estimating the Doppler spectrum from

[2] A ver sion of this chapter has been submitted for publication: A. Liou, K.N. Sivertsen, and D.G. Michelson, "Characterization of Time Variation on 1.9 GHz Fixed Wireless Channels in Suburban Macrocell Environments."

amplitude-only measurement data was proposed in [14], it is intended mainly for use on short-range line-of-sight paths where the Ricean K-factor is high, *e.g.*, $K > 10$, and is much less effective in suburban macrocell environments where K is often < 10.

In certain cases, it has been found that one can fit the measured level crossing rate (LCR) and/or average fade duration (AFD) distributions seen on fixed wireless links to expressions that are normally justified only for mobile wireless links [12]. This allows one to express the time variation on the link in terms of just three parameters: the mean signal strength, the Ricean K-factor, and an equivalent Doppler frequency which is referred to as $f_{d,FW}$ in [12] and which we will simply refer to as f_d. Here, based upon short-term measurements collected at 107 different locations in a suburban macrocell environment characterized by flat terrain and heavy foliage, we present what we believe is the first effort to describe the manner in which both K and f_d on 1.9 GHz fixed wireless links vary with both distance and average wind speed across a typical suburban macrocell. We have also showed how changing the shape of the Doppler spectrum affects the relationship between the estimated parameter f_d and the corresponding maximum Doppler frequency $f_{d,\max}$.

The remainder of this paper is organized as follows: In Section 3.2, we consider the model and method for estimating f_d that was proposed in [12] in greater detail. In Section 3.3, we describe the measurement setup that we used to collect our data. In Section 3.4, we describe how we reduced the data and present our results. In Section 3.5, we summarize our contributions and their implications.

3.2 The Model

If the complex envelope of the time-varying path gain, $g(t)$, experienced by either a mobile or fixed links is given by the sum of a fixed component V and a zero-mean complex Gaussian process $v(t)$ and $r(t) = |g(t)|^2$, the first-order statistics of r will follow a Ricean distribution where

$$p(r) = \frac{2(K+1)r}{\Omega}\exp\left(-K - \frac{(K+1)r^2}{\Omega}\right)\cdot I_0\left(2\sqrt{\frac{K(K+1)}{\Omega}}r\right), \tag{3.1}$$

Ω is the average envelope power and $I_0(\cdot)$ is the zero order modified Bessel function of the first kind. In such cases, the Ricean K-factor is given by

$$K = |V|^2 / \overline{|v(t)|^2} = |V|^2 / \sigma^2 , \tag{3.2}$$

where σ^2 is the power in the time-varying component. Various methods for estimating K have been proposed. Here, we use the moment-based method described in [17] where

$$K = \frac{|V|^2}{\sigma^2} = \frac{\sqrt{G^2 - \sigma_G^2}}{G - \sqrt{G^2 - \sigma_G^2}}, \tag{3.3}$$

and σ_G is the rms fluctuation of the envelope about the mean which is given by the standard deviation of $|g(t)|^2$.

In cases where the base station is fixed, the terminal is in motion, and scattering is two-dimensional and isotropic, the Doppler spectrum of the time-varying component is given by Clarke's U-shaped spectrum and ranges between range from $-f_{d,max}$ to $f_{d,,max}$. The frequency offset of the carrier that corresponds to the fixed component is determined by the direction of the propagation path relative to the velocity of the terminal. In such cases, the LCR and AFD are given by

$$LCR = \sqrt{2\pi(K+1)} f_d \rho \exp\left(-K-(K+1)\rho^2\right) \cdot I_0\left(2\sqrt{K(K+1)}\rho\right) \tag{3.4}$$

And

$$AFD = \frac{\left(1 - Q\left(\sqrt{2K}, \sqrt{2(K+1)\rho^2}\right)\right) \exp\left(K + (K+1)\rho^2\right)}{\sqrt{2\pi(K+1)} f_d \rho I_0(2\sqrt{K(K+1)}\rho)} \tag{3.5}$$

where T is the threshold voltage, $\rho = T/r_{rms}$ is the threshold normalized to the rms envelope, Q($\cdot$) is the Marcum-Q function and, in this case, f_d corresponds to $f_{d,,max}$.

In cases where both the base station and the terminal are fixed, time variation is due entirely to the motion of scatterers in the environment and the corresponding Doppler spectrum generally exhibits a sharp peak at the carrier frequency and rapidly decays as the frequency offset increases, e.g., [13]. In [12], it was shown that under certain conditions the expressions for LCR and AFD given in (3.4) and (3.5) do not depend on the shape of the Doppler spectrum. In particular, applying the value of K estimated using (3.3) or similar to (3.4) and (3.5), and choosing an appropriate value for f_d will often provide a good approximation to the LCR and AFD characteristics observed on fixed wireless links. Further, it was reported that a good estimate of f_d can be obtained by considering only the Zero Crossing Rate, ZCR, which is defined as the value of LCR for $\rho = 1$, i.e.,

$$\mathrm{ZCR} = \sqrt{2\pi(K+1)}f_d \exp\left(-2K-1\right)\cdot I_0\left(2\sqrt{K(K+1)}\right). \tag{3.6}$$

For $K > 3$, this expression is virtually insensitive to the actual value of K, yielding the convenient approximation

$$f_d \approx 1.4\,\mathrm{ZCR}\,. \tag{3.7}$$

3.3 The Measurement Setup

3.3.1 CW Channel Sounder

Our CW channel sounder consists of a 1.9 GHz CW transmitter that we carried aboard our drive test vehicle and a dual-channel narrowband measurement receiver that we installed at our base station. A block diagram of the measurement setup is presented in Figure 3.1. We used a Marconi 2031 RF signal generator and an RF power amplifier to bring the transmitted power level up to 6 Watts, and a Bird digital RF power meter to measure the precise value. We used a 1.9 GHz vertically polarized omnidirectional sleeve dipole antenna with a gain of 2.2 dBi as our transmitting antenna. When used in non-line-of-sight configurations, fixed wireless antennas are typically mounted at heights between 0.5 m (*e.g.,* for nomadic applications) and 4 m (*e.g.,* for permanent installations). As a compromise, we mounted the antenna on the center of the roof of our drive test vehicle at a height of 1.75 m.

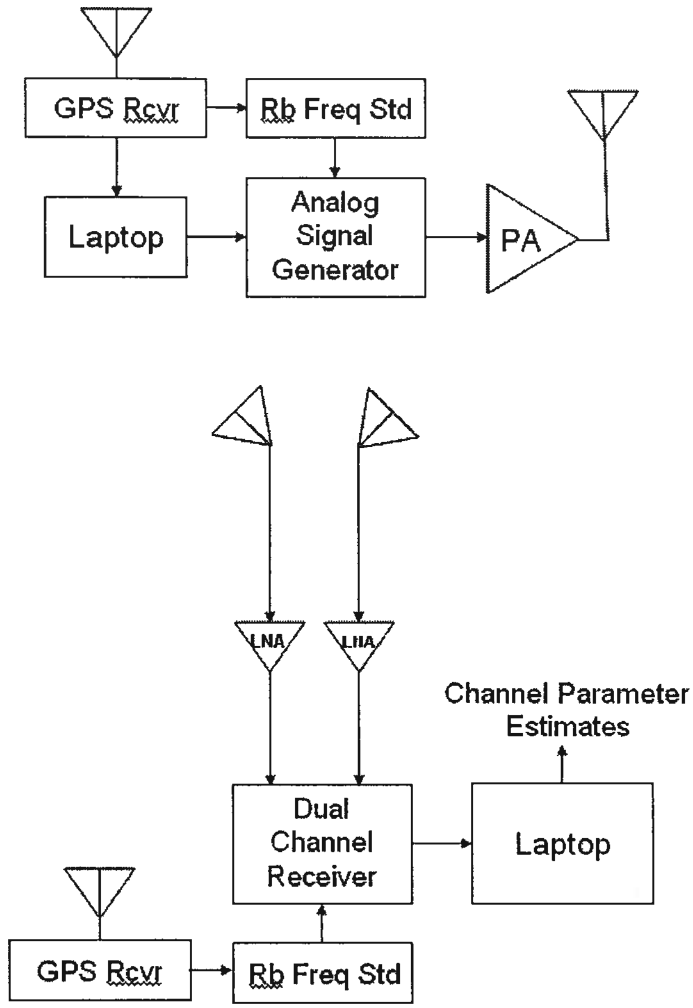

Figure 3.1 – Dual channel sounder system set up.

We used a Cushcraft 1.9 GHz forward and back slant polarization diversity antenna with a gain of 7 dBi and beamwidth of 60 degrees as our receiving antenna. We mounted the antenna, mast and rotator atop a tower at a height of 25 m above ground level. When the drive test vehicle moved to a new location within the survey area, the receiving site operator rotated the antenna boresight towards it. We boosted the signals received on each branch by 25 dB using a pair of Mini-Circuit low noise amplifiers before we applied the signals to an HP 8753E vector network analyzer configured to operate as a dual-channel tuned receiver with an IF bandwidth of 30 Hz. We stabilized the frequencies of both the transmitter and receiver using Stanford Research

Systems Rubidium frequency standards. Although outdoor temperatures were moderate during the measurement campaign, care was taken to protect the Rubidium frequency standard from sudden changes in ambient temperature, e.g., as might be caused by sudden drafts of air.

Once per minute, we recorded the average wind speed estimated by a Davis Vantage Pro2 wireless weather station that we installed on a second tower located near the receiving site. Because previous work has shown that variations in average wind speed at tree top level or above are well correlated over mesoscale distances of several kilometers [18], we considered one wind measurement location near the base station to be adequate.

3.3.2 Calibration and Verification Protocol

Before we collected any field data, we verified the function and operation of our CW channel sounder using a Spirent SR5500 channel emulator that we configured in dual channel mode. We set the path gain and Ricean K-factor to a range of values. In each case, we confirmed that we were able to correctly estimate each parameter. We also selected alternative Doppler spectrum shapes, set the maximum Doppler frequency to a range of values and estimated the equivalent Doppler frequency using the method described in Section 3.2. The results are presented in Section 3.4.

3.3.3 Test Area

Our test area consisted of neighborhoods in and around the University of British Columbia and the surrounding University Endowment Lands. Within an annulus between 500 and 1500 m from our receiving site, we had access to both: (1) residential neighbourhoods with tall trees and heavy foliage throughout and (2) light urban areas with two- and four-storey buildings and somewhat less foliage. Almost all of the motion in the environment arose from wind-blown foliage; few, if any, cars, people or other moving scatterers were present in the vicinity when we collected measurement data. Most of the foliage in the area is coniferous but at least one-third is deciduous. Because the duration of the measurement campaign was only six weeks, we had no opportunity to observe the effects of seasonal variations in the foliage, i.e., with trees in and out of leaf [19]. All of our data was collected with the trees in leaf.

3.3.4 Data Collection Protocol

Over a span of several weeks, the operator drove the drive test vehicle to each of the 100 survey locations that we had selected in advance and parked for approximately 20 minutes at each one. Once the transmitter was operating, the operator at the receiving site pointed the receiving antenna in the direction of the survey location, then began recording time series measurements of the amplitude of the signals (in dBm) received on the two diversity branches. The measured data were collected in the form of eight successive 120-second sweeps. Each of the eight sweeps contains 1601 samples collected at 0.075 second intervals or at a sample rate of 13.3 Hz. Collecting data at 107 locations over a range of wind conditions took approximately six weeks.

3.4 Results

3.4.1 Effect of Spectrum Shape on the Equivalent Doppler Frequency

If the remote terminal is in motion and scattering is two-dimensional and isotropic, the Doppler spectrum of the fading signal follows Clarke's model and f_d in (3.4) and (3.5) is given by

$$f_d = k\, f_{d,\max}, \tag{3.8}$$

where $k = 1$. If the scattering is non-isotropic and/or the terminal is not in motion, the shape of the Doppler spectrum will be quite different. During the calibration and validation protocol described in Section 3.3.3, we determined the value of k that applies to various Doppler spectrum shapes. We found that as the fraction of energy in the high frequency portion of the spectrum decreases, so does k. In particular, the 6-dB classic, flat and rounded spectra described in [20] yielded $k = 0.91$, 0.74 and 0.58, respectively. Further work is required to determine the corresponding relationship for spectra more typical of fixed wireless environments, e.g., [13].

3.4.2 Dependence of the Ricean K-factor and Equivalent Doppler Frequency on Averaged Wind Speed

The average wind speed $\overline{v}_w$ observed at the base station observed during the short-term measurements followed a normal distribution with a mean value of 8.7 km/h and a standard deviation of 3.4 km/h. (When we claim or imply that a parameter or residual follows a normal distribution, we mean that it passed the Anderson-Darling test at the 5% significance level [21].) The manner in which the Ricean K-factor in dB decreased with the average wind speed across all measurement locations is presented in Figure 3.2(a). We applied regression analysis to determine that the relationship between Ricean K-factor and average wind speed at this site can be modeled by

$$K(\text{dB}) = -0.63\overline{v}_w + 8.27 + K_\sigma \tag{3.9}$$

where K_σ is a zero mean Gaussian random variable with standard deviation of 5.1 dB and the correlation coefficient ρ = -0.38.

The manner in which the equivalent Doppler frequency, f_d, in dBHz varied with the average wind speed is presented in Figure 3.2(b). As was observed in [11] at a handful of locations, the fading rate is essentially independent of wind speed. We applied regression analysis to determine that the relationship between equivalent Doppler frequency and average wind speed at this site can be modeled by

$$f_d(\text{dBHz}) = 0.005\overline{v}_w - 0.096 + f_\sigma \tag{3.10}$$

where f_σ is a zero mean Gaussian random variable with standard deviation of 1.97 dBHz and the correlation coefficient ρ = 0.009. In practice, it seems reasonable to simply drop the term in $\overline{v}_w$.

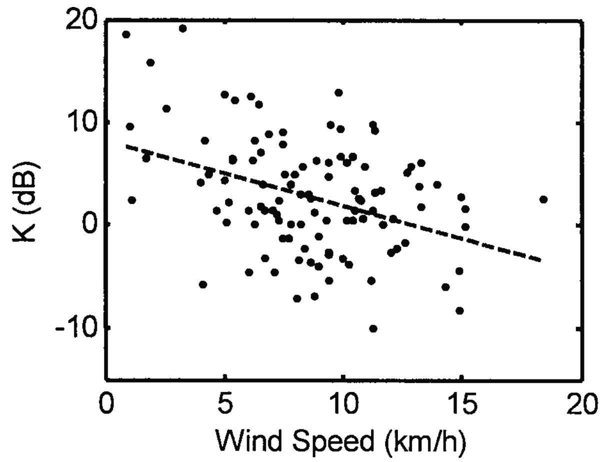

(a)

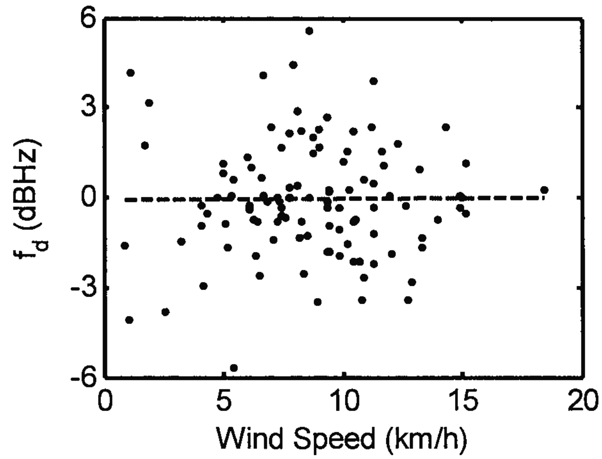

(b)

Figure 3.2 – (a) K-factor vs. distance and (b) equivalent Doppler frequency vs. average wind speed as observed at 107 locations across the test site.

3.4.2 Dependence of the Ricean K-factor and Equivalent Doppler Frequency on Distance

Our transmitter locations were situated between 500 and 1500 m away from the base station. The manner in which the Ricean K-factor in dB decreased with distance across all measurement locations is presented in Figure 3.3(a). We applied regression analysis to determine that the relationship between Ricean K-factor and distance at this site can be modeled by

$$K(\text{dB}) = -1.61(10\log_{10} d) + 1.92 + K_{\sigma} \tag{3.11}$$

where d is the distance in km, K_σ is a zero mean Gaussian random variable with standard deviation of 5.25 dB and the correlation coefficient ρ = -0.33.

The tendency for the equivalent Doppler frequency, f_d, in dBHz to rapidly increase with distance, as seen in Figure 3.3(b), was unexpected. We applied regression analysis to determine that the relationship between the equivalent Doppler frequency and distance at this site can be modeled by

$$f_d(\text{dBHz}) = 0.46(10\log_{10} d) + 0.38 + f_\sigma \tag{3.12}$$

where d is the distance in km, f_σ is a zero mean Gaussian random variable with standard deviation of 1.75 dBHz and the correlation coefficient ρ = 0.46.

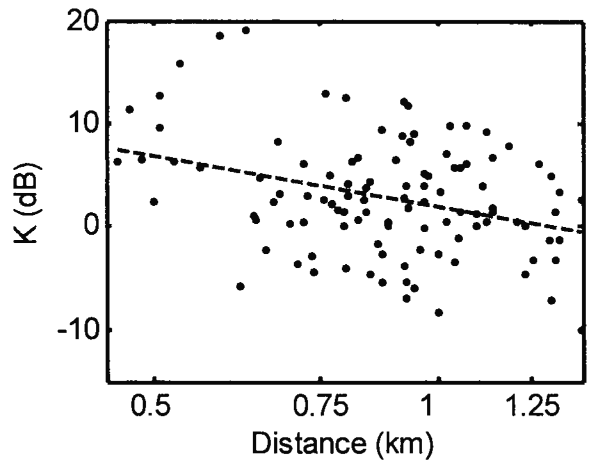

(a)

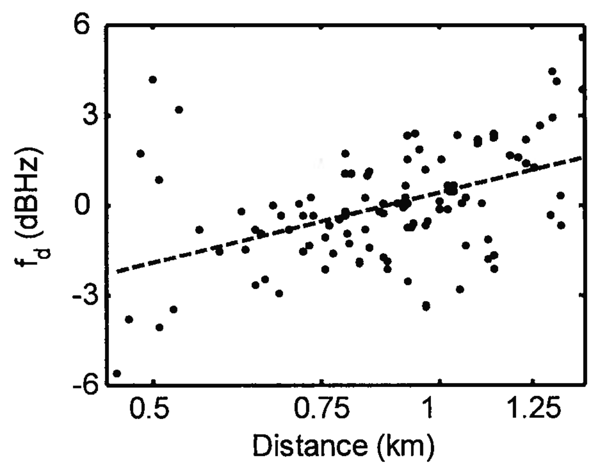

(b)

Figure 3.3 – (a) Ricean K-factor and (b) equivalent Doppler frequency, f_d, vs. distance as observed at 107 locations across the test site.

Because both K_σ and f_σ are Gaussian random variables, they can be cast as a bivariate distribution for the purposes of simulation. Their joint distribution is depicted in Figure 3.4 where the excess Ricean K-factor ΔK and the excess equivalent Doppler frequency Δf_d are the deviations about the regression lines given in (3.11) and (3.12) that are captured by K_σ and f_σ. The parameters of the marginal distribution are as given above. With a correlation coefficient of -0.117, the two random variables are effectively uncorrelated.

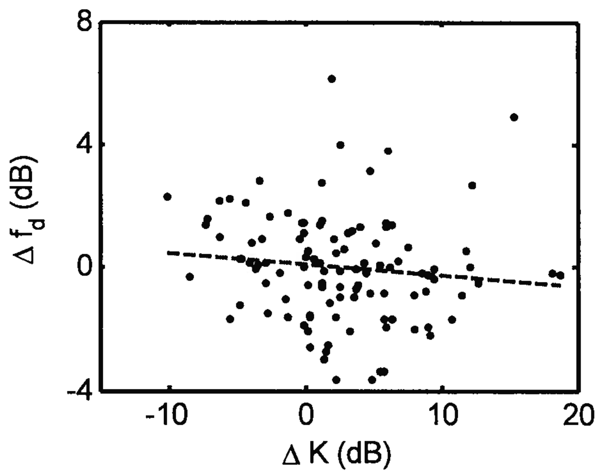

Figure 3.4 – The excess Ricean K-factor, ΔK, vs. the excess equivalent Doppler frequency, Δf_d, as observed at 107 locations across the test site.

3.5 Discussion

As has been observed at other macrocell sites, the Ricean K-factor decreased with both average wind speed and distance. Our observation that the equivalent Doppler frequency was effectively uncorrelated with wind speed corroborates anecdotal results reported in [11]. Our observation that equivalent Doppler frequency noticeably increased with distance was unexpected. Similar measurements should be collected at other sites in order to determine the extent to which this trend is affected by foliage density and tower height or might be predicted by suitably modified physical models of wind blown foliage, perhaps similar to those reported in [22] and [23].

References

[1] E. Armanious, D. D. Falconer, H. Yanikomeroglu, "Adaptive modulation, adaptive coding, and power control for fixed cellular broadband wireless systems: some new insights," in *Proc. IEEE WCNC'03*, 16-20 March 2003, pp. 238-242.

[2] X. Liu, E.K.P. Chong and N.B. Shroff, "Opportunistic transmission scheduling with resource-sharing constraints in wireless networks," *IEEE J. Sel. Areas Communic.,* vol. 19, no. 10, pp. 2053-2064, Oct. 2001.

[3] P. Viswanath, D.N.C. Tse and R. Laroia, "Opportunistic beamforming using dumb antennas," *IEEE Trans. Inform. Theory,* vol. 48, no. 6, pp. 1277-1294, Jun. 2002.

[4] L. J. Greenstein, S. S. Ghassemzadeh, V. Erceg and D. G. Michelson, "Ricean K-factors in narrowband fixed wireless channels: Theory, experiments and statistical models," in *Proc. WPMC'99* (Amsterdam, Netherlands), Sep. 1999.

[5] D. S. Baum et al., "Measurements and characterization of broadband MIMO fixed wireless channels at 2.5 GHz," in *Proc. ICPWC 2000*, Dec. 2000, pp. 203-206.

[6] V. Erceg et al. "Channel Models for Fixed Wireless Applications," IEEE 802.16a-03/01, 27 Jun 2003.

[7] S. Perras and L. Bouchard, "Fading characteristics of RF signals due to foliage in frequency bands from 2 to 60 GHz," in *Proc. IEEE WPMC 2002*, 2002.

[8] E. R. Pelet, J. E. Salt, and G. Wells, "Effect of wind on foliage obstructed line-of-sight channel at 2.5 GHz," *IEEE Trans. Broadcast.,* vol. 50, no. 3, pp. 224-232, 2004.

[9] D. Crosby, V. S. Abhayawardhana, I. J. Wassell, M. G. Brown, and M. P. Sellars, "Time variability of the foliated fixed wireless access channel at 3.5 GHz," in *Proc. IEEE VTC 2005 Spring*, pp.106-110, 2005.

[10] M. H. Hashim and S. Stavrou, "Wind influence on radio waves propagating through vegetation at 1.8 GHz," *IEEE Antennas Wireless Propag. Lett.* vol. 4, pp. 143-146, 2005.

[11] M. H. Hashim, D. Mavrakis and S. R. Saunders, "Measurement and analysis of temporal fading due to moving vegetation," in *Proc. ICAP 2003*, 31 Mar. – 3 Apr. 2003, pp. 650-653.

[12] R. Feick, R. A. Valenzuela, and L. Ahumada, "Experiment results on the level crossing rate and average fade duration for urban fixed wireless channels," *IEEE Trans. Communic.*, vol. 9, no. 1, pp. 175-179, Jan 2007.

[13] S. Thoen, L. V. D. Perre, and M. Engels, "Modeling the channel time-variance for fixed wireless communications," *IEEE Communic. Lett.*, vol. 6, no. 8, pp. 331-333, Aug. 2002.

[14] A. Domazetovic, L. J. Greenstein, N. B. Mandayam, and I. Seskar, "Estimating the Doppler spectrum of a short-ranged fixed wireless channel," *IEEE Communic. Lett.*, vol. 7, no. 5, pp. 227-229, May 2003.

[15] K. E. Baddour and N. C. Beaulieu, "Accurate simulation of multiple cross-correlated Rician fading channels," *IEEE Trans. Commun.* vol. 52, no. 11, pp. 1980-1987, Nov. 2004.

[16] B. Natarajan, C. R. Nassar and V. Chandrasekhar, "Generation of correlated Rayleigh fading envelopes for spread spectrum applications," *IEEE Communic. Lett.*, vol. 4, no. 1, pp. 9-11, Jan. 2000

[17] L. J. Greenstein, D.G. Michelson and V. Erceg, "Moment-method estimation of the Ricean K-Factor" *IEEE Commun. Lett.*, vol. 3, no. 6, pp. 175-176, Jun. 1999.

[18] S. R. Hanna and J. C. Chang, "Representativeness of wind measurements on a mesoscale grid with station separations of 312 m to 10 km," *Boundary-Layer Meteorol,* vol. 60, pp. 309-324, 1992.
[19] ITU, "Attenuation in Vegetation," Rec. ITU-R P.833-6, 2007.
[20] "SR5500 Wireless Channel Emulator Operations Manual," Spirent Communications, Eatontown, NJ, 2006, pp. 3-16.
[21] M. A. Stephens, "EDF statistics for goodness of fit and some comparisons," *J. Amer. Statistical Assoc.,* vol. 69, no. 347, pp. 730-737, Sep. 1974.
[22] D. A. J. Pearce, A. G. Burr and T. C. Tozer, "Modelling and predicting the fading performance of fixed radio links through vegetation," in *Proc. IEE NCAP'99,* 31 Mar.-1 Apr. 1999, pp. 263-266.
[23] P. Lédl, P. Pechač and M. Mazánek, "Time-series prediction of attenuation caused by trees for fixed wireless access systems operating in millimeter waveband," in *Proc. IEE ICAP'03*, 31 Mar.-3 Apr. 2003, pp. 646-649.

4 Depth and Rate of Fading on Fixed Wireless Channels between 200MHz and 2GHz in Suburban Macrocell Environments[3]

4.1 Introduction

In recent years, as: (1) common carriers seek methods for providing either fixed or nomadic network access services to residential households without the expense of deploying wireline connectivity over the last mile [1],[2] and (2) public utilities seek methods that will allow them to: (a) detect and report outages, (b) monitor usage, and (c) implement strategies that encourage customers to limit consumption and adopt sustainable practices ·[3]-[5], the possibility of deploying fixed wireless multipoint communication systems in suburban macrocell environments has attracted considerable interest. In order to provide developers with the insights required to design effective systems, several groups in Canada, the United States, the United Kingdom, Chile, Australia and elsewhere have conducted measurement campaigns which have aimed to characterize the depth of signal fading observed in such environments, *e.g.*, [6]-[12].

In macrocell environments, the base station antenna is mounted well above the local rooftop or treetop level and the remote terminal antenna is mounted below the local rooftop or treetop level. As a result, the wireless links are usually obstructed by intervening obstacles and a large fraction of the signal that reaches the receiver does so as a result of scattering and diffraction by objects in the environment. Because both the transmitting and receiving antennas in such applications are fixed, signal fading is caused solely by the motion of objects in the environment that scatter and diffract the signal. In suburban macrocell environments, a large fraction of those objects are trees and foliage with leaves and branches that sway when blown by the wind.

The vast majority of previous studies of fixed wireless channels in suburban macrocell environments focused on individual frequency bands at 1.9 GHz and above, including the PCS band at 1.9 GHz, the ISM band at 2.45 GHz, the Fixed Wireless

[3] A ver sion of this chapter has been submitted for publication: A. Liou, K.N. Sivertsen, and D.G. Michelson, "Rate of Fading on Fixed Wireless Channels between 200 MHz and 2 GHz in Suburban Macrocell Environments."

Access (FWA) band at 3.5 GHz and the U-NII and ISM bands at 5.2 and 5.8 GHz. However, spectrum regulators have recently begun to reallocate frequency bands below 2 GHz in order to help meet the requirements for broadband wireless access for urban and rural areas and/or narrowband telemetry for public utilities. In Canada, spectrum in frequency bands near 700 MHz has been proposed for fixed wireless broadband use in rural areas [14] and may find application in distribution automation by the electrical power industry. Frequency bands such as 220–222 MHz, 1429.5–1432 MHz and 1800–1830 MHz have recently been designated for utility telemetry and distribution automation [15]. Regulators are increasingly designating multiple primary allocations within individual frequency bands, as well as proposing more flexible licensing schemes, in an attempt to accommodate different users and services in the same spectrum. Both the amount of radio spectrum, and the choice of frequency bands available for fixed wireless use, will almost certainly increase in coming years.

The manner in which path loss, or its reciprocal, path gain, is affected by the carrier frequency, the heights of and separation between the base station and mobile terminal in suburban macrocell environments over the range from 200 MHz to 2 GHz has been well-studied over the years and has been captured by several standard models [16]-[18]. However, existing channel models do not provide a description of either the depth or rate of signal fading that fixed wireless channels will experience over this frequency range in suburban macrocell environments. Although previous efforts to characterize the fade dynamics of propagation through vegetation provided useful insights, the amount of data collected was limited [23]-[25].This lack of information places those charged with planning, simulating or deploying fixed wireless systems in suburban macrocell environments at a severe disadvantage when asked to predict the performance of data link protocols (including handshaking schemes) and opportunistic schedulers.

Because fading on fixed wireless channels in macrocell environments normally follows a Ricean distribution, the depth of fading is typically expressed in terms of the Ricean K-factor. The rate at which signal fading occurs may be characterized either by the Level Crossing Rate (LCR) and Average Fade Duration (AFD) at selected thresholds above and below the mean signal strength [12] (which depend on both the first- and second-order statistics of the fading signal) or by a Doppler power spectrum [21],[14] (which depends only upon the second-order statistics). Although the latter representation is particularly useful because it is a key input for algorithms used to simulate (or emulate) fading channels, *e.g.*, [15],[16], estimation of the Doppler power spectrum from measured data generally requires coherent time series data (amplitude and phase). Fading on fixed wireless links occurs so slowly, however, that lack of phase coherence between the local oscillators in the widely separated transmitter and receiver can severely distort the measurement. Although a method for estimating the Doppler spectrum from amplitude-only measurement data was proposed in [14], it is mainly intended for use on short-range line-of-sight paths where the Ricean K-factor is high, *e.g.*, $K > 10$, and is much less effective in suburban macrocell environments where K is often < 10.

In certain cases, it has been found that one can fit the measured level crossing rate (LCR) and/or average fade duration (AFD) distributions seen on fixed wireless links to expressions that are normally justified only for mobile wireless links [12]. This allows one to express the time variation on the link in terms of just three parameters: the mean signal strength, the Ricean K-factor, and an *effective maximum Doppler frequency* which is referred to as $f_{d,FW}$ in [12] and which we will simply refer to as f_d. Here, we take the first steps to determine how both the depth and rate of fading on fixed wireless channels in a typical suburban macrocell environment vary with carrier frequency, wind speed and distance across the frequency range from 200 MHz to 2 GHz. We established a transmitting site atop an eighteen-storey office tower located in the middle of a large suburban area. We simultaneously broadcast single carrier signals in the 220, 850 and 1900 MHz bands and collected time-series of the received signal strength observed in each band at fixed locations at ranges between 1 and 4 km. The frequencies that we employed bracket the majority of the bands that have been allocated to fixed wireless access and SCADA (supervisory control and data acquisition) applications. Although our results strictly apply to narrowband channels, they are also relevant to single carriers in multicarrier modulation schemes. The results presented here are specific to high transmitting sites; determining how lowering the base station height affects the results is a topic for future work.

The remainder of this paper is organized as follows: In Section 4.2, we summarize the essential aspects of our second-order model of fading on narrowband channels. In

Section III, we describe our measurement setup and test site. In Section IV, we present our results and suggest how these results can be used in system-level simulations. In Section V, we summarize our findings and contributions and discuss the implications of our results.

4.2 The Second-Order Fading Channel Model

If the complex envelope of the time-varying path gain, $g(t)$, experienced by either a mobile or fixed links is given by the sum of a fixed component V and a zero-mean complex Gaussian process $v(t)$ and $r(t) = |g(t)|$, the first-order statistics of r will follow a Ricean distribution where

$$p(r) = \frac{2(K+1)r}{G}\exp\left(-K - \frac{(K+1)r^2}{G}\right)\cdot I_0\left(2\sqrt{\frac{K(K+1)}{G}}r\right), \tag{4.1}$$

G is the average envelope power and $I_0(\cdot)$ is the zero order modified Bessel function of the first kind. In such cases, the Ricean K-factor is given by

$$K = |V|^2 / \overline{|v(t)|^2} = |V|^2/\sigma^2, \tag{4.2}$$

where σ^2 is the power in the time-varying component. Various methods for estimating K have been proposed. Here, we use the moment-based method described in [20] where

$$K = \frac{|V|^2}{\sigma^2} = \frac{\sqrt{G^2 - \sigma_G^2}}{G - \sqrt{G^2 - \sigma_G^2}}, \tag{4.3}$$

and σ_G is the rms fluctuation of the envelope about G, i.e., the standard deviation of $|g(t)|^2$.

In cases where the base station is fixed, the terminal is in motion, and scattering is two-dimensional and isotropic, the Doppler spectrum of the time-varying component is given by Clarke's U-shaped spectrum and ranges from $-f_{d,max}$ to $f_{d,,max}$. The frequency offset of the carrier that corresponds to the fixed component is determined by the direction of the propagation path relative to the velocity of the terminal. In such cases, the LCR and AFD are given by

$$LCR = \sqrt{2\pi(K+1)} f_d \rho \exp\left(-K-(K+1)\rho^2\right) \cdot I_0\left(2\sqrt{K(K+1)}\rho\right) \tag{4.4}$$

and

$$\begin{aligned} AFD &= \frac{\Pr(r<T)}{LCR} \\ &= \frac{\left(1-Q\left(\sqrt{2K},\sqrt{2(K+1)\rho^2}\right)\right)\exp\left(K+(K+1)\rho^2\right)}{\sqrt{2\pi(K+1)} f_d \rho I_0(2\sqrt{K(K+1)}\rho)} \end{aligned} \tag{4.5}$$

where T is the threshold voltage, $\rho = T/r_{rms}$ is the threshold normalized to the rms envelope, Q(·) is the Marcum-Q function and, in this case, f_d corresponds to $f_{d,,max}$ [12]

In cases where both the base station and the terminal are fixed, time variation is entirely due to the motion of scatterers in the environment and the corresponding Doppler spectrum generally exhibits a sharp peak at the carrier frequency and rapidly decays as the frequency offset increases, e.g., [21]. In [12], it was shown that under certain conditions the expressions for LCR and AFD given in (4.4) and (4.5) do not depend on the shape of the Doppler spectrum. In particular, applying the value of K estimated using (4.3) or similar to (4.4) and (4.5), and choosing an appropriate value for f_d will often provide a good approximation to the LCR and AFD characteristics observed on fixed wireless links. Further, it was reported that a good estimate of f_d can be obtained by considering only the Zero Crossing Rate, ZCR, which is defined as the value of LCR for $\rho = 1$, i.e.,

$$\text{ZCR} = \sqrt{2\pi(K+1)} f_d \exp\left(-2K-1\right) \cdot I_0\left(2\sqrt{K(K+1)}\right). \tag{4.6}$$

For $K > 3$, this expression is virtually insensitive to the actual value of K, yielding the convenient approximation

$$f_d \approx 1.4\,\text{ZCR}\,. \tag{4.7}$$

The significance of f_d is now unclear given that it no longer applies to the maximum frequency component of Clarke's U-shaped spectrum. In Section IV-B, we recount a possible interpretation of the physical significance of f_d. In the sections that follow, we describe our efforts to characterize the depth and rate of fading experienced over fixed wireless links across a broad frequency range from 200 MHz to 2 GHz in a typical suburban macrocell environment.

4.3 The Measurement Setup

4.3.1 Tri-band Channel Sounder

Our tri-band channel sounder consists of three continuous wave (CW) transmitters and three corresponding receivers that operate in the 220, 850 and 1900 MHz frequency bands. A block diagram of the CW transmitter is shown in Figure 4.1(a). The signal source portion of the transmitter contains a pair of Marconi 2022 RF signal generators, each of which is capable of supplying a CW signal up to 6 dBm over the range 10 kHz to 1 GHz, and a Marconi 2031 RF signal generator capable of supplying a CW signal up to 13 dBm over the range 10 kHz to 2.7 GHz. The signal generators are locked to a 10 MHz reference signal supplied by a Stanford Research Systems PRS10 Rubidium frequency standard. It, in turn, is disciplined by the 1 PPS signal supplied by a Trimble Resolution-T GPS receiver that has been designed for such applications.

The amplifier portion contains three power amplifiers: (1) a TPL Communications LMS series RF power amplifier capable of delivering between 20 and 100 W at 220 MHz, (2) a Unity Wireless Dragon RF power amplifier capable of delivering up to 30 W between 869 and 894 MHz and (3) a Unity Wireless Grizzly RF power amplifier capable of delivering up to 35 W between 1930 and 1990 MHz. During data collection, all three amplifiers were configured to deliver 20 W signals to their respective feedlines. A wireless remote control device that operates near 150 MHz allowed the data collection team to remotely enable or disable the power amplifiers at the start or end of a measurement session. The 220, 850 and 1900 MHz transmitting antennas are omnidirectional and have gains of 8.1, 6.1 and 5.0 dBi, respectively. They were installed atop the eighteen-storey office tower at BC Hydro's Edmonds facility in Burnaby, BC at a height of 80 m above ground level. The remaining parameters used in the system link budget for each band are given in Table 4.1.

Table 4.1 – Link Budget Parameters for the Tri-band Channel Sounder.

Parameter	220 MHz	850 MHz	1900 MHz
Transmitted Power	43 dBm	43 dBm	43 dBm
Transmit Cable Loss	1.3 dB	2.7 dB	4.3 dB
Transmit Antenna Gain	8.1 dBi	6.1 dBi	5 dBi
Receive Antenna Gain	1 dBi	1 dBi	1 dBi
Receive Cable Loss	0.37 dB	0.76 dB	1.2 dB
Receiver LNA Gain	-	30 dB	26 dB

A block diagram of our multiband receiver is shown in Figure 4.1(b). The receiving antennas are omnidirectional and all have the same nominal gain of 1 dBi. When used in NLOS configurations, fixed wireless antennas are typically mounted at heights between 0.5 m (*e.g.,* for nomadic applications) and 4 m (*e.g.,* for permanent installations). As a compromise, we mounted the antennas on the roof of our propagation measurement van at a height of 2.3 m. In many fixed wireless deployments, the terminal antennas are directional. Because our primary objective is to compare the behaviour of the channel at different frequencies, we elected to simplify the data collection protocol by collecting the measurement data using omnidirectional antennas. If the remote terminal antenna's beamwidth decreased or its height is increased, the path gain and/or the Ricean K-factor will tend to increase [7].

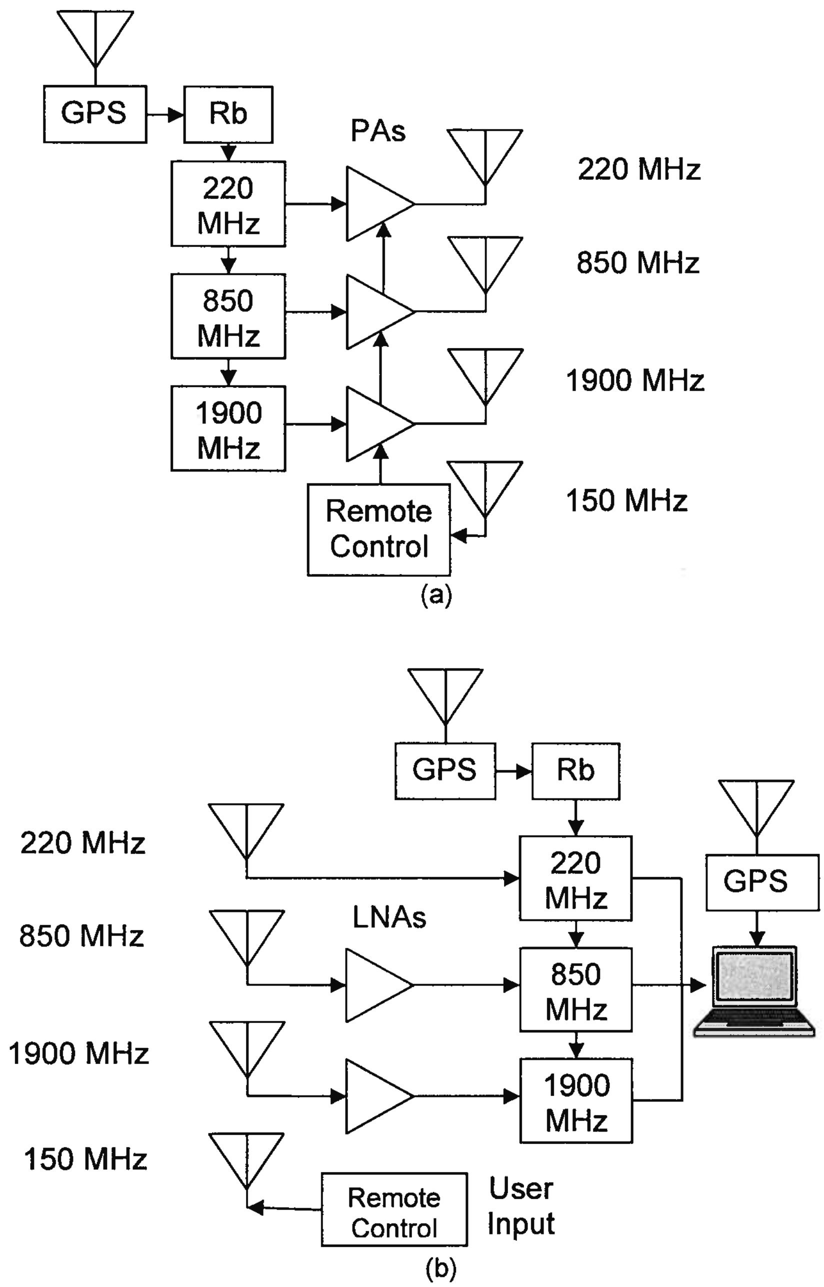

Figure 4.1 – (a) The tri-band transmitter that was deployed at the base station and (b) the tri-band receiver that was carried aboard the propagation measurement van.

The multiband receiver consists of: (1) a pair of Anritsu MS2651B spectrum analyzers that operate over the range from 9 kHz to 3 GHz with a selectable IF bandwidth, (2) an Anritsu MS2721A spectrum analyzer that operates over the range from 100 kHz to 7.1 GHz with a selectable IF bandwidth, (3) a Stanford Research Systems PRS10 Rubidium frequency standard that generates a 10 MHz reference signal to which the spectrum analyzers can be locked and (4) a Trimble Resolution-T GPS receiver that supplies the 1 PPS signal used to discipline the frequency standard. External low-noise pre-amplifiers with 30 dB and 26 dB gain were used to increase the sensitivity of the spectrum analyzers that measure the received strength of the 850 and 1900 MHz signals, respectively. We used a laptop computer equipped with a GPIB adapter to: (1) configure the spectrum analyzers and (2) collect data from them. We geocoded the data with a nominal circular error probability (CEP) of less than 5 metres using location information supplied by a u-blox Antaris 4 SuperSense GPS receiver.

4.3.2 Verification Protocol

Before we collected any field data, we verified the function and operation of our tri-band CW channel sounder using a Spirent SR5500 channel emulator. We set the relevant narrowband channel parameters, including path gain and Ricean K-factor, to various values over a broad range and, in each case, confirmed that we were able to correctly estimate each of the parameters. We verified the transmitted power levels using a Bird Model 5000EX digital wattmeter.

4.3.3 Weather Instrument

We measured the wind speed, wind direction, rain rate and outdoor temperature using a Davis Vantage Pro 2 wireless weather station that we mounted on a mast located about 30 metres away from the transmitting antennas. Internally, the weather station samples the relevant weather parameters every few seconds. Once per minute, it logs the average values of these parameters over the previous minute to an internal database. We used a custom software tool to match the received signal strength time series collected at a given location to the relevant weather data. Because previous work has shown that variations in average wind speed at tree top level or above are well correlated over mesoscale distances of several kilometers [22], we concluded that collecting wind data at a single location near the base station would be adequate for our purposes.

4.3.4 Test Area

Our test area consisted of suburban neighbourhoods with generally flat terrain, light to moderate foliage and one- and two-storey houses. We collected measurement data at 92 fixed measurement locations that were situated within an annular sector between 1 and 4 km from the transmitter site. Almost all the motion in the environment arose from windblown foliage; few, if any, cars, people or other moving scatterers were in the vicinity of the receiver when we collected measurement data. Most of the foliage in the area is deciduous and between 4 and 7 m in height but at least one-third is coniferous and up to 15 m in height. The duration of the measurement campaign was too short to permit observation of the effects of seasonal variations in the foliage. All of our data was collected with leaves on the trees.

4.3.5 Data Collection Protocol

Our data collection protocol comprised the following steps. First, we conducted a rapid survey of the proposed measurement locations in order to ensure that the strength of the received signal would be adequate at all locations. Next, over a span of several days, the operator drove the propagation measurement van to each of the fixed measurement locations that we had selected in advance. At each location, the operator collected simultaneous time series of the received strength of the 220, 850 and 1900 MHz CW signals. The measured data were collected in the form of fifteen successive 24-second sweeps. For the two higher bands, the pair of Anritsu MS2651B spectrum analyzers were used to record fifteen sweeps of 501 samples each, yielding 7515 received signal strength samples at each location and a sampling rate of 20.9 samples/sec. For the 220 MHz band, the Anritsu MS2721A spectrum analyzer was used; it yielded 551 samples per sweep or 8265 samples at each location and a sampling rate of 23.0 samples/sec. The sampling rates were chosen to be far greater than the anecdotal estimates of the maximum observed Doppler frequency reported previously, e.g., [21],[29]. As reported in the next section, our estimates of the effective maximum Doppler frequency, which is always less than the maximum observed Doppler frequency, were all significantly lower than 10 Hz.

4.4 Results

4.4.1 Estimation of the Equivalent Doppler Frequency

We processed the time series data that we collected at 92 locations as follows: First, we estimated K using (4.3) and the zero-crossing rate ZCR, which is defined as the value of LCR for $\rho = 1$. This corresponds to the case where the threshold is equal to the mean value of the fading envelope. If $K > 3$, we estimated the effective maximum Doppler frequency f_d using (4.7). Otherwise, we estimated f_d using (4.6). We assessed the accuracy of the results by substituting our estimates of K and f_d into (4.4) and (4.5) to yield the theoretical LCR and AFD distributions, respectively, and then superimposing them on the corresponding LCR and AFD distributions obtained by directly processing the time series. This allowed us to determine how transient signal fading, transient signal enhancement and non-stationary channel behaviour affect the performance of the estimator, an issue not considered in [12].

An example where the theoretical and experimental AFD and LCR distributions are a close match is given in Figure 4.2. Reduction of time series data collected in the 850 MHz band at a distance of 1555 m from the base station yielded $K = 7.9$ dB and $f_d = 0.47$ Hz. Inspection of the time series suggests that both the depth and rate of fading is consistent across the 6-minute duration of the observation. We conclude that the model given by (4.4) applies. A counterexample where the theoretical and experimental AFD and LCR curves do not match particularly well is given in Figure 4.3. Reduction of time series collected in the 220 MHz band at a distance of 3170 m yielded $K = 33$ dB and $f_d = 1.30$ Hz. However, inspection of the time series reveals that the depth and rate of fading are not consistent across the duration of the observation. Instead, the signal is virtually flat for the first 100 seconds (with the exception of a brief fade and enhancement at $t = 80$ seconds) then begins to experience rapid and consistent scintillation during the remainder of the observation. We interpret this as a transition between two channel states.

We produced plots of individual time series and the corresponding AFD and LCR distributions similar to those presented in Figure 4.2 and Figure 4.3 for all of our measurement locations. We used these results to identify deviations from stationary Ricean fading and to assess the goodness of fit between the theoretical and experimental AFD and LCR curves. The results are summarized in Table 4.2. In the vast majority of cases (69% at 220 MHz, 75% at 850 MHz, and 85% at 1900 MHz), the depth and rate of fading in the time series were consistent depth and rate of fading in the time series were consistent across the duration of the observation and the theoretical and experimental curves matched well. Transient signal enhancement, possibly due to reflections from passing vehicles, was the most common impairment. Slow fading superimposed upon an otherwise consistent fading signal was the next most common impairment. It tended to occur more often when the channel experienced high values of K. This suggests that the slow fading was the direct result of fading of the fixed component of the signal. In both cases, the experimental AFD curves were far more affected by fading and enhancement of the signal and deviated far more from their theoretical counterparts than did the experimental LCR curves. Between 4 and 9% of the time series in each band displayed either single or multiple transitions between channel states. In such cases, even the experimental LCR curves tended to deviate significantly from their theoretical counterparts. Because the parameters estimated from such time series would not be meaningful, we did not process them further.

Table 4.2 – Data Quality Summary in Percentages

Impairment	220 MHz	850 MHz	1900 MHz
None	69%	75%	85%
Slow Fades	9%	7%	10%
Transient Peaks	16%	9%	1%
Non-Stationary Fading	3%	3%	3%
Transition between States	3%	6%	1%

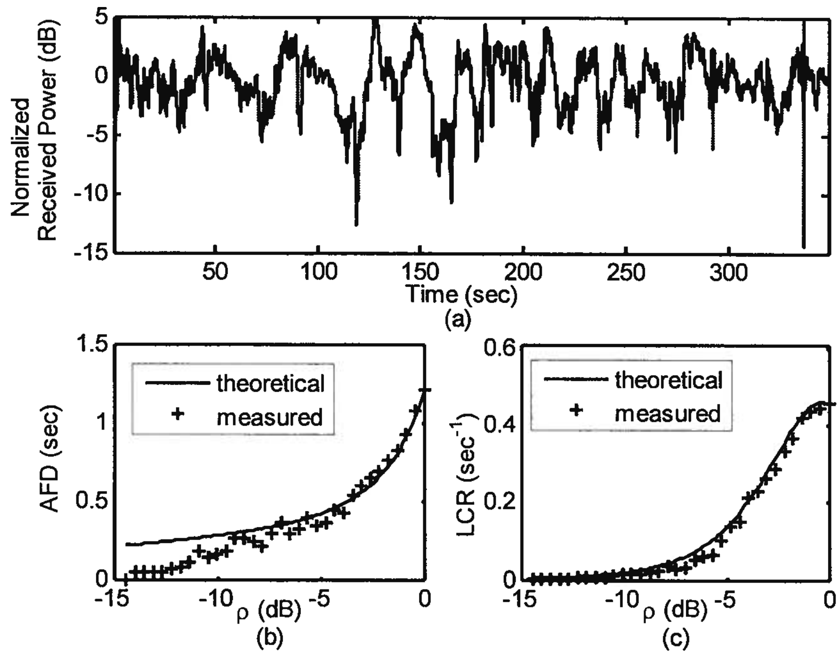

Figure 4.2 – A good fit between theoretical and measured fading distributions for: (a) Measured time series, (b) Averaged fade duration (AFD), and (c) Level crossing rate (LCR), where ρ is the threshold normalized to the rms envelope.

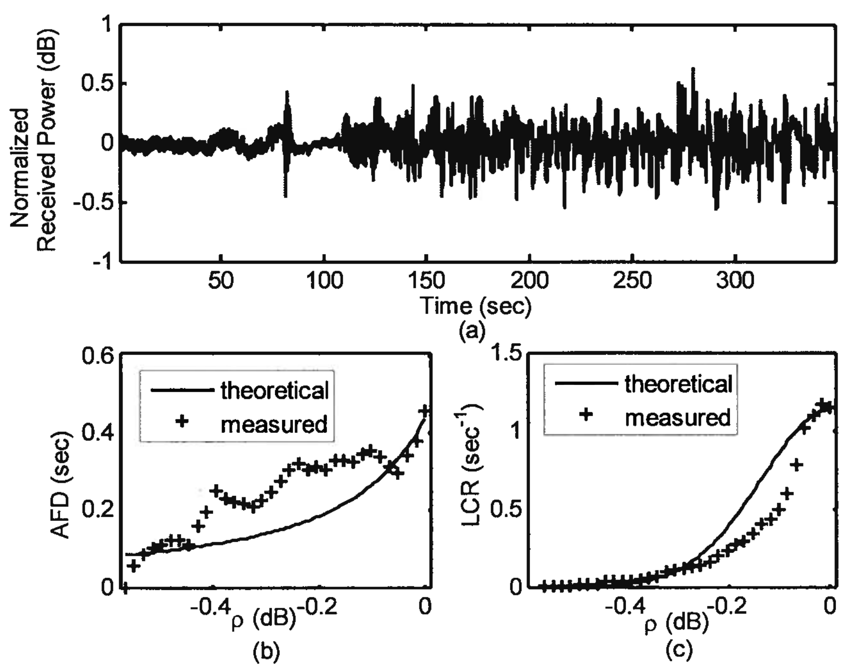

Figure 4.3 – A poor fit between theoretical and measured fading distributions for: (a) Measured time series, (b) Averaged fade duration (AFD), and (c) Level crossing rate (LCR), where ρ is the threshold normalized to the rms envelope.

4.4.2 Significance of the Equivalent Doppler Frequency

If the remote terminal is in motion and scattering is two-dimensional and isotropic, the Doppler spectrum of the fading signal follows Clarke's model and f_d in (4.4) and (4.5) is given by

$$f_d = k\, f_{d,\max}\,, \tag{4.8}$$

where k = 1. If the scattering is non-isotropic and/or the terminal is not in motion, the shape of the Doppler spectrum will be quite different. During the calibration and validation protocol described in Section III-B, we determined the value of k that applies to various Doppler spectrum shapes. We found that as the fraction of energy in the high frequency portion of the spectrum decreases, so does k. In particular, the 6-dB classic, flat and rounded spectra described in [30] yielded $k = 0.91$, 0.74 and 0.58, respectively. Further work will be required to determine the corresponding relationship for spectra more typical of those observed in fixed wireless environments, e.g., [21],[14].

4.4.3 Joint-Distribution of Equivalent Doppler Frequencies

Over the 92 measurement locations and in all three frequency bands, the effective maximum Doppler frequency distributions are well approximated by lognormal distributions (i.e., normal in dBHz). Therefore, these effective maximum Doppler frequency values at 220, 850, and 1900 MHz bands can be cast as a three-element vector of jointly random Gaussian processes which are completely specified by the means, standard variations, and mutual correlation coefficients.

The mean values of the effective maximum Doppler frequency at 220, 850, and 1900 MHz bands are 1.62, 2.46, and 0.34 dBHz (or 1.45, 1.76, and 1.08 Hz, respectively.) The standard deviations of the effective maximum Doppler frequency in these bands are 2.03, 2.99 and 2.87 dBHz, respectively. The correlation matrix between the Doppler frequencies observed in these bands is given by

$$\rho = \begin{bmatrix} 1 & 0.63 & 0.61 \\ 0.63 & 1 & 0.64 \\ 0.61 & 0.64 & 1 \end{bmatrix} \tag{4.9}$$

where the rows and columns correspond to the bands in the sequence given above. It is apparent that the marginal distributions of the effective maximum Doppler frequencies are very similar among the three frequency bands. In particular, the rate of signal fading is not proportional to carrier frequency, as a simplistic model involving moving scatterers might suggest, e.g., [21]. This constraint will provide useful guidance to those who seek to develop detailed physical models of fade dynamics on fixed wireless channels in suburban macrocell environments.

4.4.4 Ricean K-factor and Equivalent Doppler Frequency vs. Average Wind Speed

From previous work, it is well known that the Ricean K-factor drops as the average wind speed increases. However, the corresponding relationship between the effective maximum Doppler frequency and the average wind speed, and the effect of carrier frequency on the relationship between K and f_d and the average wind speed has not been previously revealed. Our results for K and f_d vs. the average wind speed in the 220, 850 and 1900 MHz bands are presented in Figure 4.4 and Figure 4.5 respectively.

We estimated the regression line that best fits our measured data, the correlation coefficient between each parameter and the average wind speed, and the location variability of the parameter, i.e., the variation of the parameter about the regression line at a given average wind speed. The regression line for K and f_d, and the corresponding correlation coefficients ρ and location variabilities σ in each frequency band are given by

$$\overline{K}_{220}(\text{dB}) = 0.066 v_W + 31.0; \qquad \rho = 0.03,\ \ \sigma = 6.8\ \text{dB} \tag{4.10}$$

$$\overline{K}_{850}(\text{dB}) = -0.47 v_W + 21.7; \qquad \rho = -0.23,\ \ \sigma = 7.0\ \text{dB} \tag{4.11}$$

$$\overline{K}_{1900}(\text{dB}) = -0.64 v_W + 18.42; \qquad \rho = -0.31,\ \ \sigma = 7.0\ \text{dB} \tag{4.12}$$

and

$$\overline{f_d}_{220}(\text{dBHz}) = -0.18 v_W + 2.56; \qquad \rho = -0.32,\ \ \sigma = 1.9\ \text{dBHz} \tag{4.13}$$

$$\overline{f_d}_{850}(\text{dBHz}) = -0.096 v_W + 2.95; \qquad \rho = -0.11,\ \ \sigma = 3.0\ \text{dBHz} \tag{4.14}$$

$$\overline{f_{d\,1900}}(\mathrm{dBHz}) = -0.36 v_W + 2.17\,; \qquad \rho = -0.45\,, \quad \sigma = 2.6\ \mathrm{dBHz} \tag{4.15}$$

respectively, where the average wind speed, v_W, is expressed in km/h. In general, both K and f_d are weakly but negatively correlated with the average wind speed in all three bands. In the 220 MHz band, K and the average wind speed are effectively uncorrelated.

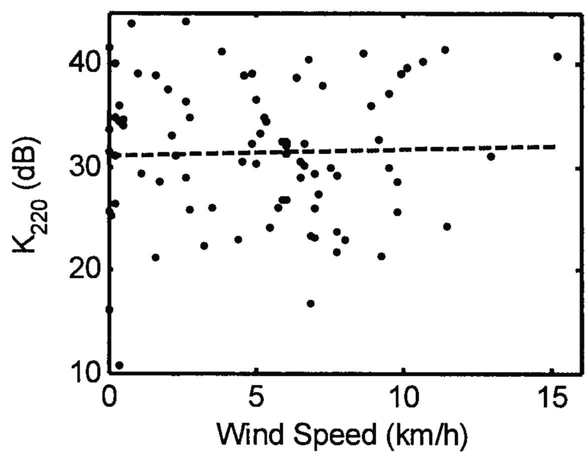

(a)

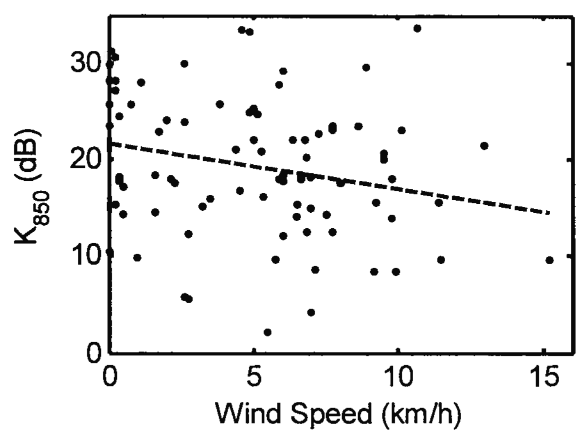

(b)

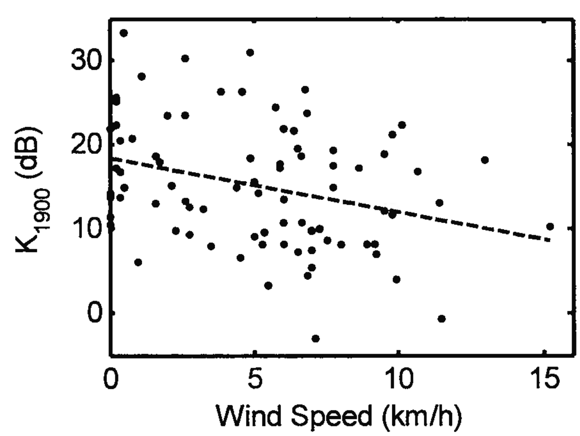

(c)

Figure 4.4 – Ricean K-factors observed at (a) 220 MHz, (b) 850 MHz and (c) 1900 MHz *vs.* the average wind speed.

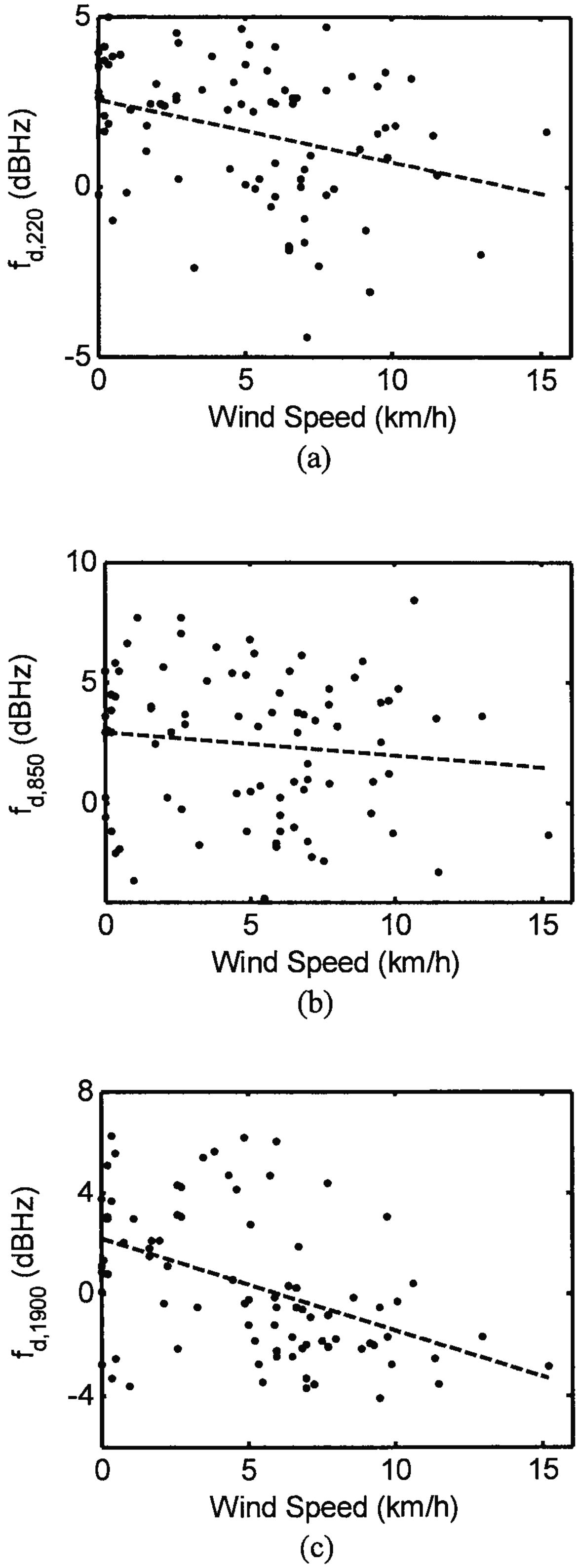

Figure 4.5 – Effective maximum Doppler frequency observed at (a) 220 MHz, (b) 850 MHz and (c) 1900 MHz *vs.* the average wind speed.

4.4.5 Ricean K-factor and Equivalent Doppler Frequency vs. Distance

From previous work, it is well known that the Ricean K-factor tends to present a slight negative correlation with distance. However, the corresponding relationship between the effective maximum Doppler frequency and distance, and the effect of carrier frequency on the relationship between K and f_d and distance has not been previously revealed. Our results for K and f_d vs. distance in the 220, 850 and 1900 MHz bands are presented in Figure 4.6 and Figure 4.7 respectively.

We estimated the regression line that best fits our measured data, the correlation coefficient between each parameter and the distance, and the location variability of the parameter, i.e., the variation of the parameter about the regression line at a given distance. The regression line for K and f_d and the corresponding correlation coefficients ρ and location variabilities σ in each frequency band are given by

$$\overline{K}_{220}(\mathrm{dB}) = -5.8\log_{10} d + 33.2; \qquad \rho = -0.14, \ \ \sigma = 6.7 \text{ dB}, \tag{4.16}$$

$$\overline{K}_{850}(\mathrm{dB}) = -6.8\log_{10} d + 21.4; \qquad \rho = -0.16, \ \ \sigma = 7.1 \text{ dB}, \tag{4.17}$$

$$\overline{K}_{1900}(\mathrm{dB}) = -1.83\log_{10} d + 15.7; \qquad \rho = -0.04, \ \ \sigma = 7.4 \text{ dB}, \tag{4.18}$$

and

$$\overline{f}_{d\,220}(\mathrm{dBHz}) = -1.9\log_{10} d + 2.2; \qquad \rho = -0.16, \ \ \sigma = 2.0 \text{ dBHz}, \tag{4.19}$$

$$\overline{f}_{d\,850}(\mathrm{dBHz}) = -1.4\log_{10} d + 2.90; \qquad \rho = -0.08, \ \ \sigma = 3.0 \text{ dBHz}, \tag{4.20}$$

$$\overline{f}_{d\,1900}(\mathrm{dBHz}) = 0.53\log_{10} d + 0.18; \qquad \rho = 0.03, \ \ \sigma = 2.9 \text{ dBHz}, \tag{4.21}$$

respectively, where distance, d , is expressed in km. In general, both K and f_d are very weakly but negatively correlated with distance in the 220 and 850 MHz bands. In the 1900 MHz band, neither K nor f_d are correlated with distance.

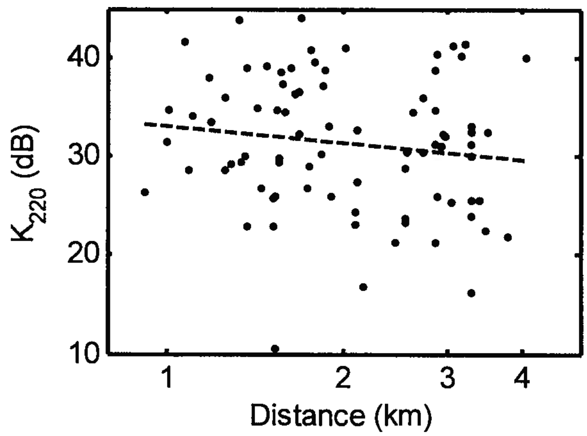

(a)

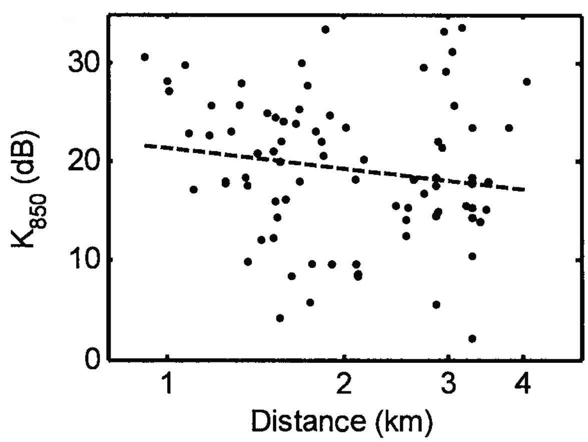

(b)

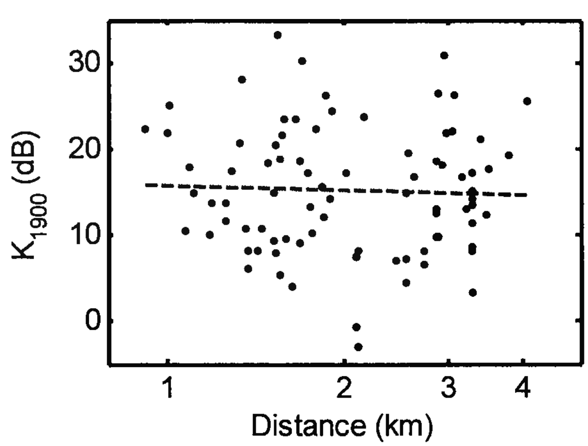

(c)

Figure 4.6 – Ricean K-factors observed at (a) 220 MHz, (b) 850 MHz and (c) 1900 MHz *vs.* distance.

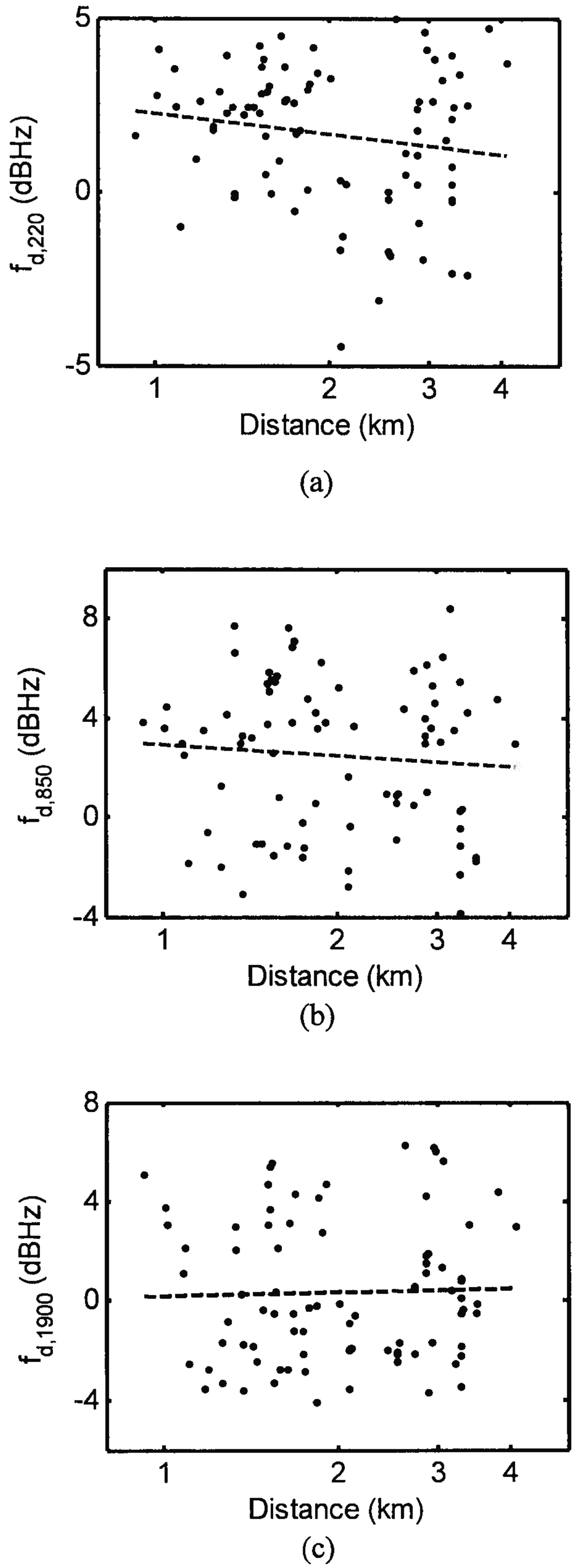

Figure 4.7 – Effective maximum Doppler frequencies observed at (a) 220 MHz, (b) 850 MHz and (c) 1900 MHz *vs.* distance.

4.4.6 Joint Dependency of the Ricean K-factor and Equivalent Doppler Frequency

We found that the Ricean K-factor (in dB) and the effective maximum Doppler frequency (in dBHz) both present normal distributions. This suggests that the two may be cast as jointly Gaussian random variables with specified mean, standard deviation and mutual correlation coefficient. Scatter plots of K and f_d in the 220. 850 and 1900 MHz bands are presented in Figure 4.8 together with the corresponding regression lines and correlation coefficients given by

$$\overline{f_{d\,220}}(\text{dBHz}) = 0.089\overline{K}_{220}(\text{dB}) - 1.18\,; \qquad \rho = 0.3\,, \tag{4.22}$$

$$\overline{f_{d\,850}}(\text{dBHz}) = 0.26\overline{K}_{850}(\text{dB}) - 2.48\,; \qquad \rho = 0.62\,, \tag{4.23}$$

$$\overline{f_{d\,1900}}(\text{dBHz}) = 0.26\overline{K}_{1900}(\text{dB}) - 3.56\,; \qquad \rho = 0.66\,, \tag{4.24}$$

that best fit the data in a least-squares sense. The mean and standard deviations of K (in dB) in the 220, 850 and 1900 MHz bands are given by

$$\overline{K} = [31.4 \text{ dB} \quad 19.3 \text{ dB} \quad 15.2 \text{ dB}]\,, \tag{4.25}$$

$$\sigma_K = [6.8 \text{ dB} \quad 7.2 \text{ dB} \quad 7.4 \text{ dB}]\,. \tag{4.26}$$

The corresponding mean and standard deviations of f_d are given in (4.19)-(4.21).

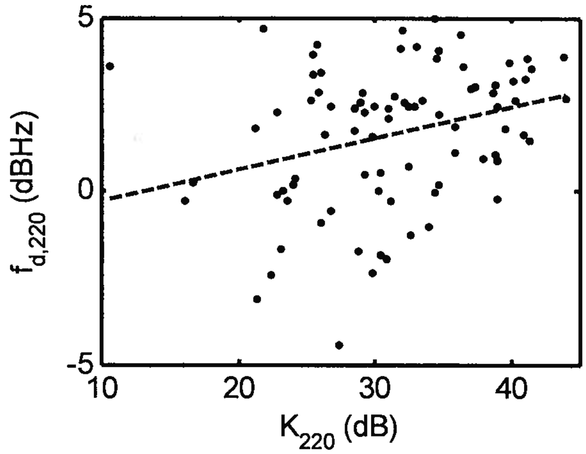

(a)

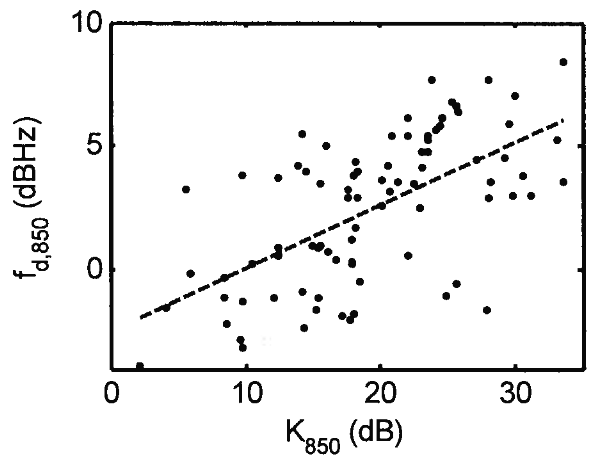

(b)

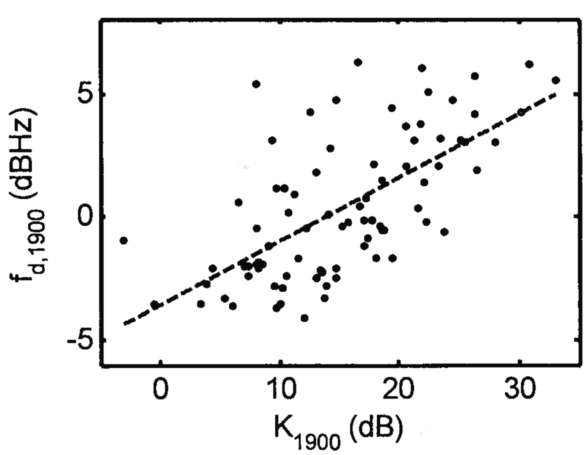

(c)

Figure 4.8 – Ricean K-factor vs. effective maximum Doppler frequency observed at (a) 220 MHz, (b) 850 MHz and (c) 1900 MHz.

4.5 Conclusions

We observed Ricean fading signals on 220, 850 and 1900 MHz fixed wireless channels at 92 locations within a typical suburban macrocell environment and compared the observed LCR and AFD distributions to sets generated using theoretical expressions that normally apply to mobility scenarios where the fading statistics are Ricean and the Doppler spectrum is predominantly classical or U-shaped. Our results corroborate Feick *et al.*'s observation [12] that even though the fixed Doppler spectrum assumes a much different shape than it does in mobility scenarios, substituting an appropriate value for what would normally be the maximum Doppler frequency (and which we refer to here as the effective maximum Doppler frequency) into the theoretical expressions for the LCR and AFD distributions often yields a good match to the fixed wireless observations. Further, we have shown how transient peaks, fades, or non-stationary behaviour in the fading signal affect the fit of the measured LCR and AFD curves to their theoretical counterparts and have provided convincing evidence that fitting the theoretical LCR curve to the measured curve provides the most robust and reliable results. Finally, we recount preliminary results that suggest that the ratio of the effective maximum Doppler frequency to the maximum Doppler frequency: (1) is determined by the shape of the Doppler spectrum and (2) decreases as the fraction of energy in the high frequency components of the Doppler spectrum decreases.

Our most significant finding is that the effective maximum Doppler frequency observed at a given location is not proportional to the carrier frequency as: (1) a model based upon the radial motion of moving scatterers would predict and (2) what others have observed in conventional indoor and mobility environments. This suggests that simple physical models of indoor fixed wireless channels such as those proposed by Thoen *et al.* [21] do not apply to fixed wireless channels in suburban macrocell environments and that a more sophisticated physical model is required. Further, we found that the effective maximum Doppler frequency is effectively independent of either distance or average wind speed and is lognormally distributed about its mean value, which typically falls between 1 and 2 Hz. Although the lognormal distribution suggests that the randomness is the result of a multiplicative process, determining the precise details is a task for future work.

The results presented here will provide useful guidance to those who seek to: (1) simulate channels encountered in suburban macrocell environments with high transmitting sites and moderate foliage or (2) develop detailed physical models of propagation in such environments.

Development of measurement-based models of the depth and rate of channel fading applicable to a broad range of environments will require additional data collected: (1) at other sites, (2) with transmitters at different heights and (3) at additional frequencies within the range of interest

References

[1] W. Webb, "Broadband fixed wireless access as a key component of the future integrated communications environment," *IEEE Commun. Mag.*, vol. 39, no. 9, pp. 115-121, Sep. 2001.

[2] K. Lu, Y. Qian and H-H Chen, "Wireless broadband access: WIMAX and beyond," *IEEE Commun. Mag.*, vol. 45, no. 5, pp. 124-130, May 2007.

[3] S. S. Venkata, A. Pahwa, R. E. Brown, and R. D. Christie, "What future distribution engineers need to learn," *IEEE Trans. Power Syst.*, vol.19, no.1, pp. 17-23, Feb. 2004.

[4] G. Simard and D. Chartrand, "Hydro-Quebec's Economic and Technical Approach to Justify its Distribution Automation Program," in *Proc. IEEE PES'07,* pp. 1-5, 24-28 Jun. 2007.

[5] S. Jim, W. Carr, and S. E. Collier, "Real time distribution analysis for electric utilities," in *Proc. IEEE REPC'08,* pp. B5-B5-8, 27-29 Apr. 2008.

[6] D. G. Michelson, V. Erceg, and L. J. Greenstein, "Modeling diversity reception over narrowband fixed wireless channels," in *Proc. IEEE MTT-TWA'99*, pp. 95-100, 21-24 Feb. 1999.

[7] L. J. Greenstein, S. S. Ghassemzadeh, V. Erceg and D. G. Michelson, "Ricean K-factors in narrowband fixed wireless channels: Theory, experiments and statistical models," in *Proc. WPMC'99*, 21-23 Sep. 1999.

[8] S. Perras and L. Bouchard, "Fading characteristics of RF signals due to foliage in frequency bands from 2 to 60 GHz," in *Proc. WPMC'02*, 27-30 Oct. 2002, pp. 267-271.

[9] M. J. Gans, N. Amitay, Y. S. Yeh, T. C. Damen, R. A. Valenzuela, C. Cheon and J. Lee, "Propagation measurements for fixed wireless loops (FWL) in a suburban region with foliage and terrain blockages," *IEEE Trans. Wireless Commun.*, vol. 1, no. 2, pp. 302-310, Apr. 2002.

[10] E. R. Pelet, J. E. Salt, and G. Wells, "Effect of wind on foliage obstructed line-of-sight channel at 2.5 GHz," *IEEE Trans. Broadcasting*, vol. 50, no. 3, pp. 224-232, 2004.

[11] D. Crosby, V. S. Abhayawardhana, I. J. Wassell, M. G. Brown, and M. P. Sellars, "Time variability of the foliated fixed wireless access channel at 3.5 GHz," in *Proc. IEEE VTC 2005 Spring*, 25-28 Sep. 2005, pp. 106-110.

[12] H. Suzuki, C. D. Wilson, and K. Ziri-Castro, "Time variation characteristics of wireless broadband channel in urban area," presented at *EuCAP'06*, Nice, France, 2-6 Nov. 2006.

[13] R. Feick, R. A. Valenzuela and L. Ahumada, "Experiment results on the level crossing rate and average fade duration for urban fixed wireless channels," *IEEE Trans. Commun.,* vol. 9, no. 1, pp. 175-179, Jan. 2007.

[14] S. Thoen, L. V. D. Perre, and M. Engels, "Modeling the channel time-variance for fixed wireless communications," *IEEE Communic. Lett.*, vol. 6, no. 8, pp. 331-333, Aug. 2002.

[15] A. Domazetovic, L. J. Greenstein, N. B. Mandayam, and I. Seskar, "Estimating the Doppler spectrum of a short-ranged fixed wireless channel," *IEEE Communic. Lett.*, vol. 7, no. 5, pp. 227-229, May 2003.

[16] K. E. Baddour and N. C. Beaulieu, "Accurate simulation of multiple cross-correlated Rician fading channels," *IEEE Trans. Commun.* vol. 52, no. 11, pp. 1980-1987, Nov. 2004.

[17] B. Natarajan, C. R. Nassar and V. Chandrasekhar, "Generation of correlated Rayleigh fading envelopes for spread spectrum applications," *IEEE Communic. Lett.*, vol. 4, no. 1, pp. 9-11, Jan. 2000

[18] "Policy for the Use of 700 MHz Systems for Public Safety Applications and Other Limited Use of Broadcasting Spectrum," Industry Canada Radio Systems Policy, RP-006 – Issue 1, Jun. 2006.

[19] "Proposals and Changes to the Spectrum in Certain Bands below 1.7 GHz," Industry Canada Gazette Notice DGTP-004-05, Dec. 2005.

[20] M. Hata, "Empirical formula for propagation loss in land mobile radio services," *IEEE Trans. Veh. Technol.,* vol. 29, no. 3, pp. 317-325, Aug. 1980.

[21] E. Damosso, Ed., "Digital Mobile Radio Toward Future Generation Systems - Final Report," COST 231 Final Report, 1996.

[22] V. Erceg, L. J. Greenstein, S. Y. Tjandra, S.R. Parkoff, A. Gupta, B. Kulic, A. A. Julius, and R. Bianchi, "An empirically based path loss model for wireless channels in suburban environments," *IEEE J. Sel. Areas Commun.,* vol. 17, no. 7, pp. 1205-1211, July 1999.

[23] D. A. J. Pearce, A. G. Burr and T. C. Tozer, "Modelling and predicting the fading performance of fixed radio links through vegetation," in *Proc. IEE NCAP'99,* 31 Mar.-1 Apr. 1999, pp. 263-266.

[24] P. Lédl, P. Pechač and M. Mazánek, "Time-series prediction of attenuation caused by trees for fixed wireless access systems operating in millimeter waveband," in *Proc. IEE ICAP'03,* 31 Mar.-3 Apr. 2003, pp. 646-649.

[25] M. Cheffena and T. Ekman, "Modeling the dynamic effects of vegetation on radiowave propagation," in *Proc. IEEE ICC'08*, 19-23 May 2008, pp. 4466-4471.

[26] L. J. Greenstein, D. G. Michelson, and V. Erceg, "Moment-method estimation of the Ricean K-factor," *IEEE Commun. Lett,* vol. 3, no. 6, pp. 175-176, Jun. 1999.

[27] S. R. Hanna and J. C. Chang, "Representativeness of wind measurements on a mesoscale grid with station separations of 312 m to 10 km," *Boundary-Layer Meteorol,* vol. 60, pp. 309-324, 1992.

[28] D. S. Baum, D. A. Gore, R. U. Nabar, S. Panchanathan, K. V. S. Hari, V. Erceg and A. J. Paulraj, "Measurements and characterization of broadband MIMO fixed wireless channels at 2.5 GHz," in *Proc. IEEE ICPWD'00,* 17-20 Dec. 2000, pp. 203-206.

[29] V. Erceg et al., "Channel models for fixed wireless applications," IEEE 802.16 Broadband Wireless Access Working Group, IEEE 802.16a-03/01, 27 Jun. 2003.

[30] "SR5500 Wireless Channel Emulator Operations Manual," Spirent Communications, Eatontown, NJ, 2006, pp. 3-16.

5 A First-Order Model for Depolarization of Propagation Signals by Narrowband Ricean Fading Channels[4]

5.1 Introduction

Polarization diversity on narrowband fixed wireless links has traditionally been characterized in terms of the fading statistics and the cross-correlation between the Rician distributed signals on each branch, e.g., [1]. A complementary approach, which provides additional physical insight and which is independent of the polarization states of the diversity receiving antennas, is to characterize the manner in which the polarization states observed at the receiver disperse across the Poincaré sphere. In the absence of fading, the polarization state of the signal that is observed at the receiver will describe a single point. As the depth of fading increases and as the correlation between the signals observed on the diversity receiving branches decreases, the polarization states observed by the receiver will begin to disperse. In the limit as the fading distribution on the branches becomes uncorrelated and Rayleigh, the polarization states will be uniformly distributed across the sphere.

The notion that it may be useful to consider the manner in which the polarization states associated with wireless signals disperse across the Poincaré sphere has previously been considered in [2] and [3]. To the best of our knowledge, however, we are the first to consider polarization state dispersion by Ricean fading channels. The polarization state distribution that one expects to see at the receiving antenna is of particular interest to those engaged in the simulation and test of polarization diversity or polarization adaptive antennas. Knowledge of the polarization state distribution also allows one to estimate of the level of cross-polar discrimination (XPD) on the channel. Such information is of particular interest to those engaged in the development and evaluation of polarization re-use or polarized MIMO schemes, e.g., [4],[5].

In this work, we show that the manner in which polarization states disperse across the Poincaré sphere over time, i.e., the first-order statistics of dispersion, is well-described by a

[4] A ver sion of this chapter has been accepted for publication: K.N. Sivertsen, A. Liou, and D.G. Michelson, "A First-Order Model for Depolarization of Propagating Signals by Narrowband Ricean Fading Channels."

spherical normal or Fisher distribution and how the parameters of this distribution are related to the narrowband channel parameters that describe the diversity channel. We also show how knowledge of the polarization state distribution might be used to predict the level of cross-polar discrimination (XPD) on the channel.

The remainder of this paper is organized as follows: In Section 5.2, we describe the concept in greater detail and explain our methodology. In Section 5.3, we show how dispersion of polarization states over time is related to the conventional narrowband channel parameters. In Section 5.4, we show that the dispersion of polarization states is closely correlated with XPD. In Section 5.5, we summarize our contributions and their implications.

5.2 Concept and Methodology

In [1], it was shown that the first-order statistics of the Ricean fading signals $g_1(t)$ and $g_2(t)$ observed on diversity receiving branches are completely described by: (1) the average path gains G and Ricean K-factors K observed on each branch and (2) the cross-correlation coefficient ρ between the time varying components of the signals on each receiving branch. In such cases,

$$g_1(t) = \sqrt{\frac{G_1}{K_1+1}}\left[\sqrt{K_1} + x_1(t)\right] \tag{5.1}$$

and

$$g_2(t) = \sqrt{\frac{G_2}{K_2+1}}\left[\sqrt{K_2}e^{j\Delta\Psi} + x_2(t)\right], \tag{5.2}$$

where $x_1(t)$ and $x_2(t)$ are zero-mean complex Gaussian processes with unit standard deviation and $\Delta\psi$ is the phase offset between the fixed components of $g_1(t)$ and $g_2(t)$ that may result depending upon the relationship between the transmit and receive polarizations.

We denote the correlation between the complex Gaussian variates x_1 and x_2 by

$$\rho = \overline{x_1 x_2^*} = \mathrm{R}e^{j\theta}. \tag{5.3}$$

If the phase between the fixed components is assumed to be zero, the power correlation coefficient ρ_{pwr} between the envelopes of g_1 and g_2 is related to ρ, the correlation between the complex Gaussian variates x_1 and x_2, by

$$\rho_{pwr} = \frac{R^2 + 2\mu_c\sqrt{K_1K_2}}{\sqrt{(1+2K_1)(1+2K_2)}}, \tag{5.4}$$

where the real part of the complex correlation coefficient is given by

$$\mu_c = R\cos\theta, \tag{5.5}$$

as described in [6],[7]. In the remainder of this paper, we use ρ_{pwr} to indicate the degree of cross-correlation between diversity branches.

When the angle of arrival distribution is sufficiently narrow that the antenna pattern appears to be constant over the range, e.g., as one might observe at a base station in a macrocell environment or at the satellite end of an earth-space link, the polarization state of the signal observed at the receiver at a given instant can be determined from knowledge of the amplitude and phase of the signals received on orthogonally polarized receiving branches at that instant. The arctangent of the ratio of the signal amplitudes gives the polarization angle γ while the difference between the signal phases gives the polarimetric phase δ. Trigonometric relations that relate the polarization angle and polarimetric phase to the ellipticity angle ε and tilt angle τ that define the polarization ellipse can be derived using spherical trigonometry, as described in [8].

The amplitude distribution of a Ricean distributed signal with a given K-factor and noise amplitude σ^2 is given by the well-known expression

$$\begin{aligned} p(r) &= \frac{r}{\sigma^2}\exp\left[-\tfrac{r^2+V^2}{2\sigma^2}\right] I_0\left(\tfrac{rV}{\sigma^2}\right), \quad r \ge 0 \\ p(r) &= 0, \qquad\qquad\qquad\qquad\qquad\quad r < 0 \end{aligned}, \tag{5.6}$$

where $I_0(z)$ is the modified Bessel function of the first kind of order zero. The phase distribution is given by

$$\begin{aligned} p(\vartheta) &= \frac{1}{2\pi\sigma^2}\exp\left(\tfrac{-V^2}{2\sigma^2}\right) \\ &\cdot\left[\sigma^2 + \tfrac{V}{2}\sqrt{2\pi}\sigma\cos\vartheta\exp\left(\tfrac{V^2\cos^2\vartheta}{2\sigma^2}\right)\left(1+\mathrm{erf}\left(\tfrac{V\cos\vartheta}{2\sigma^2}\right)\right)\right] \end{aligned}, \tag{5.7}$$

where

$$erf(G) = \frac{2}{\sqrt{\pi}}\int_0^G e^{-y^2}\,dy. \tag{5.8}$$

Although one could derive closed form expressions for the polarization angle and polarimetric phase distributions using (5.6) and (5.7), the effort required would be considerable. We therefore opted to use numerical simulations to determine the manner in which the polarization states of the received signal disperse across the Poincaré sphere over time.

Polarization diversity receiving antennas are usually chosen to be both symmetrically and orthogonally polarized. For example, when the transmitted signal is vertically polarized, we might use forward and back slanted diagonally polarized receiving antennas. The inherent symmetry between the two branches suggests that the fading statistics on the two channels might reasonably be assumed to be identical, i.e., identical path gains G and Ricean K-factors K. We refer to this as an *ideal* Ricean diversity channel. By assuming such a channel, we can reduce the number of independent first-order channel model parameters to just three: G, K and ρ_{pwr}.

Because the average path gains G on the two branches are identical, they cancel out when we calculate the polarization ratio and therefore do not affect the polarization state. For each instance of K and ρ_{pwr} that we considered, we generated almost 10,000 values of $g_1(t)$ and $g_2(t)$ using a cross-correlated Ricean channel simulator. From the ratio $g_1(t)/g_2(t)$ at a given instant, we determined the polarization angle γ and the polarimetric phase δ, or, alternatively, the ellipticity and tilt angles, ε and τ, that define the polarization state of the received signal. Finally, we plotted the polarization states on a Poincaré sphere, as suggested by Figure 5.1, where the longitude coordinate $\varphi' = 2\tau$ and the co-latitude coordinate $\theta' = 90 - 2\varepsilon$ in degrees. The polarization states corresponding to horizontal and vertical, right and left circular, and $\tau = +45°$ (forward slant) and $+135°$ (back slant) with $\varepsilon = 0°$ are indicated.

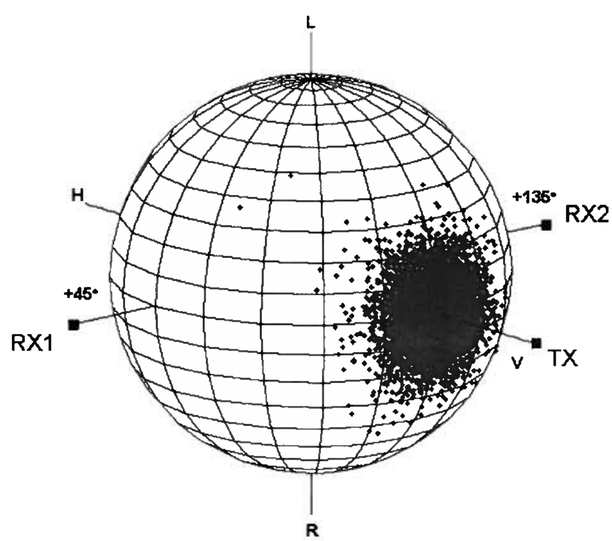

Figure 5.1 - Dispersion of polarization states on the Poincaré sphere when fading signals observed on the forward and back-slant polarized receiving antennas RX1 and RX2 are characterized by $K = 10$ dB and $\rho_{pwr} = 0.8$. The transmitted signal was vertically polarized but has been depolarized by the environment.

5.3 Results

The manner in which polarization states are distributed across the Poincaré sphere for various K and ρ_{pwr} is presented in Figure. 5.2. In order to facilitate assessment of the rotational symmetry of the distributions, we have rotated the spherical coordinate frame used in Figure 5.1 so that the polarization state corresponding to the mean direction is coincident with one of the poles of the rotated coordinate frame. For ease of visualization as the distribution broadens, we displayed the rotated Poincaré sphere using Lambert's equal area azimuthal projection. Because this projection maps equal areas on the sphere onto equal areas on the plane, it preserves the density of polarization states. The centre of each plot in Figure 5.2 corresponds to vertical polarization while the outer circle corresponds to horizontal polarization.

The polarization state distributions in Figure 5.2 may be considered to be the result of a correlated random walk. When K is very large, the polarization state distribution is effectively confined to a sufficiently small portion of the sphere in the vicinity of the transmitter polarization state that it may effectively be considered a plane. In such cases, the central limit theorem predicts that the distribution will tend to conform to a two-dimensional isotropic Gaussian distribution. When K approaches zero, the polarization state distribution is unconstrained and covers the entire sphere. In such cases, the central limit theorem predicts that the random walk will conform to a spherical uniform distribution.

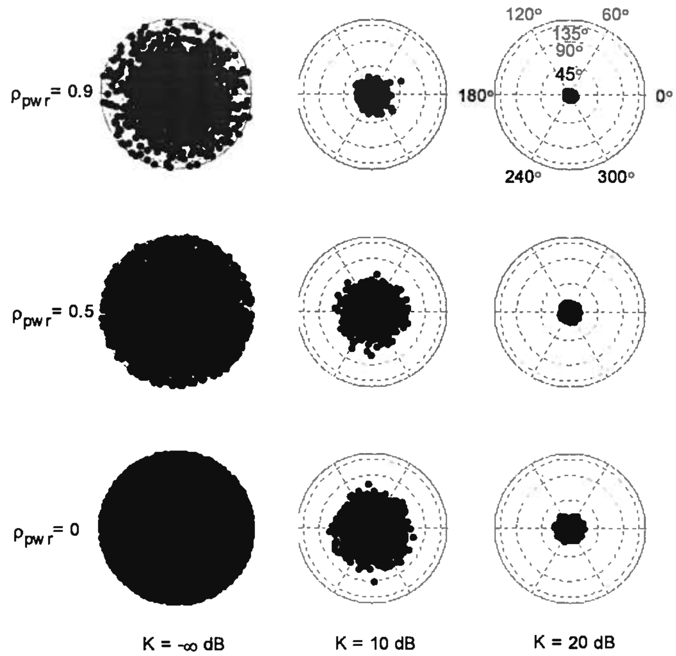

Figure 5.2 – Dispersion of polarization states on a Lambert equal area azimuthal projection of the Poincaré sphere when the fading signals observed on forward and back slant polarized receiving antennas are characterized by the indicated values of K (dB) and ρ_{pwr}.

Although no general theory of correlated random walks on a sphere yet exists to guide us when considering intermediate values of K, the behavior of the polarization state distribution for very large and small values of K is very similar to that exhibited by the Fisher or *spherical normal* distribution given by

$$f(\theta,\phi) = \frac{\kappa \sin\theta}{2\pi\left(e^{\kappa} - e^{-\kappa}\right)} e^{\kappa\left(\sin\theta \sin\alpha \cos(\phi-\beta) + \cos\theta \cos\alpha\right)} \tag{5.9}$$

for very large and small values of κ, where θ and ϕ are the co-latitude and longitude (elevation and azimuth angle) in the local spherical coordinate frame, κ is the concentration parameter, and α and β are the co-latitude and longitude, respectively, of the mean direction [9]. If the polarization state distributions for arbitrary values of K and ρ_{pwr} are, in fact, well approximated by Fisher distributions with an appropriate value of κ, effective methods for compactly representing and simulating such distributions become available. In particular, methods for simulating pseudo random samples of the Fisher distribution, and which, by extension, may be used to simulate polarization state distributions, are presented in [10]-[12].

If the mean direction of a Fisher distribution is located at a pole of the sphere (e.g., $\alpha = 0°$, β arbitrary) then the distributions in θ and φ are independent and separable. In that case, the marginal distribution in φ is the uniform distribution, while the marginal distribution in θ is given by

$$f(\theta) = \kappa \sin\theta \frac{e^{\kappa\cos\theta}}{e^{\kappa} - e^{-\kappa}}. \tag{5.10}$$

The maximum likelihood estimate of the mean direction is given by the sample mean direction [13]. Experimental data may require estimators for the concentration parameter κ that are robust against outliers, or have been modified for small ($N < 16$) sample sizes [14]-[17]. Because neither are issues here, we simply used the maximum likelihood estimator,

$$\coth\kappa - \frac{1}{\kappa} = \frac{R}{N}, \tag{5.11}$$

that is given in [9]. The Fisher distributions with concentration parameters κ that best fit the simulated data sets corresponding to selected values of K between -∞ and 20 dB and ρ_{pwr} between 0 and 0.9 are shown in Figure 5.3. We decimated the data to ensure that the samples were independent then performed a pair of tests to assess: (i) the uniformity of the marginal distribution in longitude φ and (ii) the goodness-of-fit of the marginal distribution in co-latitude θ to the exponential component of the Fisher distribution [14]. Because the parameters of the proposed distributions have been estimated from simulated data, we have used standard test statistics that have been modified as described in [18],[19].

Our first task was to verify that the simulated data is rotationally symmetric. Let X_i be a random sample from a hypothesized distribution $F(x)$, and let $X_{(i)}$ be the order statistics of the sample so that $X_{(1)} \le \ldots \le X_{(N)}$ Following [13], we compared the value of Kuiper's test statistic,

$$V_N = \max\left[\frac{i}{N} - F\left(X_{(i)}\right)\right] + \max\left[F\left(X_{(i)}\right) - \frac{(i-1)}{N}\right], \tag{5.12}$$

for i = 1, …, N, modified for the case when the distribution is continuous and completely specified (in this case uniform) by

$$V = V_N\left(\sqrt{N} + 0.155 + \frac{0.24}{\sqrt{N}}\right), \tag{5.13}$$

to standard test statistics, and were able to accept the hypothesis of rotational symmetry at a significance level greater than 15%.

We then assessed the fit of the probability distribution in (10) to the marginal distribution of the data in θ. Following [13] once again, we compared the value of the Kolmogorov-Smirnov test statistic,

$$D_N = \max\left[\max\left[\frac{i}{N} - F\left(X_{(i)}\right)\right], \max\left[F\left(X_{(i)}\right) - \frac{(i-1)}{N}\right]\right], \tag{5.14}$$

modified for the case when the distribution is exponential with estimated parameters as

$$D = \left(D_N - \frac{0.2}{N}\right)\left(\sqrt{N} + 0.26 + \frac{0.5}{\sqrt{N}}\right) \tag{5.15}$$

to standard test statistics, and confirmed what is apparent from visual inspection of Figure 5.3: The Fisher distribution fits the simulated data well for most values of K and ρ_{pwr} but slightly over predicts the polarization state dispersion in the unlikely case that the fading distribution is close to Rayleigh while the branches are also highly correlated.

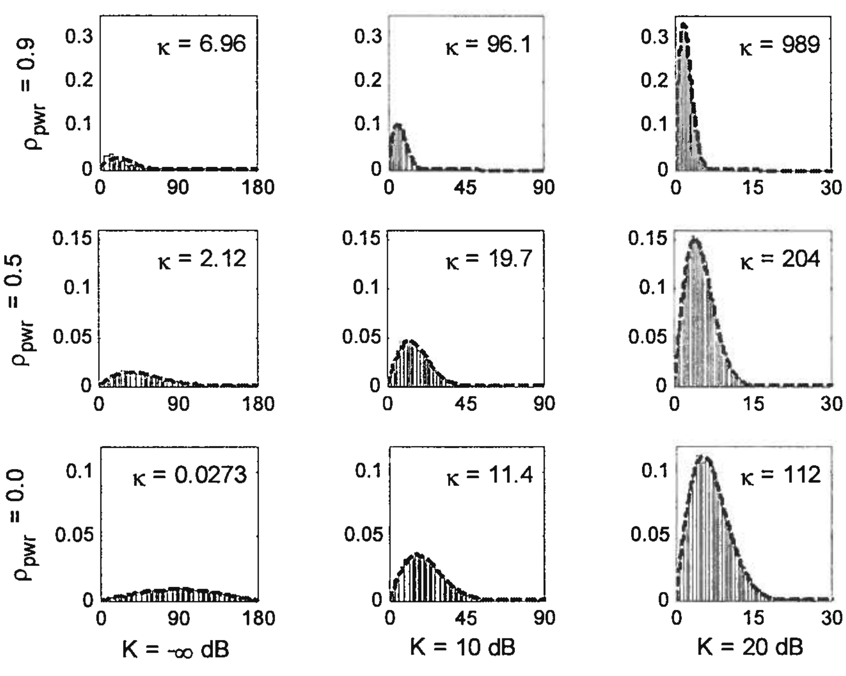

Figure 5.3 - The Fisher distributions that best fit the co-latitude component of the polarization state distribution for selected values of K between -∞ and 20 dB and ρ_{pwr} between 0 and 0.9.

In Figure 5.4, we show the manner in which the logarithmic form of the concentration parameter depends upon K and ρ_{pwr}. As K increases, the variation in the polarimetric ratio decreases so $\log_{10}\kappa$ also increases, i.e., the polarization state distribution becomes more concentrated. A similar effect occurs as ρ_{pwr} increases and the instantaneous amplitudes of the signals on the two branches become more similar. To facilitate estimation of the concentration parameter given the narrowband channel parameters, we generated a polynomial response surface that models the relationship between $\log_{10}\kappa$ and the parameters K and ρ_{pwr}. A third order polynomial surface provides a good fit with an RMS error of 0.04 while a fourth order surface only reduces the error to 0.02 at the expense of far greater complexity. The third order model is given by

$$\begin{aligned}\log_{10}\kappa = \beta_0 + \beta_1 K + \beta_2 \rho_{pwr} + \beta_3 K \rho_{pwr} + \beta_4 K^2 + \beta_5 \rho_{pwr}^2 \\ + \beta_6 K \rho_{pwr}^2 + \beta_7 K^2 \rho_{pwr} + \beta_8 K^3 + \beta_9 \rho_{pwr}^3\end{aligned} \tag{5.16}$$

where

$$\beta = \begin{bmatrix} 0.1133868, 0.0677943, 1.3392816, \text{-}0.0303603, 0.0021740, \\ \text{-}2.4102017, 0.0276632, 0.0007400, \text{-}0.0000464, 2.2787705 \end{bmatrix} \tag{5.17}$$

and K is expressed in dB.

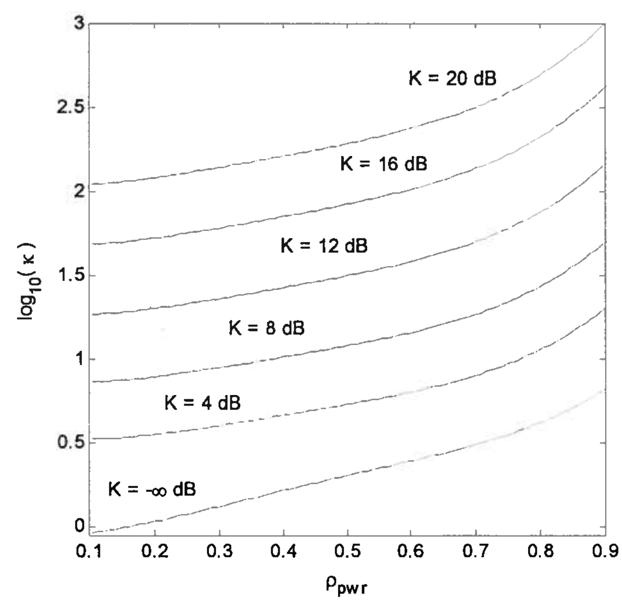

Figure 5.4 – The Fisher concentration parameter κ as a function of the cross-correlation coefficient, ρ_{pwr}, between the orthogonally polarized diversity branches and the Ricean K-factor K (dB) that characterizes fading on each diversity branch.

5.4 Prediction of XPD from Narrowband Channel Parameters

Although previous experimental work has shown that XPD is correlated with Ricean K-factor [20], eqn. (5.9) indicates that the spread of polarization states that determines XPD is actually determined by κ. The results of the last section indicate that κ is determined by both K and ρ_{pwr}. In order to determine how effectively we can predict XPD given κ, K or ρ_{pwr}, we synthesized a multiplicity of fading diversity signals with values of K between -∞ and 20 dB and ρ_{pwr} between 0 and 0.9 and estimated both the corresponding κ and XPD. We found that XPD is more highly correlated with κ (correlation = 0.97) than with K or ρ_{pwr} alone (correlation = 0.58 and 0.60 respectively). The relationship between κ and XPD is shown in Figure 5.5 and is given by

$$\text{XPD [dB]} = 9.82\log_{10}\kappa + 15.05 \quad . \tag{5.18}$$

Together, (5.16) and (5.18) allow XPD to be accurately predicted directly from narrowband channel model parameters of the sort described in [1].

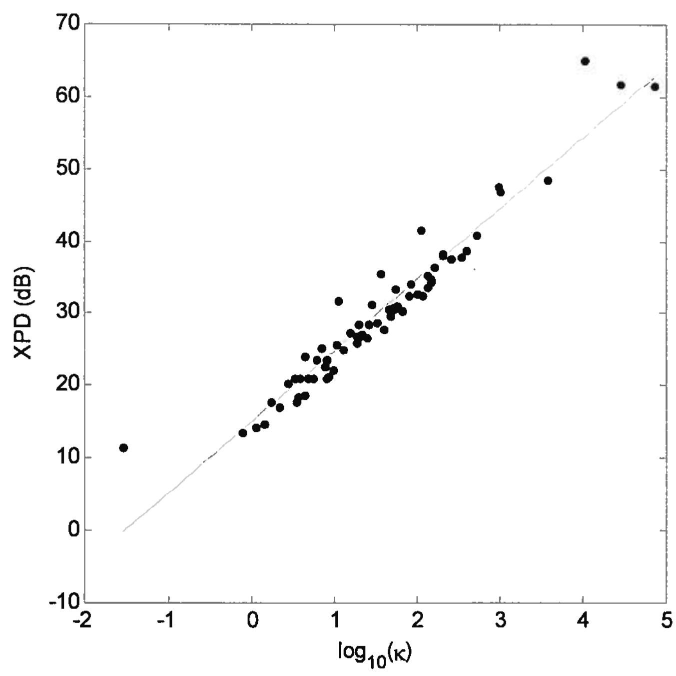

Figure 5.5– Cross-polar discrimination as a function of the Fisher concentration parameter κ. The correlation coefficient between κ and XPD is 0.97.

5.5 Conclusion

We have shown by simulation that when the fading signals observed on polarization diversity branches are Ricean distributed, the first-order distribution of polarization states is generally well-approximated by a Fisher distribution with specified concentration parameter κ. Although one generally needs to measure the phase between diversity branches to determine the received polarization state at a given instant, the concentration parameter κ is a function of the narrowband channel parameters K and ρ_{pwr}, both of which can be estimated from simple measurements of received power *vs.* time. We have also shown that κ is a better indicator than K or ρ_{pwr} alone of the level of cross-polar discrimination (XPD) on the channel, a parameter useful to those engaged in the development and evaluation of polarization re-use or polarized MIMO schemes. In order to simplify interpretation of the results, we have assumed what we refer to as an ideal Ricean fading diversity channel in which the average path gains and Ricean K-factors on both orthogonally polarized diversity branches are identical. We will relax this restriction in the next phase of our study where we will consider how unequal path gains and/or K-factors affect the polarization state distribution.

References

[1] D.G. Michelson, V. Erceg, and L.J. Greenstein, "Modeling diversity reception over narrowband fixed wireless channels," *IEEE MTT-S Int. Topical Symp. Technol. Wireless Applic.* (Vancouver, BC), 21-24 Feb. 1999, pp. 95-100.
[2] D. J. Cichon, T. Kurner and W. Wiesbeck, "Polarimetric aspects in antenna related superposition of multipath signals," *Proc. ICAP 1993*, pp. 80-83, 30 Mar. – 2 Apr.1993.
[3] M. M. McKinnon, "Three-dimensional statistics of radio polarimetry," *Astrophys. J. Suppl.*, vol. 148, no. 2, pp. 519-526, Oct. 2003.
[4] V. R. Anreddy and M. A. Ingram, "Capacity of measured Ricean and Rayleigh indoor MIMO channels at 2.4 GHz with polarization and spatial diversity," *IEEE Proc. IEEE WCNC*, pp. 946–951, April 3-6 2006.
[5] H. Bolcskei, R.U. Nabar, V. Erceg, D. Gesbert and A.J. Paulraj, "Performance of spatial multiplexing in the presence of polarization diversity," *Proc. IEEE ICASSP*, pp. 2437–2440, May 7-11 2001.
[6] J. R. Mendes, M. D. Yacoub and D. Benevides da Costa, "Closed-form generalised power correlation coefficient of Ricean channels," *Eur. Trans. Telecomms,* vol. 18, pp. 403–409, 2007.
[7] Y. Karasawa and H. Iwai, "Modeling of signal envelope correlation of line-of-sight fading with applications to frequency correlation analysis," *IEEE Trans. Communic.*, vol. 42, no. 6, pp. 2201–2203, 1994.
[8] W. L. Stutzman, *Polarization in Electromagnetic Systems*, Boston: Artech House, 1993.
[9] R. Fisher, "Dispersion on a sphere," *Proc. Roy. Soc. London Ser. A*, vol. 217, no. 1130, pp. 295-303, May 1953.
[10] G. Ulrich, "Computer generation of distributions on the m-sphere," *Appl. Statist.*, vol. 33, no. 2, pp. 158-163, 1984.
[11] A. T. A. Wood, "Simulation of the von Mises Fisher distribution," *Commun. Statist. - Simula.*, vol. 23, no. 1, pp. 157-164, 1994.
[12] N. I. Fisher, T. Lewis, M. E. Willcox, "Tests of discordancy for samples from Fisher's distribution on the sphere," *Appl. Statist.*, vol. 30, no. 3, pp. 230-237, 1981.
[13] N. I. Fisher, T. Lewis, and B. J. J. Embleton, *Statistical Analysis of Spherical Data.* Cambridge: Cambridge Univ. Press, 1987.
[14] K. V. Mardia and P. E. Jupp, *Directional Statistics*, New York: Wiley, 2000.
[15] P. L. McFadden, "The best estimate of Fisher's precision parameter κ," *Geophys. J. R. Astr. Soc.*, vol. 60, pp. 397-407, 1980.
[16] D. J. Best and N. I. Fisher, "The bias of the maximum likelihood estimators of the von Mises-Fisher concentration parameters," *Commun. Statist.*, vol. B10, pp. 493-502, 1981.
[17] N.I. Fisher, "Robust estimation of the concentration parameter of Fisher's distribution on the sphere," *Applied Statistics*, vol. 31, no. 2, pp. 152-154, 1982.
[18] N. I. Fisher and D. J. Best, "Goodness-of-fit tests for Fisher's distribution on the sphere," *Austral. J. Statist.*, vol. 26, no. 2, pp. 151-159, 1984.
[19] M. A. Stephens, "EDF statistics for goodness of fit and some comparisons," *J. Amer. Statistical Assoc.*, vol. 69, no. 2, pp. 730-737, Sep. 1974.
[20] D. S. Baum, D. Gore, R. Nabar, S. Panchanathan, K. V. S. Hari, V. Erceg and A. J. Paulraj, "Measurement and characterization of broadband MIMO fixed wireless channels at 2.5 GHz," *Proc. IEEE ICPWC*, pp. 203–206, Dec. 17–20, 2000.

6 Polarization Dispersion on 1.9 GHz Fixed Wireless Uplink Channels in Suburban Macrocell Environments[5]

6.1 Introduction

As wireless signals traverse the path from a transmitter to a receiver in suburban macrocell environments, they are diffracted and scattered by buildings, foliage and other obstructions along the path. The manner in which such interaction with the environment alters the polarization state of the wireless signal over time has attracted much interest over the years. Initial interest was motivated by the observation that rapid changes in the polarization state of a fading signal over very short time scales make it possible to mitigate signal fading by combining the outputs of relatively compact polarization diversity antennas and thereby avoid the inconvenience associated with deploying relatively bulky space diversity antennas [1]-[8]. Later, concerns that significant and sustained mismatch between the mean polarization state of an incoming signal and the polarization state of the receiving antenna would impair link performance motivated several studies [9]-[14]. Most recently, the possibility of increasing spectral efficiency in fixed wireless systems deployed in suburban macrocell environments by implementing polarization re-use schemes [15]-[20] and increasing both link quality and system capacity by using orthogonally polarized diversity branches in polarization multiplexing and/or polarized MIMO schemes [21]-[25] has attracted interest in characterization of the level of isolation between orthogonally polarized channels, *i.e.,* the level of cross-polar discrimination (XPD).

Polarization diversity receiving antennas are usually chosen to be both symmetrically polarized with respect to the transmitting antenna and orthogonally polarized with respect to each other. For example, when the transmitted signal is vertically polarized, we might use forward and back-slant polarized receiving antennas [3]. Most previous work has characterized polarization diversity on fixed wireless links in terms of the fading statistics on each branch and the cross-correlation coefficient between the time-varying components, *e.g.,* [6]. Such a characterization is particularly useful because the results can be used directly in channel simulations. However, the traditional approach suffers from two significant limitations: (1) the

[5] A ver sion of this chapter has been submitted for publication: A. Liou, K.N. Sivertsen, and D.G. Michelson, "Polarization Dispersion on 1.9 GHz Fixed Wireless Uplink Channels in Suburban Macrocell Environments."

results are generally specific to receiving branches with specified polarization states and (2) the results offer little physical insight concerning such issues as the degree of isolation between orthogonally polarized channels or XPD.

A complementary approach, which provides physical insight and which is independent of the polarization states of the diversity receiving antennas, is to characterize the manner in which polarization states disperse across the Poincaré sphere over time, *i.e.*, to determine the mean and shape of the corresponding polarization state distribution. The notion that it may be useful to consider the manner in which polarization states disperse across the Poincaré sphere has previously been considered in applications as diverse as wireless propagation [26] and radio astronomy [27]. To the best of our knowledge, however, we are the first to use this approach to characterize diversity fading channels and XPD.

In the absence of wind and other disturbances to a fixed wireless channel, the polarization state of a narrowband signal that is observed at the receiver will describe a single point on the Poincaré sphere. As the local wind speed increases, tree branches and other foliage will begin to sway, fading will become more severe, and the correlation between the signals observed on the diversity receiving branches will decrease. At the same time, the polarization states observed by the receiver will disperse across the Poincaré sphere, as suggested by Figure 6.1. Depending upon the nature of the propagation path, the mean of the polarization state distribution may be offset from the polarization state of the transmitted signal as well. In the limit as the fading distributions on the two branches begin to exhibit Rayleigh fading statistics and become uncorrelated, the polarization states will become uniformly distributed across the sphere [28].

In practical situations, polarization state dispersion has three main consequences. First, shifts in the mean polarization state will lead to imbalance in the average path gains and Ricean K-factors observed on the two diversity branches. Such an imbalance will cause diversity combining schemes to be less effective [15]. Second, as dispersion of polarization states about the mean increases, the level of cross-polar discrimination on the channel will decrease and polarization re-use schemes will be less effective. Third, as polarization state dispersion increases, the range of polarization states that a polarization adaptive array will have to synthesize or track will increase greatly. Better understanding of the statistics of polarization state dispersion is therefore of obvious interest to those tasked with: (1) simulation and test of polarization diversity and polarization adaptive antennas and/or (2) the design and evaluation of polarization re-use and polarized MIMO schemes.

In previous work [28], we used simulations of ideal Ricean channels to show that: (1) the distribution of polarization states across the Poincaré sphere, as observed at the receiver, is very well approximated by a Fisher or spherical normal distribution over most values of the Ricean K-factor and cross-correlation coefficient, (2) the Fisher concentration parameter κ is a useful measure of the extent of such polarization state dispersion, (3) κ is completely determined by the fading statistics on each branch and the cross-correlation coefficient between the time-varying components, and (4) in the general case, κ provides a better prediction of the level of XPD than does the Ricean K factor.

The results that we obtained for ideal channels raises some important questions regarding the nature of practical channels: (1) How are the mean polarization states observed at many locations throughout the coverage area distributed about the transmitted polarization state? (2) (a) How well does the Fisher distribution fit the distribution of polarization states observed over a short time at a given location? (b) Do shifts of the mean polarization state away from the transmitter polarization affect the fit to the Fisher distribution? (c) How is the Fisher concentration parameter κ distributed over many locations? (3) How closely is κ correlated with the Ricean K-factors observed on the polarization diversity branches and the level of XPD observed throughout the coverage area? (4) How closely is κ correlated with a physically significant parameter such as the average speed of the wind observed at the base station?

In this paper, we seek to answer the questions posed above by presenting our analysis of narrowband polarization diversity measurement data that we collected in a typical suburban macrocell environment located near the University of British Columbia. In Section 6.2, we describe our first-order model for polarization dispersion. In Section 6.3, we describe the measurement setup that we used to collect our data. In Section 6.4, we describe the distribution of mean polarization states over all locations and the distribution of polarization states about the mean at each location. In Section 6.5, describe a polarization state dispersion simulator that we implemented based upon our results. In Section 6.6, we consider the extent to which the Fisher concentration parameter is correlated with other channel and environmental parameters. In Section 6.7, we summarize our contributions and their implications.

6.2 The Model

6.2.1 Ricean Channels

The complex signal path gain of a narrowband channel (typically tens of kHz wide) over a given time segment (typically several minutes long) is given by

$$g(t) = V + v(t) \tag{6.1}$$

where V is a complex number and $v(t)$ is a complex, zero-mean random time variation caused by wind-blown foliage, vehicular traffic, *etc*. Both V and the parameters of the random process $v(t)$ may change from one narrowband time segment to another. Because experience has shown that $v(t)$ is a complex Gaussian process, the distribution of $|g(t)|^2$ over time is Ricean.

In [6], it was shown that the first-order statistics of the Ricean fading signals $g_1(t)$ and $g_2(t)$ observed on diversity receiving branches are completely described by the average path gains G and Ricean K-factors K observed on each branch and the cross-correlation coefficient ρ between the time varying components of the signals on each receiving branch. In such cases,

$$g_1(t) = \sqrt{\frac{G_1}{K_1 + 1}}\left[\sqrt{K_1} + x_1(t)\right] \tag{6.2}$$

and

$$g_2(t) = \sqrt{\frac{G_2}{K_2 + 1}}\left[\left(\sqrt{K_2}e^{j\Delta\Psi} + x_2(t)\right)\right] \tag{6.3}$$

where $x_1(t)$ and $x_2(t)$ are zero-mean complex Gaussian processes with unit standard deviation and $\Delta\psi$ is the phase offset between the fixed components that may result depending upon the mean polarization state observed at the receiver.

6.2.2 Estimation of the Narrowband Channel Model Parameters

From time series data collected over a given time-frequency segment, it is a simple matter to calculate the average power gain,

$$G = \overline{|g(t)|^2} = |V|^2 + \overline{|v(t)|^2} = |V|^2 + \sigma^2 . \tag{6.4}$$

The rms fluctuation of the envelope about the mean is given by the standard deviation of $|g(t)|^2$ and is denoted by σ_G. The K-factor of the Ricean distribution given by

$$K = |V|^2 / \overline{|v(t)|^2} = |V|^2 / \sigma^2, \tag{6.5}$$

where σ^2 is the variance of the complex Gaussian process. Various methods for estimating K have been proposed; we use the moment-based method described in [29] where

$$K = \frac{|V|^2}{\sigma^2} = \frac{\sqrt{G^2 - \sigma_G^2}}{G - \sqrt{G^2 - \sigma_G^2}}. \tag{6.6}$$

6.2.3 Estimation of the Polarization States

When the angle of arrival distribution is sufficiently narrow that the antenna pattern appears to be constant over the range, *e.g.,* as one might observe at a base station in a macrocell environment, the polarization state of the signal observed at the receiver at a given instant can be determined from knowledge of the amplitude and phase of the signals received on orthogonally polarized receiving branches at that instant. The arctangent of the ratio of the signal amplitudes gives the polarization angle γ while the difference between the signal phases gives the polarimetric phase δ. Trigonometric relations that relate the polarization angle and polarimetric phase to the ellipticity angle ε and tilt angle τ that define the corresponding polarization ellipse can be derived using spherical trigonometry, as described in [30]-[32].

6.2.4 Estimation of XPD

The Cross-Polar Discrimination (XPD) ratio is defined as the ratio of the average power received by a co-polarized antenna to the average power received by a cross-polarized antenna [33]. Because our transmitting antenna is vertically polarized, we define the level of XPD observed by the receiver as

$$XPD = \frac{\overline{P_V}}{\overline{P_H}} = \left(\frac{\overline{E_V}}{\overline{E_H}}\right)^2, \tag{6.7}$$

where P_x refers to the power received by an antenna with polarization state x and E_x refers to the corresponding received field strength. Because our polarization diversity receiving antennas are slant polarized (tilt angles of 45° and 135°), we first transformed the received signals to rectilinear polarization (H-V) by multiplying the corresponding Jones vector by the unitary transform matrix Q, *i.e.*,

$$\begin{bmatrix} E_H \\ E_V \end{bmatrix} = Q \begin{bmatrix} E_/ \\ E_\backslash \end{bmatrix}, \tag{6.8}$$

where

$$Q = \frac{1}{\sqrt{2}} \begin{bmatrix} 1 & -1 \\ 1 & 1 \end{bmatrix}, \tag{6.9}$$

calculated the time average of E_V and E_H, then determined XPD by applying (6.7).

6.2.5 Estimation of the Mean Polarization State

All possible polarization states can be mapped one-to-one onto the surface of a Poincaré sphere where the co-latitude θ corresponds to 90° - 2ε and the longitude ϕ corresponds to 2τ where ε and τ are the ellipticity and tilt angles that define a particular polarization state. The equator of the Poincaré sphere corresponds to all possible linear polarization states while the poles correspond to left and right circular polarization, respectively [30]-[32].

The maximum likelihood estimate of the mean direction of the polarization states in spherical coordinates is given by the sample mean direction

$$\hat{\theta} = \arccos(\hat{z}) \ , \ \hat{\phi} = \arctan\left(\frac{\hat{y}}{\hat{x}}\right) \tag{6.10}$$

where $\hat{x}, \hat{y}, \hat{z}$ are given by

$$\hat{x} = \frac{1}{R}\sum_{i=1}^{N} x_i \ , \ \hat{y} = \frac{1}{R}\sum_{i=1}^{N} y_i \ , \ \hat{z} = \frac{1}{R}\sum_{i=1}^{N} z_i \tag{6.11}$$

and N is the number of samples, R is the resultant length given by

$$R^2 = \left(\sum_{i=1}^{N} x_i\right)^2 + \left(\sum_{i=1}^{N} y_i\right)^2 + \left(\sum_{i=1}^{N} z_i\right)^2 \tag{6.12}$$

and x, y and z are the directional cosines of the spherical data,

$$x_i = \sin\theta_i \cos\phi_i, \ y_i = \sin\theta_i \sin\phi_i \ , \ z_i = \cos\theta_i . \tag{6.13}$$

as described in [34].

6.2.6 The Fisher Distribution and its Parameters

In previous work, we simulated polarization diversity branches that experience ideal Ricean fading and found that the corresponding polarization state distribution is unimodal, rotationally symmetric about the mean polarization state, and well described by the Fisher or *spherical* normal distribution given by

$$f(\theta,\phi)=\frac{\kappa\sin\theta}{2\pi\left(e^{\kappa}-e^{-\kappa}\right)}e^{\kappa\left(\sin\theta\sin\alpha\cos(\phi-\beta)+\cos\theta\cos\alpha\right)} \tag{6.14}$$

where θ and ϕ are the co-latitude and longitude of the polarization states when they are projected onto a Poincaré sphere, *e.g.*, as in Figure 6.1, κ is the Fisher concentration parameter, and α and β are the co-latitude and longitude, respectively, of the mean direction of the polarization states, which corresponds to the mean polarization state [35],[36]. If the spherical coordinate system is transformed through rotation to primed coordinates so that the mean direction is located at a pole of the sphere (*e.g.*, $\alpha' = 0°$, β' arbitrary) in the new coordinate frame, then the distributions in θ' and ϕ' are independent and separable. In that case, the marginal distribution in ϕ' is the uniform distribution, while the marginal distribution in θ' is given by

$$f(\theta')=\kappa\sin\theta'\frac{e^{\kappa\cos\theta'}}{e^{\kappa}-e^{-\kappa}}. \tag{6.15}$$

Experimental data may require estimators for the concentration parameter κ that are robust against outliers, or have been modified for small ($N < 16$) sample sizes [36]-[39]. Because neither are issues here, we simply used the maximum likelihood estimator

$$\coth\kappa-\frac{1}{\kappa}=\frac{R}{N} \tag{6.16}$$

as given in [34].

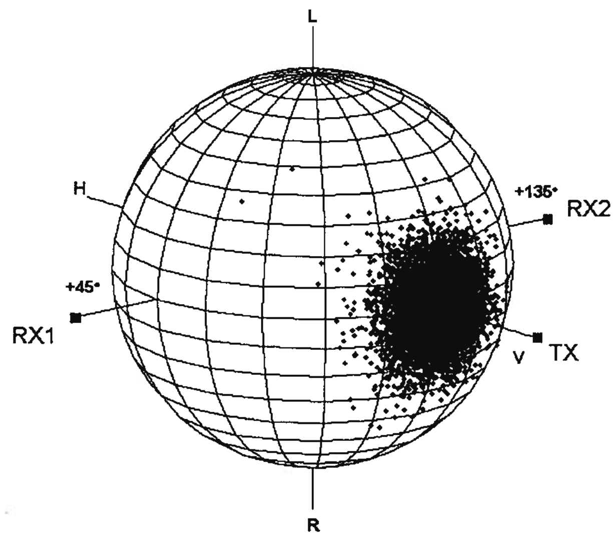

Figure 6.1 – Dispersion of polarization states on the Poincaré sphere when fading signals observed on the forward and back-slant polarized receiving antennas RX1 and RX2 are characterized by $K = 10$ and $\rho_{pwr} = 0.8$. The transmitted signal was vertically polarized but has been depolarized by propagation through the environment.

6.3 The Measurement Setup

6.3.1 CW Channel Sounder

A block diagram of our CW channel sounder is shown in Figure 6.2. It consists of a 1.9 GHz CW transmitter that we carried aboard our drive test vehicle and a dual-channel coherent narrowband measurement receiver that we installed at our base station. A block diagram of the transmitter is shown in Figure 6.2(a). We used a Marconi 2031 RF signal generator to generate a 1 mW CW signal in the 1.9 GHz band. We used an Ophir RF Model 5303075 pre-amplifier and Model 5303062 power amplifier in cascade to bring the transmitted power level up to 6 Watts and a Bird digital RF power meter to measure the precise value. We used a 1.9 GHz vertically polarized omnidirectional sleeve dipole antenna with a gain of 2.2 dBi as our transmitting antenna. Using a sleeve dipole helped us to avoid much of the pattern distortion associated with conventional monopoles mounted upon an imperfect ground plane. Fixed wireless antennas are typically mounted at a heights between 0.5 m (*e.g.*, for nomadic applications) and 4 m (*e.g.*, for permanent installations). As a compromise, we mounted the antenna on the center of the roof of our drive test vehicle at a height of 1.75 m.

A block diagram of the receiver is shown in Figure 6.2(b). We used a Cushcraft 1.9 GHz forward and back-slant polarization diversity antenna with a gain of 7 dBi and beamwidth of 60 degrees as our receiving antenna. We mounted the antenna, mast and rotator atop a tower at a height of 25 m above ground level. When the drive test vehicle was moved to a new location within the survey area, the receiving site operator rotated the antenna boresight towards it. We boosted the signals received on each branch by 25 dB using a pair of Mini-Circuit low noise amplifiers (LNAs) before we applied the signals to an HP 8753E vector network analyzer that we configured to operate in dual-channel tuned-receiver mode with an IF bandwidth of 30 Hz. The receiver provided us with two channels of coherent time series data (amplitude and phase) in a form suitable for polarimetric analysis. A MATLAB script running on a laptop computer controlled the instrument and archived the received data.

We stabilized the frequencies of both the transmitter and receiver using Stanford Research Systems Rubidium frequency standards. Each frequency standard was disciplined over the long term by the 1 pulse per second (PPS) output signal from a Trimble Resolution-T GPS receiver. Although outdoor temperatures were moderate during the measurement campaign, care was taken to protect the Rubidium frequency standard from sudden changes in ambient temperature, *e.g.,* as might be caused by sudden drafts of air. Once per minute, we recorded the average wind speed that was measured by a Davis Vantage Pro2 wireless weather station that we installed on a second tower located near the receiving site. Because previous work has shown that variations in average wind speed at tree top level or above are well correlated over mesoscale distances of several kilometers [40], we considered one wind measurement location near the base station to be adequate for our purposes.

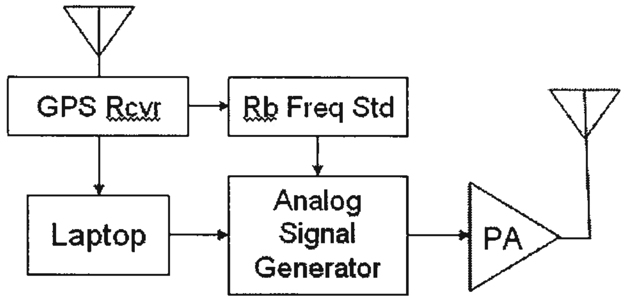

(a)

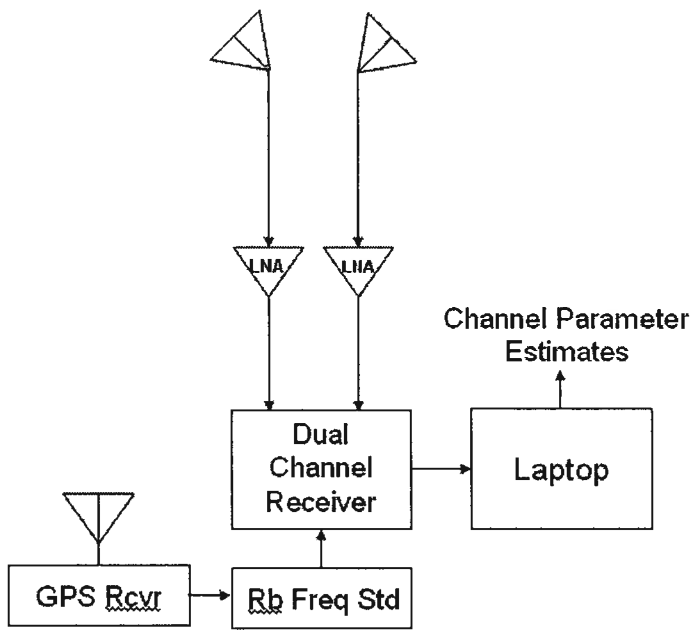

(b)

Figure 6.2 – Measurement setup: (a) CW transmitter and (b) dual-channel receiver.

6.3.2 Calibration and Verification Protocol

Before we collected any field data, we verified the function and operation of our CW channel sounder using a Spirent SR5500 channel emulator that we configured in dual-channel mode. We set relevant narrowband channel parameters including path gain, Ricean K-factor, the cross-correlation coefficient between branches and the width and shape of the Doppler power spectrum to a range of values. In each case, we confirmed that our estimate of the value of each parameter closely matched the value that we had set.

We calibrated the dual-polarized panel antenna, the feedlines and LNAs and the dual-channel receiver using our rooftop antenna range. We began by mounting the dual-polarized panel antenna on a model tower at a separation of about 10 m from a vertically polarized panel antenna that we used as the source. As we rotated the receiving antenna through 360 degrees about the boresight, we recorded the amplitude and relative phase on the diversity receiving branches. This allowed us to determine the correction factors required to compensate for amplitude imbalance, phase imbalance and cross-talk between branches.

With the receiving antenna calibrated and mounted on the base station tower, we mounted the sleeve dipole transmitting antenna atop the elevated roof of the building stairwell. This placed the transmitting antenna about 3 m above the intervening rooftop and about 30 m away from and 5 m below the base station antenna in a configuration somewhat similar to its mount on the drive test vehicle. While the polarization state of a conventional monopole antenna on a compact ground plane was highly distorted, we observed that the polarization state of the sleeve dipole was purely vertical as seen by the receiving site.

6.3.3 Test Area

Our test area consisted of neighborhoods in and around the University of British Columbia and the surrounding University Endowment Lands. Within a test area that we defined by an annulus between 500 and 1500 m from our receiving site, we had access to: (1) residential neighborhoods with tall trees and heavy foliage throughout and (2) light urban areas with two and four storey buildings and comparatively less foliage. Almost all of the motion in the environment arose from wind-blown foliage; few, if any, cars, people or other moving scatterers were present in the vicinity of the drive test vehicle when we collected measurement data. Most of the foliage in the area is coniferous but at least one-third is deciduous. Because the duration of the measurement campaign was only six weeks, we had no opportunity to observe the effects of seasonal variations in the foliage. All of our data was collected with leaves on the trees.

6.3.4 Data Collection Protocol

Our data collection protocol comprised the following steps. First, we conducted a rapid survey of potential survey locations in order to verify that the strength of the received signal at all locations would be adequate. Next, over a span of several weeks, the operator drove the drive test vehicle to each of the 95 survey locations that we had selected in advance and parked for approximately 20 minutes at each one. The operator logged the location of the vehicle using a GPS receiver and logged the transmitted power level.

Once the transmitter was operating at the prescribed survey location, the operator at the receiving site pointed the receiving antenna toward it and then began recording time series measurements of both the amplitude of the signals (in dBm) received on the two diversity branches and their phases relative to the receiver's internal reference (in degrees). The measured data were collected in the form of eight successive 120-second sweeps. Each of the eight sweeps contains 1601 samples collected at 0.075 second intervals or at a sample rate of 13.3 Hz. Although our estimates of the channel parameters at each location are based on 12808 samples, the relatively fast sample rate results in oversampling and fairly high correlation between successive samples. Depending upon the rate of fading (or, equivalently, the width of the Doppler spectrum) at each location, the equivalent number of independent samples in each 960-second time series may range between a few hundred and a few thousand. Collecting data at 95 locations over a range of wind conditions took approximately six weeks.

6.4 Distribution of Polarization States

6.4.1 Distribution of the Mean Polarization States

In macrocell environments, a line-of-sight rarely exists between the transmitter and the receiver. If the polarization state of the dominant or direct ray is transformed as it is scattered or reflected by large fixed structures along the path, the mean polarization state of the cluster may be offset from the polarization state of the transmitting antenna. For systems that use a single antenna, base station antennas that track the mean polarization state of the incoming signal were proposed as a method for mitigating polarization mismatch. In previous work, such antennas were found to improve the link margin by up to 4 dB [13],[14]. In the case of polarization diversity systems, such a mismatch will degrade the performance of the diversity combiner [15]. In this section, we show how the mean polarization states observed over all of the measurement locations are distributed about the transmitted polarization state.

We began by computing the instantaneous polarization states observed at each location during successive instants over the 16-minute observation time, as described in Section 6.2.3. We then computed the mean polarization state in each case by applying (6.10). Finally, we plotted the distribution of the mean polarization states on a Lambert azimuthal equal area projection of the Poincaré sphere. The result for 95 measurement locations is presented in Figure 6.3 where the distribution is both unimodal and symmetric and shows considerable angular spread. Our next step was to characterize the form of the distribution of the mean polarization states. We determined the mean of the mean polarization states over all measurement locations by applying (6.10) once again. As anticipated, the result is within a few degrees of the vertical polarization state of the transmitter.

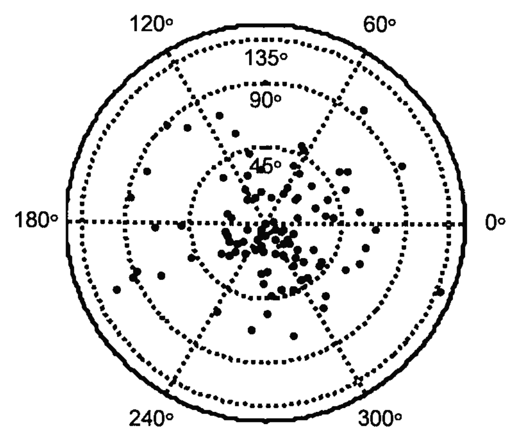

Figure 6.3 – Dispersion of the mean polarization states on a Lambert equal area azimuthal projection of a Poincaré sphere that has been rotated so that the origin corresponds to vertical polarization.

We attempted to fit a Fisher distribution to the co-latitude component of the mean polarization state data. Although a distribution with a concentration parameter $\kappa_m = 3.4$ provides a compelling fit, as shown in Figure 6.4, our measurement database is relatively limited in both size and scope. Considerably more measurement data from a broader range of environments must be collected in order to: (1) prove or disprove the general validity of the Fisher distribution hypothesis and (2) determine the manner in which κ_m is affected by the height of the base station and/or remote terminal, the heights and densities of buildings and other fixed structures, and the heights and densities of trees and other foliage. Nevertheless, these results provide a useful indication of how the mean polarization state will be distributed within suburban macrocell environments with a relatively low base station height of 25 m and a high density of trees and other foliage.

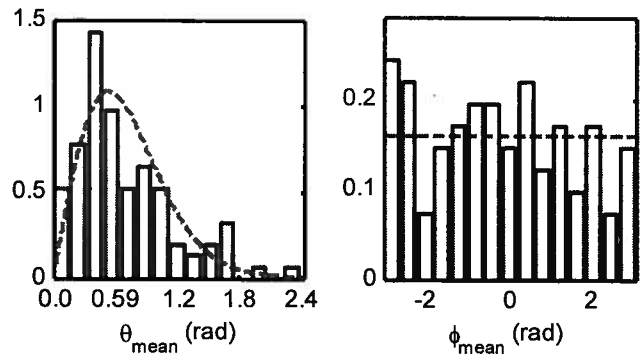

Figure 6.4 – A Fisher distribution with a concentration parameter of 3.4 that best fits the co-latitude and longitude components of the mean polarization states observed over all 95 locations.

6.4.2 Distribution of Polarization States about the Mean

In previous work, we showed that if the signals on orthogonally polarized diversity branches follow ideal Ricean fading statistics, *i.e.,* identical mean signal strength and K-factors on both branches, the distribution of polarization states about the mean polarization state is well-approximated by a Fisher distribution. Here, we consider: (1) how well the Fisher distribution fits the distribution of polarization states observed over a short time at each location, (2) whether shifts of the mean polarization state away from the transmitter polarization affect the fit to the Fisher distribution, and (3) how the Fisher concentration parameter κ distributed over many locations.

In Figure 6.5, we present typical polarization state distributions observed at locations R1 and R7, which are located 800 and 1150 metres from the base station. Figure 6.5(a) gives the polarization state distribution at the first location, R1, where the K-factors on the two diversity branches are 0.012 dB and 5.92 dB, respectively, and the cross-correlation coefficient is 0.47. Figure 6.5(b) presents the polarization state distribution at the second location, R7, where the K-factors on the two diversity branches are 1.45 dB and -0.4 dB, respectively, and the cross-correlation coefficient is 0.01. In both cases, the fading experienced on the diversity branches is asymmetric. In Figure 6.6, we bin the polarization states as a function of co-latitude and longitude angles for the same locations. For the co-latitude angle distributions, we superimpose Fisher distributions with concentration parameter estimates using (6.16), yielding κ of 7.3 and 2.4 dB at locations R1 and R7, respectively. For the longitude distributions, we superimpose a uniform distribution. The closeness of the fit, particularly for the co-latitude distributions, is apparent in both the figures presented here and the remainder of our data set. We used the formal goodness-of-fit tests for the Fisher distribution, as recommended in [36], to assess the similarity of our numerical results to the ideal case. Over all locations, 100% of the longitude distributions passed the Kuiper test at the 15% significance level. Over all locations, 73% of the co-latitude distributions passed the Kolmogorov-Smirnov (K-S) test at the 15% significance level and 87% of the locations passed the K-S test at the 1% level.

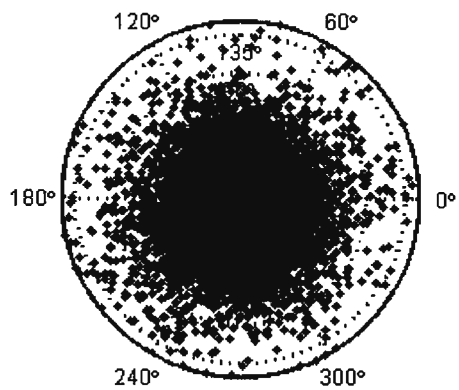

(a)

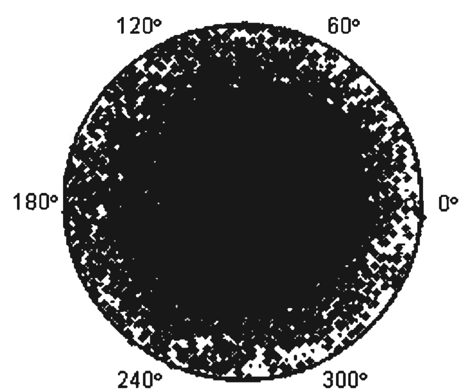

(b)

Figure 6.5 – Dispersion of polarization states on a Lambert equal area azimuthal projection of the Poincaré sphere that has been rotated so that the origin corresponds to vertical polarization. The polarization state data were collected at locations (a) R1 and (b) R7, which are located 800 and 1150 m away from the base station, respectively.

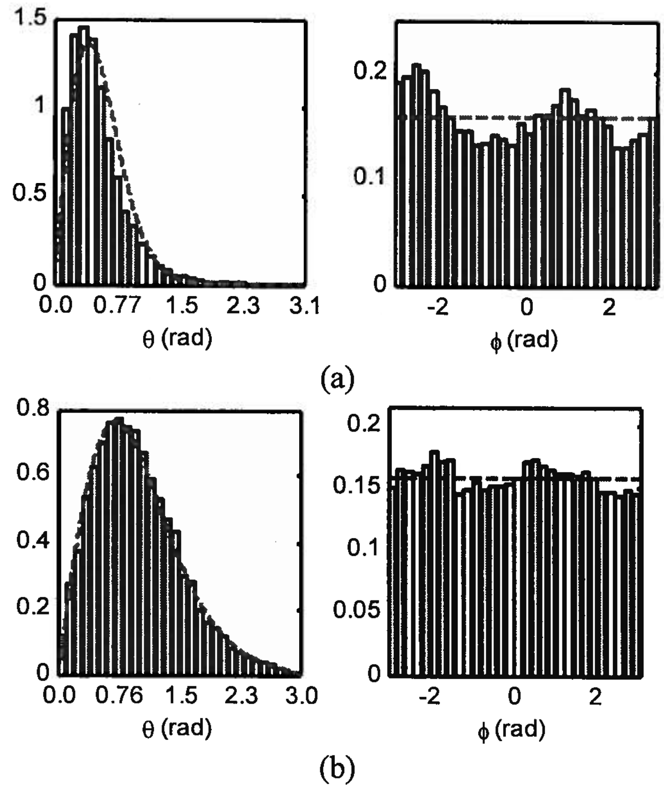

Figure 6.6 – Fisher distributions with concentration parameters of 7.3 and 2.4 dB, respectively, that best fit the co-latitude and longitude components of the polarization state distributions observed at locations (a) R1 and (b) R7.

In Figure 6.7, we present the distribution of κ over all measurement locations. We evaluated several trial distributions including logistic and normal. We obtained the best fit using using a Gumbel (minimum) distribution where

$$f(x) = \frac{1}{\sigma}\exp(-z - \exp(-z)) \tag{6.17}$$

and where $z = (x - \mu)/\sigma$. In this case, the location parameter is $\mu = 3.2$ and the distribution scale is $\sigma = 4.2$. In Figure 6.8, we plot κ vs. the angular offset of the mean polarization state from the transmitter polarization state on the Poincaré sphere. We find that as θ_{mean} increases, both the mean and standard deviation of κ decrease. We fit regression lines to both, yielding

$$\kappa_{mean} = -0.15\,\theta_{mean} + 10 \tag{6.18}$$

and

$$\sigma_{\kappa} = -0.021\,\theta_{mean} + 5.3 \tag{6.19}$$

which are valid for $\theta_{mean} < 250$ degrees.

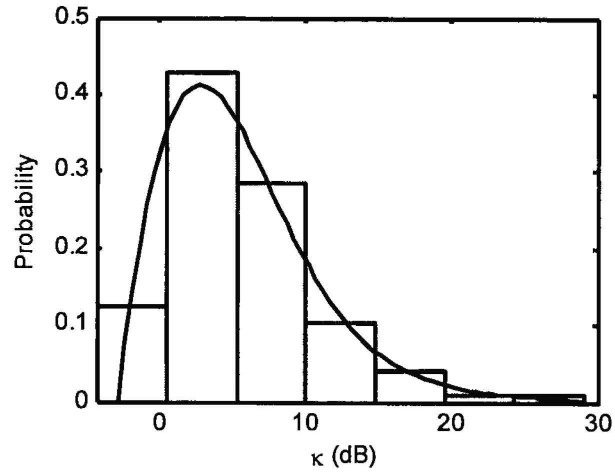

Figure 6.7 – The distribution of the Fisher concentration parameter as observed over all 95 measurement locations.

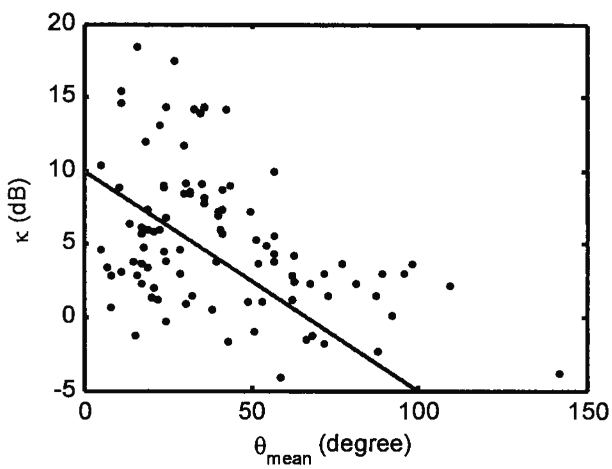

Figure 6.8 – The Fisher concentration parameter as a function of the angular offset of the mean polarization state from the transmitter polarization state on the Poincaré sphere, as observed over all 95 measurement locations.

6.5 A First-Order Simulation Model for the Polarization State Distribution

The results presented in the previous two sections allow us to specify a first-order simulation model for the polarization state distribution observed on given fixed wireless links in environments similar to that in which we conducted our study. First, we require a method for simulating pseudo random samples of Fisher distributed variables in the primed coordinate frame where the mean direction corresponds to upper pole of the sphere or the z' direction, One of the first methods to be developed, which applies to m-dimensional distributions, is presented in [41]. An improved procedure that corrected certain errors and/or oversights in that method was presented in [42]. A simplified method for generating samples Θ' and Φ' of the co-latitude and longitude components of a Fisher distribution in θ' and ϕ', respectively, for $m=3$ from independent uniform (0,1) random variables U and V is given by

$$\Theta' = 2\arcsin\sqrt{\frac{-\ln\left(U(1-\lambda)+\lambda\right)}{2\kappa}} \tag{6.20}$$

and

$$\Phi' = 2\pi V \tag{6.21}$$

where $\lambda = \exp(-2\kappa)$, as described in more detail in [43].

Although it is convenient to generate the Fisher distribution in a spherical coordinate frame where the mean polarization state corresponds to upper pole of the sphere, it is then necessary to rotate the coordinate frame so that the mean polarization state points in the direction $(\theta_{mean}, \phi_{mean})$. This is easily accomplished by transforming $(\theta'_{mean}, \phi'_{mean})$ to $r' \equiv (x', y', z')$, applying the transformation

$$r = \mathbf{T}^{-1} r' \tag{6.22}$$

where the elements of **T** are the direction cosines that relate the basis vectors of the original and primed coordinate systems, and then transforming $r \equiv (x, y, z)$ to $(\theta_{mean}, \phi_{mean})$. If any two unit directions $\hat{r}_1$ and $\hat{r}_2$ ar e known in both coordinate frames, a third unit direction $\hat{r}_3$ can be determined from their normalized cross product. **T** is then given by

$$T = \begin{bmatrix} x'_1 & x'_2 & x'_3 \\ y'_1 & y'_2 & y'_3 \\ z'_1 & z'_2 & z'_3 \end{bmatrix} \begin{bmatrix} x_1 & x_2 & x_3 \\ y_1 & y_2 & y_3 \\ z_1 & z_2 & z_3 \end{bmatrix}^{-1} . \tag{6.23}$$

Our simulation model for the polarization state distribution proceeds as follows:

1. Given κ_m, use (6.20) and (6.21) to generate the mean polarization state given by $(\theta_{mean}, \phi_{mean})$ that is experienced over a short time at a particular location.

2. Given θ_{mean}, use (6.18) to find $\bar{\kappa}$, the mean value of κ.

3. Given θ_{mean}, use (6.19) to find σ_κ, the standard deviation of κ.

4. Given $\bar{\kappa}$ and σ_κ, find κ using

$$\kappa = \bar{\kappa} + X_{\sigma_\kappa}, \tag{6.24}$$

where X_{σ_κ} is a random variable with $(0, \sigma_\kappa)$.

5. Given κ, use (6.20) and (6.21) to generate a multiplicity of polarization states in the $(\theta'_{mean}, \phi'_{mean})$ coordinate frame where the mean polarization state corresponds to the upper pole of the sphere.

6. Rotate the coordinate system using (6.22) so that the mean direction of the polarization state distribution lies in the direction given by $(\theta_{mean}, \phi_{mean})$.

6.6 Correlation of the Fisher Concentration Parameter with other Parameters

In the previous section, we showed that polarization state distributions over short periods are well-described by a Fisher distribution with given mean polarization state and concentration parameter κ. We also developed a simulation model capable of generating polarization distributions with the same statistical properties as our measured data. Here, we consider the degree to which the Fisher concentration parameter is correlated with other channel and environmental parameters, including the Ricean K-factor, the level of cross-polar discrimination on the channel, and the average wind speed in the vicinity of the base station and, by extension, the surrounding coverage area.

6.6.1 Correlation of the Fisher Concentration Parameter with the Ricean K-factor

We have previously used simulations of ideal Ricean channels to show that a strong positive correlation exists between κ and the Ricean K-factor. In Figure 6.9, we plot the Ricean K-factor (in dB) observed on both diversity branches at each measurement location as a function of the value of κ, also in dB, that describes the extent of the polarization state distribution. The strong correlation, $\rho = 0.87$, between the two parameters is apparent. The relationship between K and κ (both in dB) is described by the regression line

$$K(\text{dB}) = 0.94\kappa(\text{dB}) - 3.18. \tag{6.25}$$

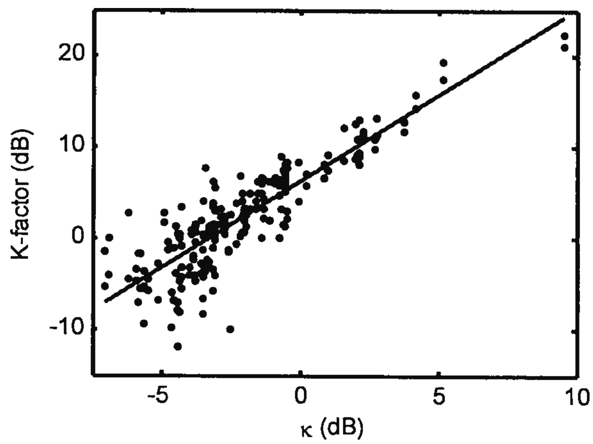

Figure 6.9 – The Ricean K-factor as a function of the Fisher concentration parameter, as observed over all 95 measurement locations.

6.6.2 Correlation of the Fisher Concentration Parameter with XPD

We have previously used simulations of ideal Ricean channels to show that κ is a good predictor of the level of XPD on the channel [28]. In Figure 6.10, we plot the level of XPD (in dB) observed at each measurement location as a function of the value of κ, also in dB, that describes the extent of the polarization state distribution. The high correlation between the two parameters is apparent. The relationship between XPD and κ is described by the regression line

$$XPD(\text{dB}) = 0.61\,\kappa(\text{dB}) + 3.3 \tag{6.26}$$

where $\rho = 0.83$. By contrast, the relationship between XPD and K is given by

$$XPD(\text{dB}) = 0.48\,K(\text{dB}) + 5.8 \tag{6.27}$$

where $\rho = 0.71$.

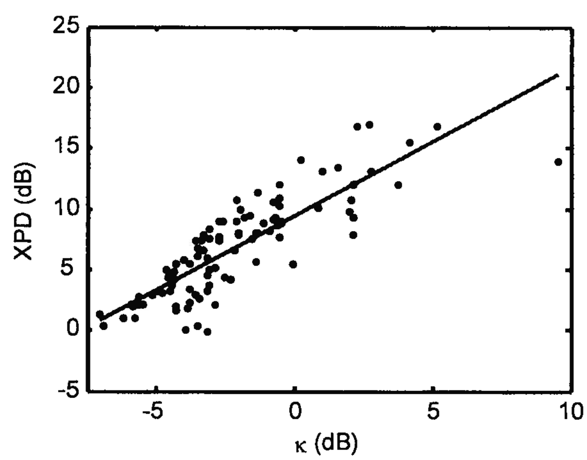

Figure 6.10 – The cross-polar discrimination as a function of the Fisher concentration parameter, as observed over all 95 measurement locations.

6.6.3 Correlation of κ with Average Wind Speed

In Figure 6.11, we plot the value of κ (in dB) observed at each measurement location as a function of the average wind speed, $\bar{v}_{wind}$, (in km/h) observed at the base station during the measurement. The moderate inverse correlation between the two parameters is apparent. The relationship between κ and average wind speed is described by the regression line

$$\kappa(\text{dB}) = -0.06\,\bar{v}_{wind}(\text{km/h}) + 1.09 \tag{6.28}$$

where ρ = -0.36. The relationship between K and average wind speed is described by the regression line

$$K(\text{dB}) = -0.66\,\bar{v}_{wind}(\text{km/h}) + 8.0 \tag{6.29}$$

where ρ = -0.37.

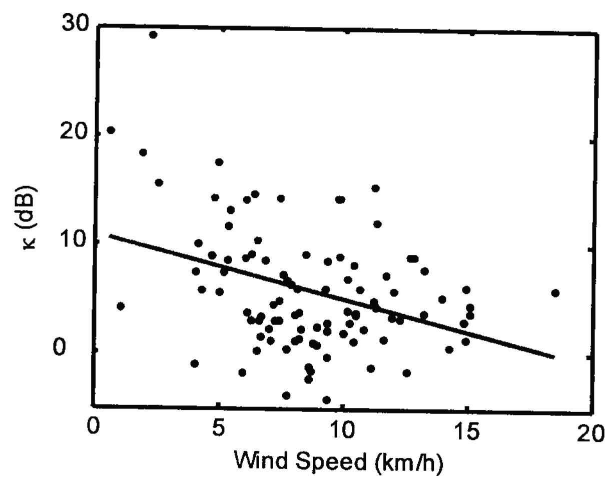

Figure 6.11 – The Fisher concentration parameter, κ, as observed over all 95 measurement locations, as a function of the average wind speed observed at the base station.

6.7 Conclusions

We have characterized the manner in which the polarization states observed on 1.9 GHz fixed wireless uplink channels disperse across the Poincaré sphere during short-term measurement sessions conducted at 95 different locations in a suburban macrocell environment with heavy foliage and using a 25-metre-high base station antenna. While our measurement database is too small to allow us to construct a model that can be applied to a broad range of neighbourhoods and environments, it provides: (1) useful insights concerning the manner in which fixed wireless channels depolarize signals in environments that are similar to our study area and (2) a useful guide to those who pursue follow-on measurement-based studies in other neighbourhoods and environments.

Over all measurement locations, we found that: (1) The mean polarization state is dispersed about the vertical polarization state of the transmitter and tends to follow a Fisher or spherical normal distribution with a concentration parameter κ_m of approximately 3.4. (2) Regardless of the offset between the mean polarization state and the polarization state of the transmitter, the polarization states are symmetrically distributed about the mean polarization state and tend to be well approximated by a Fisher distribution with a concentration parameter κ.

When we expressed the Fisher concentration parameter in dB, we found that it is: (1) well-described by a Gumbel (minimum) distribution over all measurement locations, (2) positively correlated with both Ricean K-factor (in dB) and the level of cross-polar discrimination (XPD) on the channel (in dB) and (3) negatively correlated with average speed of the wind blowing through foliage along the path. Moreover, as we have previously found in the case of simulated channels, XPD is more closely correlated with κ than the Ricean K-factor. Average wind speed is equally well correlated with κ and the Ricean K-factor.

Our results concerning the manner in which polarization states disperse across the Poincaré sphere are of particular interest to those tasked with simulation and test of polarization diversity and adaptive antennas. Our results concerning the distribution of mean polarization states, polarization state dispersion and the loss of XPD are of particular interest to those involved in the design and evaluation of polarization re-use and polarized MIMO schemes.

References

[1] W. C-Y Lee, "Polarization diversity system for mobile radio," *IEEE Trans. Commun.*, vol. 20, no. 5, pp. 912-923, Oct. 1972.

[2] S. Kozono, T. Tsuruhara, and M. Sakamoto, "Base station polarization diversity reception for mobile radio," *IEEE Trans. Veh. Technol.*, vol. 33, no. 4, pp. 301-306, Nov. 1984.

[3] R.G. Vaughan, "Polarization diversity in mobile communications," *IEEE Trans. Veh. Technol.*, vol. 39, no. 3, pp. 177-186, Aug. 1990.

[4] J. Laiho-Steffens, J. Lempiainen, M. Salmenkaita, J. Siltaniemi, and O. Jukarainen, "Experimental evaluation of polarisation diversity gain at the base station end in a GSM900 network," in *Proc. IEEE VTC 1998*, 18-21 May 1998, pp. 16-20.

[5] M. Bengtsson, D. Astely, and B. Ottersten, "Measurements of spatial characteristics and polarization with a dual polarized antenna array," in *Proc. IEEE VTC 1999*, Jul. 1999, vol. 1, pp. 366-370.

[6] D. G. Michelson, V. Erceg, and L.J. Greenstein, "Modeling diversity reception over narrowband fixed wireless channels," in *Proc. IEEE MTT-S Int. Topical Symp. Technol. Wireless Applic.* (Vancouver, BC), 21-24 Feb. 1999, pp. 95-100.

[7] R. M. Narayanan, K. Atanassov, V. Stoiljkovic, and G. R. Kadambi, "Polarization diversity measurements and analysis for antenna configurations at 1800 MHz," *IEEE Trans. Antennas Propag.*, vol. 52, no. 7, pp. 1795-1810, Jul. 2004.

[8] A. Dunand and J.M. Conrat, "Dual-polarized spatio-temporal characterization in urban macrocells at 2GHz," in *Proc. IEEE VTC 2007*, 30 Sept. – 3 Oct. 2007, pp. 854-858.

[9] D. C. Cox, "Antenna diversity performance in mitigating the effects of portable radiotelephone orientation and multipath propagation," *IEEE Trans. Commun.*, vol. 31, no. 5, pp. 620-628, May 1983.

[10] D. C. Cox, R. R. Murray, H. W. Arnold, A. W. Norris and M. F. Wazowicz, "Cross-polarization coupling measured for 800 MHz radio transmission in and around houses and large buildings," *IEEE Trans. Antennas Propag.*, vol. 34, no. 1, pp. 83-87, Jan. 1986.

[11] D. P. Stapor, "Optimal receive antenna polarization in the presence of interference and noise," *IEEE Trans. Antennas Propag.*, vol. 43, no. 5, pp. 473-477, May 1995.

[12] Y. Yang, R. Tao, and Y. Wang, "A new SINR equation based on the polarization ellipse parameters," *IEEE Trans. Antennas Propag.*, vol. 53, no. 4, pp. 1571-1577, Apr. 2005.

[13] J. Shapira and S. Miller, "A novel polarization smart antenna," *Proc. IEEE VTC Spring 2001*, 6-9 May 2001, pp. 253–257.

[14] S. Gao, A. Sambell, and S. S. Zhong, "Polarization-agile antennas," *IEEE Antennas Propag. Mag.*, vol. 48, no. 3, pp. 28-37, Jun. 2006.

[15] R.A. Valenzuela, L. Ahumada, and R. Feick, "The effect of unbalanced branches on the performance of diversity receivers for urban fixed wireless links," *IEEE Trans. Wireless Commun.*, vol. 6, no. 9, pp. 3324-3332, Sept. 2007.

[16] J. Wu and S. A. Yang, "Dual polarization waves reuse scheme in cross polarization channel," in *Proc. IEEE GLOBECOM 1999*, vol. 5, pp. 2714-2718.

[17] V.I. Roman, "Frequency reuse and system deployment in local multipoint distribution service," *IEEE Pers. Commun.*, vol. 6, no. 6, pp. 20-27,Dec. 1999.

[18] D. Scherer, "Optimizing frequency re-use in point-to-multipoint deployments," in *Proc. IEEE RAWCON*, 10-13 Sep. 2000, pp. 83-86.

[19] K. Nishimori and K. Cho, "Evaluation of SDMA employing vertical pattern and polarization control in actual cellular environment measurement," in *Proc. IEEE VTC 2004*, 17-19 May 2003, pp. 244-248.

[20] K. E. Ntagkounakis, P. I. Dallas, and B. S. Sharif, "Joint channel & polarization assignment for capacity enhancement in non-line-of-sight fixed wireless networks," in *Proc. IEEE PIMRC 2004*, 5-8 Sept. 2004, vol. 4, pp.3049-3053.

[21] C. Degen and W. Keusgen, "Performance of polarisation multiplexing in mobile radio systems," *Elec. Lett.,* vol. 38, no. 25, pp. 1730-1732, 5 Dec. 2002.

[22] C. Oestges, V. Erceg and A. J. Paulraj, "Propagation modeling of MIMO multipolarized fixed wireless channels," *IEEE Trans. Veh. Technol.*, vol. 53, no. 3, pp. 644-654, May 2004.

[23] D. Yu, A. Burr, and G. White, "Performance of MIMO systems with combined polarization multiplexing and transmit diversity," *Proc. IEEE VTC 2005*, 30 May – 1 Jun. 2005, vol. 2, pp. 869-873.

[24] L. Jiang, L. Thiele, and V. Jungnickel, "On the modeling of polarized MIMO channel," in Proc. Europ. Wireless 2007, 1-4 Apr. 2007. [Online]. Available: http://www.ew2007.org/papers/1569014361.pdf.

[25] M. Coldrey, "Modeling and capacity of polarized MIMO channels," *Proc. IEEE VTC 2008 Spring*, 11-14 May 2008, pp. 440-444.

[26] D. J. Cichon, T. Kurner and W. Wiesbeck, "Polarimetric aspects in antenna related superposition of multipath signals," *Proc. ICAP 1993*, pp. 80-83, 30 Mar. – 2 Apr.1993.

[27] M. M. McKinnon, "Three-dimensional statistics of radio polarimetry," *Astrophys. J. Suppl.,* vol. 148, no. 2, pp. 519-526, Oct. 2003.

[28] K. N. Sivertsen, A. E.-L. Liou, D. G. Michelson, "Depolarization of propagating signals by narrowband Ricean fading channels," *Proc. IEEE VTC 2008*, 11-14 May 2008, pp. 1534-1538.

[29] L. J. Greenstein, D. G. Michelson, and V. Erceg, "Moment-method estimation of the Ricean K-factor," *IEEE Commun. Lett.*, vol. 3, no. 6, pp. 175-176, Jun. 1999.

[30] "Wave Polarization," in J. Kraus and K. Carver, *Electromagnetics,* New York: McGraw-Hill, 1973, Chap. 11.

[31] H. A. Mott, *Antennas for Radar and Communications: A Polarimetric Approach,* New York: Wiley, 1992.

[32] W. L. Stutzman, *Polarization in Electromagnetic Systems*, Boston: Artech House, 1993.

[33] H. Sampath, S. Talwar, J. Tellado, V. Erceg, and A. Paulraj, "A fourth-generation MIMO-OFDM broadband wireless system: design, performance, and field trial results," *IEEE Commun. Mag.*, vol.40, no.9, pp. 143-149, Sept. 2002.

[34] M. A. Stephens, "EDF statistics for goodness of fit and some comparisons," *J. Amer. Statistical Assoc.*, vol. 69, no. 2, pp. 730-737, Sep. 1974.

[35] R. Fisher, "Dispersion on a sphere," *Proc. Roy. Soc. London Ser. A*, vol. 217, no. 1130, pp. 295-303, May 1953.

[36] N. I. Fisher, T. Lewis, and B. J. J. Embleton, *Statistical Analysis of Spherical Data.* Cambridge: Cambridge Univ. Press, 1987.

[37] K. V. Mardia and P. E. Jupp, *Directional Statistics*, New York: Wiley, 2000.

[38] P. L. McFadden, "The best estimate of Fisher's precision parameter κ," *Geophys. J. R. Astr. Soc.*, vol. 60, pp. 397-407, 1980.

[39] D. J. Best and N. I. Fisher, "The bias of the maximum likelihood estimators of the von Mises-Fisher concentration parameters," *Commun. Statist.*, vol. B10, pp. 493-502, 1981.

[40] S. R. Hanna and J. C. Chang, "Representativeness of wind measurements on a mesoscale grid with station separations of 312 m to 10 km," *Boundary-Layer Meteorol.,* vol. 60, pp. 309-324, 1992.

[41] G. Ulrich, "Computer generation of distributions on the m-sphere," *Appl. Statist.*, vol. 33, no. 2, pp. 158-163. 1984.

[42] A. T. A. Wood, "Simulation of the von Mises Fisher distribution," *Commun. Statist. - Simula.,* vol. 23, no. 1, pp. 157-164, 1994.

[43] N. I. Fisher, T. Lewis, M. E. Willcox, "Tests of discordancy for samples from Fisher's distribution on the sphere," *Appl. Statist.*, vol. 30, no. 3, pp. 230-237. 1981.

7 Conclusions and Recommendations

7.1 Conclusions

Growing use of point-to-multipoint fixed wireless networks to support network access and system automation in suburban macrocell environments has prompted regulators to re-allocate various bands between 200 MHz and 2 GHz to such applications [1]-[5]. Links in such networks are usually obstructed by buildings and foliage and are classified as non-line-of-sight. Although it is well-known that such links are susceptible to fading caused by windblown trees and foliage, most past efforts to characterize fading on such links have focused on frequency bands at 1.9 GHz and above [6]-[10]. In this work, we have shown how signal fading in the 220, 850 and 1900 MHz bands vary with both distance and time-averaged wind speed in a representative macrocell environment. Based upon time-series of received signal strength collected in a typical macrocell environment with moderate foliage at locations between 1 and 4 km from a transmitting site located 80 m above ground level, we show that fading on such links is relatively severe at 1.9 GHz but decreases rapidly as the carrier frequency decreases. We have expressed our results in the form of a first-order simulation model.

To date, however, there have been relatively few efforts to characterize the rate of fading on fixed wireless channels in any band [11]-[13]. Therefore, on the first pass, we observed temporal fading on 1.9 GHz fixed wireless channels during short-term measurements at 107 different locations in a suburban macrocell environment characterized by flat terrain and heavy foliage in order to determine how the rate of fading varies with average wind speed and distance. For each location, we estimated the Ricean K-factor using a moment-based estimator and the equivalent Doppler frequency (which is related to the maximum Doppler frequency by a factor that depends upon the shape of the Doppler spectrum) by fitting the measured level crossing rate (LCR) and average fade duration (AFD) distributions to expressions normally justified for mobile wireless links using a method recently proposed by Feick, Valenzuela and Ahumada (2007). As has been observed at other sites, the Ricean K-factor decreased with both average wind speed and distance. However, we found that the equivalent Doppler frequency was effectively uncorrelated with wind speed and noticeably increased with distance. Similar measurements at other sites will be required to determine the extent to which these trends are affected by foliage density and tower height. With preliminary results observed at 1.9 GHz, we moved one step further by transmitting CW signals in the 220, 850 and 1900 MHz bands from a transmitting site located 80 m above ground level in a typical macrocell environment with moderate foliage, and collecting time-series of received signal strength at distances between 1 and 4 km from the site. We then reduced the data to show how the depth and rate of signal fading vary with frequency band, distance and time-averaged wind speed in such an environment. Our most significant finding is that the rate of signal fading is very similar in all three bands. In particular, it is not proportional to carrier frequency, as a simplistic model involving moving scatterers might suggest. These results will provide useful guidance to those who seek to develop detailed physical models of fade dynamics in suburban macrocell environments.

In addition to the studies of depth and rate of fading as described above, polarization diversity on narrowband fixed wireless links has traditionally been characterized in terms of the fading statistics and the cross-correlation between the Rician distributed signals on each branch, e.g., [6]. A complementary approach, which provides additional physical insight and which is independent of the polarization states of the diversity receiving antennas, is to characterize the manner in which the polarization states observed at the receiver disperse across the Poincaré sphere. In the last part of our work, we show by simulation that when the fading signals observed on orthogonally polarized diversity branches follow Ricean statistics, the distribution of polarization states on the Poincaré sphere is well-approximated by a Fisher distribution. Further, we show that the Fisher concentration parameter is: (1) completely determined by the corresponding Ricean K-factors and the cross-correlation coefficient between the diversity branches, both of which can be estimated from simple measurements of received power vs. time, and (2) a good indicator of the level of cross-polar discrimination (XPD) on the channel. The insights gained are potentially useful to those engaged in the development and validation of schemes that use either polarization re-use or polarized MIMO [14], [15]. To verify our simulation results and to further characterize the polarization states, a measurement campaign has been conducted. Based upon 1.9 GHz uplink diversity measurements collected at 95 different locations in a typical suburban macrocell environment, we show that: (1) the means of the polarization state distributions (or the mean polarization states) observed over all locations tend to follow a Fisher or spherical normal distribution with concentration parameter κ_m about the polarization state of the transmitter, (2) the polarization state distributions observed at each location tends to follow a Fisher distribution with concentration parameter κ about the mean polarization state at that location, (3) the Fisher concentration parameter κ is closely correlated with channel parameters such as the Ricean K-factor and cross-polar discrimination (XPD) and (4) κ is negatively correlated with the average speed of the wind blowing through foliage along the path. We have proposed a method for simulating polarization state dispersion that will be useful to those tasked with the simulation and test of polarization diversity and adaptive antennas and/or the design and evaluation of polarization re-use and polarized MIMO schemes.

7.2 Recommendations for Future Work

The results presented in this work are specific to geographical conditions of the specific sites, distance, density of vegetation, relative transmitting and receiving antenna heights, and meteorological statistics experienced during the measurement period, i.e., averaged wind speed. Although the work presented here represents an important first step, development of models applicable to a broad range of environments will require additional measurement data: (1) from other sites, (2) from transmitters at different heights and (3) at additional frequencies within the range of interest.

References

[1] W. Webb, "Broadband fixed wireless access as a key component of the future integrated communications environment," *IEEE Commun. Mag.*, vol. 39, no. 9, pp. 115-121, Sep. 2001.

[2] K. Lu, Y. Qian and H-H Chen, "Wireless broadband access: WIMAX and beyond," *IEEE Commun. Mag.*, vol. 45, no. 5, pp. 124-130, May 2007.

[3] S. S. Venkata, A. Pahwa, R. E. Brown, and R. D. Christie, "What future distribution engineers need to learn," *IEEE Trans. Power Syst.*, vol.19, no.1, pp. 17-23, Feb. 2004.

[4] G. Simard and D. Chartrand, "Hydro-Quebec's Economic and Technical Approach to Justify its Distribution Automation Program," in *Proc. IEEE PES'07,* pp. 1-5, 24-28 Jun. 2007.

[5] S. Jim, W. Carr, and S. E. Collier, "Real time distribution analysis for electric utilities," in *Proc. IEEE REPC'08,* pp. B5-B5-8, 27-29 Apr. 2008.

[6] D. G. Michelson, V. Erceg, and L. J. Greenstein, "Modeling diversity reception over narrowband fixed wireless channels," in *Proc. IEEE MTT-TWA'99*, pp. 95-100, 21-24 Feb. 1999.

[7] S. Perras and L. Bouchard, "Fading characteristics of RF signals due to foliage in frequency bands from 2 to 60 GHz," in *Proc. WPMC'02*, 27-30 Oct. 2002, pp. 267-271.

[8] M. J. Gans, N. Amitay, Y. S. Yeh, T. C. Damen, R. A. Valenzuela, C. Cheon and J. Lee, "Propagation measurements for fixed wireless loops (FWL) in a suburban region with foliage and terrain blockages," *IEEE Trans. Wireless Commun.*, vol. 1, no. 2, pp. 302-310, Apr. 2002.

[9] E. R. Pelet, J. E. Salt, and G. Wells, "Effect of wind on foliage obstructed line-of-sight channel at 2.5 GHz," *IEEE Trans. Broadcasting*, vol. 50, no. 3, pp. 224-232, 2004.

[10] D. Crosby, V. S. Abhayawardhana, I. J. Wassell, M. G. Brown, and M. P. Sellars, "Time variability of the foliated fixed wireless access channel at 3.5 GHz," in *Proc. IEEE VTC 2005 Spring*, 25-28 Sep. 2005, pp. 106-110.

[11] R. Feick, R. A. Valenzuela, and L. Ahumada, "Experiment results on the level crossing rate and average fade duration for urban fixed wireless channels," *IEEE Trans. Communic.*, vol. 9, no. 1, pp. 175-179, Jan 2007.

[12] S. Thoen, L. V. D. Perre, and M. Engels, "Modeling the channel time-variance for fixed wireless communications," *IEEE Communic. Lett.*, vol. 6, no. 8, pp. 331-333, Aug. 2002.

[13] A. Domazetovic, L. J. Greenstein, N. B. Mandayam, and I. Seskar, "Estimating the Doppler spectrum of a short-ranged fixed wireless channel," *IEEE Communic. Lett.*, vol. 7, no. 5, pp. 227-229, May 2003.

[14] V. R. Anreddy and M. A. Ingram, "Capacity of measured Ricean and Rayleigh indoor MIMO channels at 2.4 GHz with polarization and spatial diversity," *IEEE Proc. IEEE WCNC*, pp. 946–951, April 3-6 2006.

[15] H. Bolcskei, R.U. Nabar, V. Erceg, D. Gesbert and A.J. Paulraj, "Performance of spatial multiplexing in the presence of polarization diversity," *Proc. IEEE ICASSP*, pp. 2437–2440, May 7-11 2001.